Broadband IR Stokes polarimetry for the electro-optic characterization of cadmium zinc telluride

by

William FitzGerald
B.Sc., University of Victoria, 2013

A Dissertation Submitted in Partial Fulfillment of the Requirements for the Degree of

DOCTOR OF PHILOSOPHY

in the Department of Chemistry

Broadband IR Stokes polarimetry for the electro-optic characterization of cadium zinc telluride

by

William FitzGerald
B.Sc., University of Victoria, 2017

Supervisory committee

Dr. Dennis K. Hore, Supervisor
(Department of Chemistry)

Dr. Alexander Brolo, Departmental Member
(Department of Chemistry)

Dr. David Harrington, Departmental Member
(Department of Chemistry)

Dr. Christopher Bose, Outside Member
(Department of Mathematics and Statistics)

ABSTRACT

The infrared portion of the electro-magnetic spectrum is a challenging region in which to perform optical techniques, limited by both device efficiency and availability. In this dissertation, a new optical technique is introduced to facilitate polarization state measurement across the mid-IR. In addition, cadmium zinc telluride (CZT) is investigated as a potential new material suitable for electro-optic devices which function in the mid-IR, while also being characterized by other optical analysis methods.

Thin film interference is discussed as it relates to optical techniques and electronic devices. A Stokes polarimeter is used to study the oxide development on the surface of CZT electronic devices, and the effect of natural thin films on substrates used in optical techniques is discussed. In particular, the impact of thin film interference on sum-frequency generation spectroscopy measurements of methyl group orientation are assessed.

An FTIR source operated in step-scan mode is used to create a broadband, IR Stokes polarimeter which measures the polarization state of light from 2.5-11 μm simultaneously. Its design, involving two photo-elastic modulators and an analyzer, and theory are described in detail. This instrument is demonstrated by measuring linearly polarized light, and is applied to the measurement of the refractive index dispersion of quartz from 2.5-4 μm, which goes beyond the limits of literature values.

Electro-optic crystals of CZT with electrodes of gold and indium are characterized at each wavelength in the mid-IR in terms of their electro-optic effects and apparent depolarization using the Stokes polarimeter. The material displays high-resistivity, allowing it to be operated with up to 5 kV applied DC voltage. The linear electro-optic effect is observed, but overall properties of the samples are found to be heavily dependent on the choice of metal for the electrodes. With a high-work function electrode material in gold, a large depletion region is created when high voltage is applied, which leads to a gradient in electric field throughout the material. This causes a beam of light transmitted

through it to experience a distribution of electro-optic behaviours, which leads to overall depolarization of the light. Indium's work function is lower than gold's, and is closer to that of CZT. With indium electrodes, the electric field is found to be more consistent, and behaviour is much closer to ideal.

The electro-optic effect of CZT is also characterized with AC applied voltage in order to assess its suitability to AC applied voltage applications. The power supply used for this was limited to 60 Hz, which precludes a complete characterization in this regard, but unexpected behaviour was seen. A methodology utilizing an oscilloscope and FTIR was developed in order to more completely understand the material response, and divergent behaviour with positive and negative voltage was found.

Contents

Supervisory Committee ii

Abstract iii

Table of contents **v**

List of tables **viii**

List of figures **ix**

Acknowledgements **xvii**

1 Introduction **1**

1.1 Motivation 1

1.2 Stokes vector description of light polarization 2

1.3 Mueller matrix description of optical behaviour of a material 3

1.4 Polarizers, birefringence and dichroism 5

1.5 Polarimeters and ellipsometers in the infrared 7

1.6 Variable retarders in the mid-infrared region 9

1.7 Theory and origin of the linear electro-optic effect 10

1.8 Cadmium zinc telluride 12

1.9 Scope of dissertation 14

2 Polarimetry studies on thin film interfaces **15**

2.1 Multiple-beam interference in thin films 15

2.2 Characterization of CZT oxide thickness 17
2.2.1 Introduction 17
2.2.2 Theory 18
2.2.3 Experiment and Results 22
2.3 Multiple-beam interference effects on methyl group tilt-angle determination via SFG 22
2.3.1 Background Theory 24
2.3.2 Consequences for orientation determination 26
2.3.3 Interpretation of spectral phase 30
2.3.4 Considerations for data collection 31
2.4 Conclusions 34

3 Design and Calibration of a Broadband IR Stokes Polarimeter 35

3.1 Instrument design and theory 35
3.1.1 Definitions and Approach 35
3.1.2 Fourier Analysis 38
3.1.3 Expressing I_{dc} 40
3.1.4 Expressing I_{ω_1} 43
3.1.5 Expressing $I_{2\omega_1}$ 48
3.1.6 Expressing $I_{2\omega_2}$ 51
3.1.7 F coefficient variables 55
3.1.8 Isolating the Stokes elements 56
3.2 Interpretation of data and results 61
3.3 Conclusion 66

4 Electro-optic characterization of CZT with DC applied voltage 67

4.1 Introduction 67
4.2 Experimental 68

4.2.1 Cadmium zinc telluride EO crystals 68
4.2.2 Enclosure for high voltage application 68
4.2.3 Broadband mid-infared Stokes polarimetry 69
4.2.4 Polarized IR transmittance measurements 71
4.2.5 Leakage current measurements 72
4.3 Results 73
4.3.1 Electro-optic characterization 73
4.3.2 Depolarization 75
4.4 Modeling 83
4.5 Discussion 88
4.6 Summary 91

5 Electro-optic characterization of CZT with AC applied voltage 92
5.1 Introduction 92
5.2 Experimental 93
5.3 Results 98
5.4 Discussion 101
5.5 Conclusion 104

6 Summary and Conclusions 105
6.1 Summary of research 105
6.2 Recommendations for further work 106

A Further details of derivation of Stokes vector expressions 108

References 120

List of Tables

1.1 Lookup table for the index I that represents the pair of indices (i, j) 12

2.1 Values of refractive indices corresponding to $\lambda_{\mathrm{SFG}} = 461$ nm, $\lambda_{\mathrm{vis}} = 532$ nm, $\lambda_{\mathrm{IR}} = 3.47$ μm. 26

List of Figures

1.1 The Poincaré sphere visualization of the Stokes vector convention for description of the polarization state of light. A few special cases are highlighted. All linear states occupy the equator, and the circular states occupy the top and bottom 'poles' of the sphere. A path from the equator to either pole along one longitudinal line sees a linear state at a given azimuth become an ellipse with the same azimuth, which becomes wider until it becomes a perfect circule. 4

1.2 Crystal structure of a zinc blende compound such as CZT. In CdTe, ZnSe and other such compounds with two components, one element will be (a) and the other (b) in the figure. CZT is an alloy of CdTe and ZnTe, and in its crystal structure, Te will occupy (a) sites, while the (b) sites are split between Cd and Te in some specified proportion. 14

2.1 Multiple-beam interference arising from reflection off of a surface with a non-opaque thin film. Here, a yellow layer on top is the target of optical analysis, but the reflected beam is a summation of beams with different paths. 16

2.2 The instrumental scheme used for oxide thickness measurement via ellipsometry. The 633 nm laser source is directed through a series of polarization state generation optics. A linear polarizer and quarter-wave plate are used initially to create circularly polarized light, which ensures that any linear state will have equal intensity. The light is then polarized before reflecting off of the sample. The reflected light is directed into the Stokes polarimeter. 18

2.3 Polarimetry measurement of the thickness of the oxide layer on CZT. For a series of thicknesses from 2 nm to 12 nm, in steps of 2 nm, the variation in the Stokes vectors resulting from reflection at different incident angles are shown. The s_0 curve, representing total intensity, in the upper left panel increases with increasing incident angle, so the data is normalized to this to better appreciate the shape of the Stokes elements themselves. 23

2.4 A substrate–film–adsorbate system where the SFG signal originates only from the molecules adsorbed to the film. 24

2.5 (a) Effect of multiple beam interference on methyl group tilt angle determination, for molecules adsorbed at the air–polystyrene thin film interface, on a silica substrate. For a given sps/ssp SFG intensity ratio, the fine dashed curve is used to determine the molecular tilt angle in the case of a 50 nm film, and the wide dashed curve in the case of 500 nm. If multiple beam interference were ignored, the tilt angle would be determined from the solid curve. These errors in tilt angle are summarized in (b) for a silica substrate and (c) for a silicon substrate. Colours indicate the difference between the actual methyl tilt angle, and what would be determined without considering multiple beam interference. 28

2.6 Phase of the LLL prefactor that determines the phase of $\chi^{(2)}_{\text{eff}}$ as a function of the polystyrene thickness. Results for the silica substrate are shown in blue; those for silicon in red. The horizontal dashed line indicates the zero-phase result for the air–polystyrene system. 31

2.7 (a) Determination of optimal visible and infrared beam angles for ssp polarization at the air–polystyrene interface. The same calculation, but including multiple beam interference for the air–polystyrene–substrate system with (b) 50 nm polymer on silica, (c) 500 nm polymer on silica, (d) 50 nm polymer on silicon, (d) 500 nm polymer on silicon. (f) The optimum visible and IR angles as a function of film thickness; (g) the fraction of the maximum SFG intensity that would be measured if the beam angles were maintained at those optimum for the air–polystyrene surface. For sps beam polarizations, we plot (h) the optimal angles and (i) the fraction of the maximum achievable intensity corresponding to those angles. 32

3.1 Stokes polarimeter based on two photoelastic modulators, indicating the polarizers ($\mathbf{P}$, or $\mathbf{A}$ in the case of the analyzer), sample position ($\mathbf{S}$), single-element integrating detector ($\mathbf{D}$). The first modulator is denoted $\mathbf{R}_a$ and the second one is $\mathbf{R}_b$. Optics are drawn in black, the beam path is shown in red, and electronics are shown in green. 36

3.2 (a) Double-sided interferograms for 60° linearly polarized light collected in the step-scan mode of the FTIR, illustrating the DC (black), I_{2b} (red), I_{2a} (blue), and I_{1a} (green) components as demodulated by the lock-in amplifiers. (b) Fourier-transformed signals from 3–11 μm, with I_{2b}/I_{DC} in red, I_{2a}/I_{DC} in blue and I_{1a}/I_{DC} in green. Points are experimental data; lines are model obtained using Eqs. 3.36. (c) Resulting Stokes vector elements after processing the data using Eqs. 3.51 with s_1/s_0 in red, s_2/s_0 in blue, s_3/s_0 in green, and the degree of polarization in black. (d) Interferograms collected when a quartz waveplate is in the beam path, with corresponding (e) Fourier-transformed signals and (f) Stokes vectors in the 2.5–3 μm region, (g,h) 3–4 μm region. The solid lines in (e,f) are calculated based on literature dispersion data for quartz up to 3 μm. The lines in (g,h) are using dispersion data obtained in this experiment; further details of this determination appear in Fig. 3.3. 63

3.3 (a) Birefringence dispersion as determined from (b) the sample's retardation and thickness, ultimately from (c) the measured Stokes vectors. Experimental data indicated by points. The black line in (a) is a fit to a third-degree dispersion model, given in Eq. 3.53 with $a = 7.624 \times 10^{-5}$, $b = -9.626 \times 10^{-4}$, $c = 4.112 \times 10^{-3}$, and $d = 3.591 \times 10^{-3}$. The corresponding literature model is indicated by the dashed red line up to 3 μm. The inset to (b) shows a zoom-in of the difference between our fit data and the literature-predicted retardation. The model Stokes vectors, indicated by lines in (c) are calculated from a fit to the dispersion data over the entire 2.5–4 μm region. 65

4.1 Crystal axes and orientation of CZT samples used. Light propagates along the $[110]$ axis and experiences birefringence when voltage is applied on the $[\bar{1}10]$ axis across electrodes on opposite faces. 69

4.2 At the top, 3-D renderings of the specially-designed enclosure used to house the CZT sample. This allowed the crystal (device under testing, or DUT in the diagram) to be securely held without added pressure, which could change the characteristics of the material. On the bottom, the circuit diagram for applying high voltage and measuring leakage current. 70

4.3 The leakage current of the gold- and indium-electrode CZT samples as increasing DC voltage is applied. 74

4.4 The normalized Stokes vectors resulting from a linear polarizer with 0° linearly polarized light incident on a CZT sample with the optical axis oriented at 45°, measured at each wavelength across the instrument range, with voltage applied to the crystal ranging from 0 to 5 kV. s_1, s_2 and s_3 are shown divided by s_0, and these values are used to calculate the degree of polarization via DOP = $\sqrt{s_1^2 + s_2^2 + s_3^2}$. 76

4.5 The electro-optic effect of CZT displayed in two ways. In the upper panel, the retardation with respect to wavelength is plotted for a few selected wavelengths. This corresponds to vertical slices of the lower panel, which shows the retardation at all of the wavelengths and all of the voltages together. The black traces on the lower panel show the voltages required for quarter- (lower) and half-wave (upper) retardation at each wavelength across the instrument range. 77

4.6 For both CZT samples, the transmission spectrum of light through a crossed- and parallel-polarizer system, at a range of applied voltages (0 kV in red progressing to 5 kV in violet) is shown in the top and bottom panel, respectively, normalized to the spectrum through parallel polarizers with no applied voltage to the crystal. The CZT optical axis is at 45° relative to the front polarizer. The deviation of the maxima and minima from 1 and 0 can be attributed to depolarization of the incident light as it passes through the CZT sample. 78

4.7 Transmittance of light through the crystal in a 45-45-135 configuration. Depolarization here would result in a proportional increase in transmitted intensity, but a negligible amount is seen as the voltage is ramped up to 5 kV. 80

4.8 The raw transmittance of light through the crystal as a function of voltage (0 kV in red progressing to 5 kV in violet) for two incident polarization states. With incident light oriented parallel to the electro-optic optical axis, we see a small decrease in transmission which coincides with the drop in degree of polarization. However, this is not seen in the case of incident light oriented 45° off the optical axis, which is the application configuration. Overall, there seems to be very little light intensity lost to scattering, if any. Wavelengths to focus on in the bottom two panels were selected so as to avoid the CO_2 and water absorptions, which cause erratic data as the conditions vary within the experimental setup. 81

4.9 At five different voltages, the transmittance spectrum of the crossed-polarizer system is measured at three different locations in the crystal cross-section. The retardation increases from the bottom to the top of the crystal. . 82

4.10 The electric field of each crystal imaged at 1 kV applied voltage. This is achieved in a qualitative sense in a 4 mm x 4 mm array, with bias applied in each direction on the top and bottom, respectively. The electric field is taken as the amount of light transmitted through a 0-45-90 configuration, normalized to the amount of light obtained through a 0-45-0 configuration at 0 applied voltage. Areas where no light reached the detector in the latter configuration are blacked out. 84

4.11 A depolarization model is shown for a crystal with 5 kV applied DC voltage, where depolarization results from a distribution of different retardations throughout the sample. The top panel shows the distribution of retardations being considered for the cross-section of the beam. The middle panel shows the model for the transmission in the 0-45-90 configuration given this distribution compared to the experimental data. The bottom panel shows the model (lines) for the resulting Stokes vector from a 0-45 configuration compared to the experimental data (points). 87

4.12 The mean electro-optic coefficient and the width of the distribution which best fit both crossed-polarizer and Stokes polarimeter data are shown for each crystal. 88

5.1 Schematic of the instrumentation for measuring the amplitude of the CZT sample's retardation, and its static retardation. Incident is chopped and polarized at 0°, and after encountering the sample with optical axis at 45°, passes through another polarizer at 0°. The signal at the detector is passed to three lock-in amplifiers, which demodulate the signal at three frequencies of interest, which correspond to the material properties. 94

5.2 The oscilloscope trace of the reference voltage from the AC power supply. Deviation from ideal sinusoidal shape can clearly be seen. 95

5.3 Conventional calibration of a 37 kHz photo-elastic modulator using a scheme involving a polarizer and analyzer at 0° on either side of the PEM with its optical axis at 45°, at two different driving voltages. The second-harmonic and fundamental frequency components of the intensity can be fit to a model in order to determine the amplitude of the PEM's retardation as well as its static retardation. The legend refers to the driving voltage setting, where the PEM is set to 2.1 rad or 3.1 rad retardation amplitude at 3000 cm^{-1}. The exact voltage supplied to the PEM is unknown. 96

5.4 Schematic of the instrumentation used to precisely visualize the shape of the waveform at the detector. The optical path is the same as in Fig. 5.1, but with no chopper, and no lock-in amplifiers. The signal is passed to an oscilloscope, which is triggered by the reference voltage from the AC high-voltage power supply. 97

5.5 Attempts to fit the normalized second-harmonic and fundamental frequency component intensity spectra with an amplitude and static retardation are insufficient at a variety of voltages. 99

5.6 Oscillocope visualization of the response of the optical properties of a ZnSe PEM (left column) and a CZT electro-optic crystal (right column) to applied AC voltage. Raw data is shown in the top row, and is Fourier transformed along the FTIR-step axis to produce the middle row. The data slice at 2763 cm^{-1}, (bottom row, orange) is consistent with a model (blue) in either case, though the method of developing the model is more complicated for CZT. 102

ACKNOWLEDGEMENTS

I would like to thank:

Dennis Hore, for advice and mentorship, and extreme generosity with your time.

My wife, Olyvia, for making sure the day-to-day frustrations of research stayed behind when I went home.

My parents, Robin and Zinda, and my brothers, Graham and Nicholas, for motivating me to get to this point.

Sandra Roy, Paul Covert, Tasha Jarisz and Wei-Chen Yang, for insightful discussions and great times in the lab.

David Giles and Saeid Taherion, for introducing me to CZT and for all the help along the way.

Andrew McDonald, for always being willing to help.

NSERC and UVic, for generous funding to allow me to carry out this research.

Chapter 1

Introduction

1.1 Motivation

The mid-infrared region is a difficult region to operate in for optical techniques. Sources of mid-infrared radiation generally provide quite weak emission spectra compared to sources in other regions, while optical components suitable to the region are sparse and detectors have low sensitivity. Despite the challenge, there is also significant motivation for capabilities being expanded in this region. The infrared region corresponds to vibrational energy level transitions in molecules, which makes optical techniques in the infrared especially useful for identification and for probing molecular structure and orientation [1]. As such, new instrumental techniques for the mid-IR, and new optical devices are of interest to the field.

Cadmium zinc telluride (CZT) holds promise as a new optical device material which can function across the mid-infrared region by way of the linear electro-optic effect, otherwise known as the Pockels effect. This property allows the manipulation of the polarization state of light by way of an applied voltage. CZT, a zinc-doped relative of CdTe, was first studied for nuclear detector applications in the 1960s [2]. Despite having ideal qualities for detectors of gamma and X-ray radiation, including high resistivity and the ability to function at room temperature, the major obstacle preventing these materials from becoming wide-spread is the difficulty to produce high-quality crystals [3]. CZT has a zinc-blende structure, which by necessity leads to the Pockels effect, allowing it to be used

to modulate the polarization state of light. To this point, CZT's electro-optic properties have not been documented across the mid-IR. As a material with very high transmission in the infrared region, characterizing its properties in this wavelength range opens up the possibility of adding another useful material for optical devices in the infrared.

The Pockels effect involves applying voltage to a material and causing it thereby to alter the polarization state of light [4]. The amount by which it changes the polarization state depends on the voltage in a linear manner. In order to study the electro-optic properties of the material, it is necessary to use instrumentation to monitor the polarization state of light. We wish to do this across the mid-IR region, where such instrumentation is sparse. We have designed a new type of polarimeter for measuring the polarization state of light across all wavelengths in the mid-IR simultaneously, using a broadband source from an FTIR.

In this dissertation, I first discuss the use of optical techniques with regards to thin films on surfaces. I introduce the broadband mid-IR Stokes polarimeter, and from there discuss the characterization of light polarization phenomena in materials, including investigation of the electro-optic properties of CZT using this and other techniques.

1.2 Stokes vector description of light polarization

The polarization state of light may be completely described by the four-element Stokes vector $\mathbf{s}$ [5–7]. In this description s_0 represents the total intensity, s_1 the difference in intensities between components polarized horizontally and vertically, s_2 the difference between the orthogonal $\pm 45^\circ$ states, and s_3 the difference between right- (RCP) and left-handed circular (LCP) components.

$$\mathbf{s} = \begin{bmatrix} s_0 \\ s_1 \\ s_2 \\ s_3 \end{bmatrix} = \begin{bmatrix} I_{\text{total}} \\ I_0 - I_{90} \\ I_{45} - I_{-45} \\ I_{\text{RCP}} - I_{\text{LCP}} \end{bmatrix} = \begin{bmatrix} E_x E_x^* + E_y E_y^* \\ E_x E_x^* - E_y E_y^* \\ E_x E_y^* + E_y E_x^* \\ i(E_x E_y^* - E_y E_x^*) \end{bmatrix}. \tag{1.1}$$

Elements of the Stokes vector are related by

$$s_0^2 \leq s_1^2 + s_2^2 + s_3^2 \tag{1.2}$$

where the equality holds in the case of perfectly polarized light (no depolarization of the source). It is also convenient to define the degree of polarization, DOP, from the Stokes vector elements normalized to s_0

$$\mathrm{DOP} = \sqrt{\left(\frac{s_1}{s_0}\right)^2 + \left(\frac{s_2}{s_0}\right)^2 + \left(\frac{s_3}{s_0}\right)^2} \leq 1 \tag{1.3}$$

with fully polarized light having a DOP of unity. Eq. 1.1 also illustrates that the Stokes vector is readily constructed from the x- and y-polarized components of the complex field, where $i = \sqrt{-1}$ and the asterisk denotes complex conjugation. This definition is useful as it readily enables modeling of the optical response and optical properties of materials for comparison with experimental polarization data. If each of the four elements of $\mathbf{s}$ is measured independently, it is possible to describe the azimuth, ellipticity, and handedness of the polarization ellipse, in addition to the fraction of the light that is depolarized.

A visualization which is useful when considering Stokes vectors is the Poincaré sphere, shown in Fig. 1.1. In this visualization, the axes of 3-dimensional space are the three latter Stokes elements normalized by $\mathbf{s_0}$. In this representation, any point on the surface of the sphere represents a particular polarization state of completely polarized light. The origin represents completely unpolarized light, and any point within the sphere is partially polarized. The radius of the sphere is 1, owing to Eq. 1.2.

1.3 Mueller matrix description of optical behaviour of a material

In order for the Stokes vector of light to change, it must encounter some environment which in some way manipulates the polarization state of light. Any such material, interface or other such environment can be described mathematically, in the Stokes formalism, by a Mueller matrix. There are Mueller matrices for polarizing unpolarized light, or for changing the polarization state of polarized light to something else. Unlike the Stokes vector, it is harder to ascribe certain characteristics to each element of the Mueller matrix.

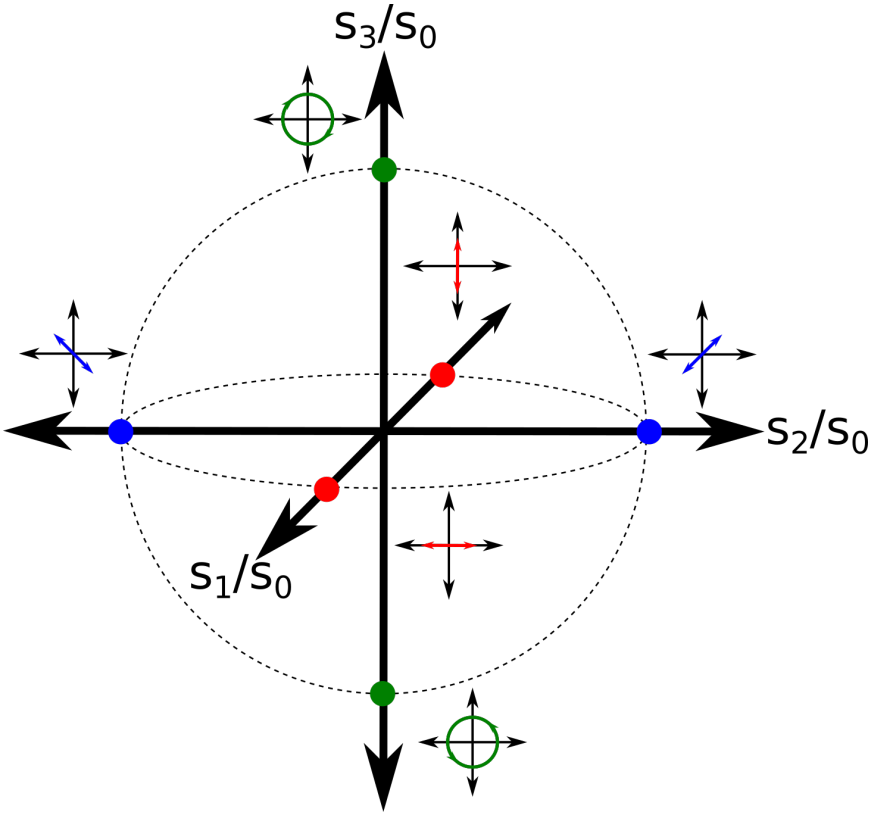

Figure 1.1: The Poincaré sphere visualization of the Stokes vector convention for description of the polarization state of light. A few special cases are highlighted. All linear states occupy the equator, and the circular states occupy the top and bottom 'poles' of the sphere. A path from the equator to either pole along one longitudinal line sees a linear state at a given azimuth become an ellipse with the same azimuth, which becomes wider until it becomes a perfect circule.

However, it is made such that for light with polarization state $\mathbf{s}$ encountering a material with Mueller matrix M, the resultant polarization state of the light, $\mathbf{s}'$ can be described simply by multiplying the matrix by the Stokes vector.

$$\mathbf{s}' = M \cdot \mathbf{s} \tag{1.4}$$

As this is matrix multiplication, it is not commutative. When multiple polarization state-manipulating components are encountered in a beam's path, the Mueller matrices for these components are multiplied on the left, in order of occurrence.

$$\mathbf{s}' = M_3 \cdot M_2 \cdot M_1 \cdot \mathbf{s} \tag{1.5}$$

There are known Mueller matrices for specific types of optical elements, and in the case of optics which contain optical axes, such as polarizers and retarders, the axis is considered by default to be horizontal. When the optical axis is rotated to a different angle, the Mueller matrix can be transformed to the corrected version by $M(\theta) = R(-\theta) \cdot M \cdot R(\theta)$, where R is the rotation matrix.

$$R(\theta) = \begin{bmatrix} 1 & 0 & 0 & 0 \\ 0 & \cos\theta & \sin\theta & 0 \\ 0 & -\sin\theta & \cos\theta & 0 \\ 0 & 0 & 0 & 1 \end{bmatrix} \tag{1.6}$$

1.4 Polarizers, birefringence and dichroism

In terms of instrumental design, the most common optical effects utilized are those of polarizers and birefringent materials. In a polarizer, only components of light polarized in a certain way are transmitted, with all other light being reflected. The transmitted polarization state can be linear or circular, but linear polarizers are much more common. The Mueller matrix for a linear polarizer with a horizontal azimuth is

$$P = \begin{bmatrix} 0.5 & 0.5 & 0 & 0 \\ 0.5 & 0.5 & 0 & 0 \\ 0 & 0 & 0 & 0 \\ 0 & 0 & 0 & 0 \end{bmatrix} \tag{1.7}$$

Linear polarizers exist for every wavelength region. In order to span the entire mid-infrared range, a wire-grid polarizer is really the only option for linear polarization. In this optic, very fine wires are holographically deposited on the surface of a substrate parallel to one another. When the light encounters the wires, any component of the light polarization parallel to the wires causes electrons to oscillate along the wires, which creates a back-reflected beam. The only light that can pass through is the component perpendicular to the wires, as very little oscillation of the electrons can occur on that axis. Due to the difficulty of preparing an optic of this type, they tend to be very expensive optical components.

Birefringence is another important material property that can be useful for instrument design. Unlike polarizing optics, birefringence can't create polarized light from unpolar-

ized light, nor does it remove any intensity from a light source in and of itself. Birefringence delays one polarized component of light with respect to the orthogonal component due to these components encountering different refractive indices within the material, and thus changes the polarization state. These components can be linear, or circular components of light, which then travel through the material at different speeds.

Both linear and circular birefringence are phenomena that can make a material useful for optical instrumentation, or can be targetted for analysis in order to characterize a material. Commonly, instruments make use of quarter-wave plates, which is a linearly birefringent optic which retards one linear component by one quarter wave with respect to another. Most often, they are tuned to a specific wavelength, and the phase delay is induced by natural birefringence of the material used for the optic. Typically, the thickness of a birefringent material required in order to induce a quarter-wave retardation is very small, and so multi-order wave plates are more common, in which the retardation is several periods plus a quarter-wave. This means that the retardation is very sensitive to a change in the wavelength of the light, and the optic is very specifically used for one wavelength. However, zero-order retarders exist, where a precise thickness of birefringent material is supported by a substrate, and achromatic designs for retarders exist using total internal reflection or other non-birefringence phenomena.

The Mueller matrix for a linear retarder with phase retardation of ϕ, and the optical axis (for a linearly birefringent material, the axis at which light travels fastest) horizontal, can be described by its Mueller matrix, L.

$$L = \begin{bmatrix} 1 & 0 & 0 & 0 \\ 0 & 1 & 0 & 0 \\ 0 & 0 & \cos\phi & \sin\phi \\ 0 & 0 & -\sin\phi & \cos\phi \end{bmatrix} \tag{1.8}$$

Using a linear polarizer and a quarter-wave plate in succession, any polarization state on the Poincare sphere can be created. For materials analysis, often a polarization state is prepared prior to incidence on the sample, and thus these two optics are very useful in such schemes.

In terms of materials themselves, some have natural birefringence, and in others it can be created through mechanical strain or other phenomena such as electro-optic effects. Chiral compounds naturally possess circular birefringence, which is what rotates light depending on the amount of the chiral material the light encounters.

Other optical properties of materials which are interesting to study are linear and circular dichroism. Where birefringence is the property of two different refractive indices within a material, dichroism is the property of two different extinction coefficients. This leads to one polarized component of light being absorbed more than the orthogonal component, which both attentuates the light and alters its polarization state.

1.5 Polarimeters and ellipsometers in the infrared

Measurement of the polarization state of light is an important aspect of experimental and modeling efforts in physics and astronomy [8, 9], chemistry [10, 11], and materials science [12, 13]. Preparing light in a specific polarization state, and then monitoring how the polarization has been altered after being transmitted through or reflected from the material provides information on optical properties such as the complex refractive index. This in turn may lead to an enhanced structural understanding of the material. For example, in the case of aligned molecules such as rubbed or stretched polymers, or liquid crystals, measurement of the linear birefringence or dichroism may be used to determine the average direction of the molecules and provide order parameters that are informative on the orientation distribution. In the case of chiral materials, left- and righted-handed circularly polarized light may be used to assign the sense of the chirality. In more complex cases such as cholesteric liquid crystals [14], photoinduced orientation in polymers [10, 15–17], or chiral sculpted thin films [18, 19], both linear and circular anisotropy may be present. One then needs to probe the linear and circular birefringence and/or dichroism in order to obtain a complete and quantitative description of the material's optical properties and physical and chemical structure.

Spectral analysis of the polarization is useful in many fields. For example, in the ultraviolet and visible region, one can determine the orientation of the electronic transition moments in ordered materials [20]. Likewise, in the mid-infrared, the polarization signature of specific chemical functional groups may be used to determine which components of a chemical structure are ordered, and which ones are isotropically distributed [21]. Even for materials that are transparent in the measured wavelength region, spectral measurements enable models to be fit across multiple wavelengths, thereby providing more reliable optical constants. Various instruments and methods have been designed in order to measure Stokes vectors, which involve polarization modulation, either with one or two photoelastic modulators (PEMs) [11, 22–27] or with a single waveplate at multiple azimuthal angles [28]. Rotating retarder based designs may also spin the waveplate continuously, thereby enabling demodulation of the signals using lock-in amplifiers, as in the PEM-based instruments [29]. There are many accounts of the use of both types of instruments for measurements at single wavelengths, but fewer descriptions of multi-wavelength operation.

In the case of instruments based on tuneable retarders (such as liquid crystals or PEMs), one option for multi-wavelength operation is to set the retardation according to the wavelength of interest [30]. In the case where a continuous spectrum of the Stokes vector elements is desired using such instruments, one option is to step through the retarder settings as the wavelengths are scanned. This is particularly attractive for dispersive instruments using a monochromator or spectrograph, as the wavelengths are scanned sequentially. Multi-wavelength polarimeters have been constructed for X-rays [31], ultraviolet light [32], visible wavelengths [33], near- [34], mid- [35–42], and far-infrared/terahertz [43–52] and microwave [53] frequencies. There have also been designs proposed that are generally applicable to broad regions of the electromagnetic spectrum [54–57]. Operation in the mid-infrared is of great interest to the materials science community, as it offers the possibility of sub-molecular level characterization when resonance frequencies of specific chemical functional groups are targeted for analysis;

however, this is also a challenging spectral region as mid-IR sources (typically heated ceramics) have a weak emission spectrum. This, coupled with only moderate transparency of infrared optics and lower sensitivity of detectors compared to what is available in other spectral regions, creates challenges in the data treatment resulting from the low signal-to-noise ratio. One solution is to use Fourier transform (FT)-based instruments, taking advantage of the higher throughput they offer.

1.6 Variable retarders in the mid-infrared region

Variable retarders are a class of materials which optically retard light by a tuneable amount. Such devices are useful for both research and commercial applications. When fixed to one retardation at a time, variable retarders can be useful for polarization state creation at different wavelengths, or as a light valve which switches on and off based on retarding light by a half-wave. When the retardation is modulated, the retarder can be useful in polarimetry and ellipsometry applications.

Current devices available for variable retardation include mechanical devices such as Babinet-Soleil compensators, electronic devices such as liquid crystals, and devices which utilize the linear or quadratic electro-optic effect of a material, known as Pockels or Kerr cells respectively. Photoelastic modulators, in which the retardation varies periodically at a fixed frequency, can also be considered as a type of variable retarder.

In order to provide a fixed retardation at a tuneable level, the choices for devices are really only Babinet-Soleil compensators (BSCs), or electro-optic devices, as both liquid crystal and photo-elastic modulators are designed to operate with an alternating applied voltage, and are not capable of remaining at a single level of birefringence. A mechanical retarder in the style of a BSC for the mid-infrared would require a birefringent material, and these are quite scarce. An achromatic retarder in the form of a Fresnel rhomb can be used for many of the same applications; however, these are bulky, and impart a jog in the beam path which necessitates reconfiguration of the optical path, and removes the

possibility of switching the retardation on and off efficiently. Therefore, the best option for many applications would be a variable retarder that operates across the mid-IR.

1.7 Theory and origin of the linear electro-optic effect

The term electro-optic effects refers to a list of various different phenomena whereby electricity affects the optical properties of a material. They can be broadly categorized into two types of effects: those that affect the absorption of the material, and those that affect the refractive index and permittivity of a material. Beyond that, though, there is no unifying feature of the effects that can be discussed. Each phenomenon is distinct and unique. For the purposes of this dissertation, the focus is on the Pockels effect and the Kerr effect, two similar phenomena in which applied voltage causes a material to develop birefringence linearly or exponentially, respectively, with respect to the amount of voltage applied. As it is the ordinary and extraordinary refractive indices being affected, these phenomena fit into the latter broad category.

These two electro-optic effects are caused at first due to the fact that an electric field causes the movement of the various ionic constituents to new locations, a deformation of the crystal which is opposed by the restoring force. If the restoring force is not equal along each of a set of three orthogonal axes of the crystal, then the electric field causes anisotropy, which then leads to birefringence.

The Pockels effect, a linear change dependence of birefringence on applied voltage, only occurs in crystals which lack an inversion centre. That is because it is a $\chi^{(2)}$ process, and $\chi^{(2)}$, the second-order susceptibility of a material, is always zero in a centrosymmetric environment.

$$r_{ijk} = -\frac{2}{n_{ij}^4} \cdot \chi_{ijk}^{(2)} \tag{1.9}$$

In all materials, birefringence varies proportionally to the square of the applied voltage as a $\chi^{(3)}$ process, which is known as the Kerr effect. This is generally weak, but when the effect is more significant, the Kerr effect is more prominent, and the material can be used

for electro-optic properties. In a Pockels cell, however, the $\chi^{(2)}$ process is non-zero. Every material displays the Kerr effect to some degree, but every non-centrosymmetric material will show the Pockels effect, which will dominate the Kerr effect and lead to more utility towards applications.

Polarization, P_i where i runs from 1 to 3 (polarization is a three-dimensional vector) of the material is related to the electric field, $E = (E_1, E_2, E_3)$, applied by

$$P_i = \epsilon_0 \left(\sum_j \chi_{ij}^{(1)} E_j + \sum_{jk} \chi_{ijk}^{(2)} E_j E_k + \sum_{jkl} \chi_{ijkl}^{(3)} E_j E_k E_l + \dots \right) \tag{1.10}$$

In the above, i, j, k and l all run from 1 to 3, conventionally referring to the x, y and z directions respectively. In the case of an electric field applied along just one of these axes, all terms except for those where j=k=l will equal 0. For linear media, $\chi^{(1)}$ is much larger than $\chi^{(2)}$ or $\chi^{(3)}$, and thus the polarization varies linearly with electric field. In a centrosymmetric environment, the $\chi^{(2)}$ terms can always be ignored. Because $\chi^{(2)}$ is typically more significant than $\chi^{(3)}$ in non-linear materials, Pockels cells usually require much smaller applied voltages than Kerr cells.

About $E = 0$, the relationship between electric field and the refractive index can be expanded as a Taylor series.

$$n(E) = n_0 + a_1 E + \frac{1}{2} a_2 E^2 + \dots \tag{1.11}$$

In this treatment, n_0 refers to $n(0)$, the refractive index of the material in the absence of any electric field.

Conventionally, two electro-optic coefficients are defined as $r = -2a_1/n_0^3$ and $s = -a_2/n_0^3$. This convention allows rewriting of the initial equation (the terms after E^2 are negligible) as

$$n(E) = n_0 - \frac{1}{2} r n_0^3 E + \frac{1}{2} s n_0^3 E^2 \tag{1.12}$$

The electric impermeability is perhaps more pertinent here than the refractive index. The electric impermeability, which is the inverse of permittivity, is defined as

$$\eta = \frac{\epsilon_0}{\epsilon} = \frac{1}{n_0^2} \tag{1.13}$$

j	**i**:1	2	3
1	1	6	5
2	6	2	4
3	5	4	3

Table 1.1: Lookup table for the index I that represents the pair of indices (i, j)

which leads to

$$\eta = \eta(0) + rE + sE^2 \tag{1.14}$$

Electric impermeability, which informs the index ellipsoid (aka the indicatrix) is a 3×3 tensor, and each element η_{ij} is dependent on the electric field, which itself has three components; $E = (E_1, E_2, E_3)$. The expression for each η_{ij} is

$$\eta_{ij}(E) = \eta_{ij}(0) + \sum_{k=1}^{3} r_{ijk}E_k + \sum_{k=1}^{3}\sum_{l=1}^{3} s_{ijkl}E_kE_l \tag{1.15}$$

So based on the above, r is a $3 \times 3 \times 3$ tensor, and s is a $3 \times 3 \times 3 \times 3$ tensor. Due to symmetry considerations, all 27 elements of r and all 81 elements of s are not unique, however. The tensors are invariant under permutations of i and j, and in the case of s, k and l. Because of this, the subscripts can be reduced from r_{ijk} with i, j and k running from 1 to 3 to r_{Ik} with I running from 1 to 6 and k running from 1 to 3. Similarly, s_{ijkl} can be written as s_{IK} with both I and K running from 1 to 6. The scheme is shown in Tab. 1.1.

r and s are known as the linear (Pockels) and quadratic (Kerrs) electro-optic coefficients. A commonly measured coefficient for a Pockels cell is the r_{41} coefficient. As can be seen, r_{41} is the short form of r_{231} or r_{321}, and dictates how the $(2, 3)$ and $(3, 2)$ element of the impermeability matrix is affected by the first component of the electric field. Which Pockels coefficients are pertinent to a given material is based on the crystal space group. For example, below are the applicable Pockels coefficients for three space groups.

1.8 Cadmium zinc telluride

The original common materials for Pockels cells are ammonium dihydrogen phosphate, potassium dihydrogen phosphate or potassium dideuterium phosphate. More recently,

$$\begin{bmatrix} 0 & 0 & 0 \\ 0 & 0 & 0 \\ 0 & 0 & 0 \\ r_{41} & 0 & 0 \\ 0 & r_{41} & 0 \\ 0 & 0 & r_{41} \end{bmatrix} \quad \begin{bmatrix} 0 & 0 & 0 \\ 0 & 0 & 0 \\ 0 & 0 & 0 \\ r_{41} & 0 & 0 \\ 0 & r_{41} & 0 \\ 0 & 0 & r_{63} \end{bmatrix} \quad \begin{bmatrix} 0 & -r_{22} & r_{13} \\ 0 & r_{22} & r_{13} \\ 0 & 0 & r_{33} \\ 0 & r_{51} & 0 \\ r_{51} & 0 & 0 \\ -r_{22} & 0 & 0 \end{bmatrix}$$

Cubic $\bar{4}3m$ [e.g. GaAs, CdTe, CZT] | Tetragonal $\bar{4}2m$ [e.g., KDP, ADP] | Trigonal $3m$ [e.g., $LiNbO_3$, $LiTaO_3$]

compounds of Group II and Group VI elements, known as II-VI compounds, have been used for this application, featuring wider bandgaps and greater density. The material with the highest r_{41} coefficient of all measured II-VI compounds is cadmium telluride (CdTe), at 6.8×10^{-12} m/V [58].

Cadmium zinc telluride (CZT) is a crystalline compound which is an alloy of cadmium telluride and zinc telluride. In terms of composition, CZT samples are often referred to as $Cd_{1-X}Zn_XTe$, with X referring to the proportion of zinc substituted for cadmium with respect to CdTe. Typically, X ranges up to 0.20, with the most common value being 0.1 [3]. Like CdTe, CZT has a zinc-blende structure, and belongs to the $\bar{4}3m$ space group, shown in Fig. 1.2.

CZT shares, and slightly improves upon, many of the characteristics that make CdTe such an ideal semiconductor for nuclear detection, such as high resistivity, wide band-gap and high density. The issue that has held back the progress of these materials for both electro-optic and semiconductor applications is the difficulty of producing high-quality crystals. Sample uniformity and homogeneity remain issues, but several advances have been made in the past few decades in this regard [59]. CdTe's function as a Pockels cell material that is transparent from 2–10 μm has been documented in the literature [60], while CZT, to this point, has not been thoroughly characterized in the literature. Due to its slightly more favourable material properties, CZT holds promise as an even more suitable material for Pockels cells operating across the mid-IR.

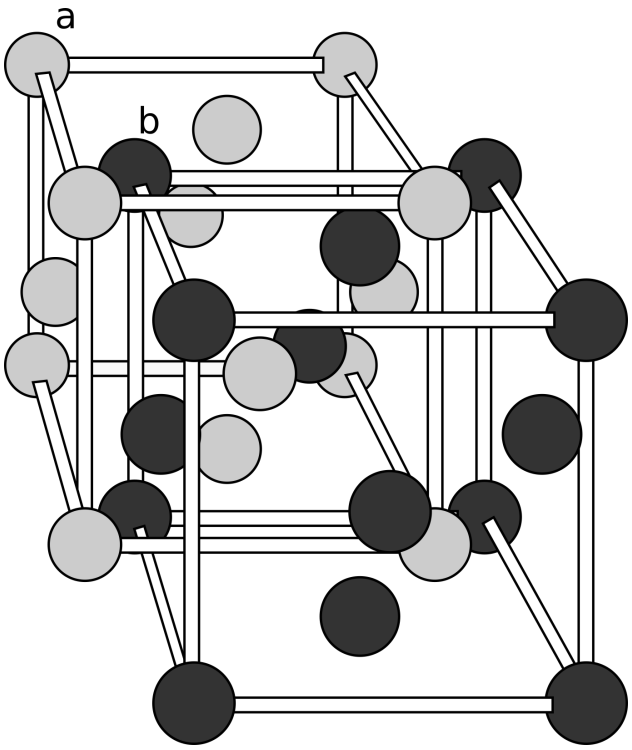

Figure 1.2: Crystal structure of a zinc blende compound such as CZT. In CdTe, ZnSe and other such compounds with two components, one element will be (a) and the other (b) in the figure. CZT is an alloy of CdTe and ZnTe, and in its crystal structure, Te will occupy (a) sites, while the (b) sites are split between Cd and Te in some specified proportion.

1.9 Scope of dissertation

There are several challenges which make optical work in the mid-infrared portion of the electro-magnetic spectrum difficult. A scarcity of materials and their general inefficiency compared to what is available in other spectral regions causes limitations that have prevented the emergence of new technologies and devices for this region. In the following dissertation, I first consider thin films on electronic devices and substrates used in optical measurements. I will introduce a new instrument for polarization state measurement across the mid-IR. I then apply that instrument, along with various other optical techniques and methodologies, to investigate cadmium zinc telluride (CZT) and its potential for use in mid-IR electro-optic devices, both with DC and AC applied voltage.

Chapter 2

Polarimetry studies on thin film interfaces

For any electronic or optical device, the characteristics of the surface are of utmost importance for the device's functionality. In many metallic and crystalline materials, the surface becomes naturally oxidized when exposed to air. This leads to a thin layer with, in many cases, very different properties, and thin films can interfere with optical analysis techniques. This factor needs to be accounted for when the situation arises, as otherwise it can lead to biases in measurements.

With electronic device materials, the nature of the surface film can be a key element in optimization of the device, and so methods to study and monitor the thin film on samples are important. The interference problem that thin films pose to certain optical techniques can be targeted for analysis by other techniques, as these films have predictable effects on light when reflected or transmitted, provided that certain constants of the materials involved are known.

2.1 Multiple-beam interference in thin films

When a beam of light encounters a surface which features a thin film, some of the light is reflected at the top-most surface, while the rest, assuming it isn't absorbed, is transmitted into the thin film. The transmitted light then encounters the bottom surface of the film, and once again is divided into a reflected and a transmitted component. The light bounces

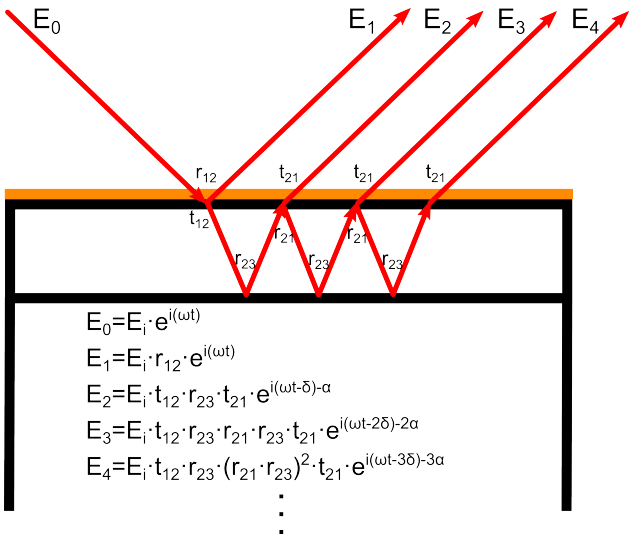

Figure 2.1: Multiple-beam interference arising from reflection off of a surface with a non-opaque thin film. Here, a yellow layer on top is the target of optical analysis, but the reflected beam is a summation of beams with different paths.

back and forth from the top to the bottom of the thin film, and on each bounce, loses a portion of its intensity via transmission through the top and bottom interface, respectively. The light which is collectively reflected off of the surface of the material is a summation of the initially reflected beam off the top surface, as well as any portions of the light which transmit through the top surface from within the thin film. The light that can be seen as transmitted through the overall system comprises all of the portions of the light which end up transmitted through the bottom surface, and also are transmitted through the material below, where applicable.

For a polarized light source, the summation of the various beams of light which contribute to the overall reflected (or transmitted) beam involves constructive or destructive interference, depending on the phase delay between each portion of the light. This phase delay depends on the thickness of the film and the incident angle, as well as the refractive indices of all of the layers of the system. Thus the amount of reflection or transmission can be used as a sensitive probe of any of these refractive indices or the thickness of the thin film.

In addition, the summation of the various beams of light is also affected by the different

Fresnel reflection and transmission coefficients upon each interface the beam encounters. If the light has components both within and perpendicular to the plane of reflection, then different amounts of each component are reflected and transmitted. The polarization state of the reflected or transmitted light is thus also sensitive to the factors that affect the characteristics of the multiple-beam interference, and the nature of the multiple-beam interference is dependent on what the incident polarization state is.

2.2 Characterization of CZT oxide thickness

2.2.1 Introduction

Cadmium zinc telluride is used primarily as a radiation detector, and also has potential to be useful as an electro-optic modulator. In either of these pursuits, high resistivity of the material is key, and this is dependent in a large way on the characteristics of the surface. In ambient conditions, the surface of CZT develops a natural oxide layer. The uniformity and thickness of this layer can be tailored by various techniques which involve removing native surface oxide and allowing it to grow in carefully controlled conditions, such as in a plasma passivation chamber.

Ellipsometry can be used to study the growth of the oxide layer due to the multiple-beam interference phenomenon. In our work, we have used a Stokes polarimeter to measure the polarization state of a 633 nm laser after reflection off the surface of CZT samples. The light is initially polarized at 45°, such that there are equal s- and p-components to the light. Upon reflection, the polarization state is a summation of the several fractions of the light which exit the top surface after increasing numbers of bounces within the oxide film, and the Stokes vector depends on the thickness of the material, and the angle of incidence of the light. The instrumental scheme is seen in Fig. 2.2.

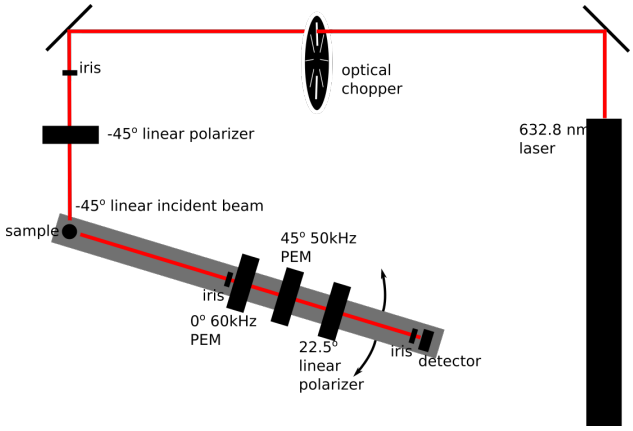

Figure 2.2: The instrumental scheme used for oxide thickness measurement via ellipsometry. The 633 nm laser source is directed through a series of polarization state generation optics. A linear polarizer and quarter-wave plate are used initially to create circularly polarized light, which ensures that any linear state will have equal intensity. The light is then polarized before reflecting off of the sample. The reflected light is directed into the Stokes polarimeter.

2.2.2 Theory

The expectation was that the oxide film which exists naturally was in the order of 0–10 nm, so I developed a model to see whether the method would be sensitive enough to see it. The light is considered as two components, the s- and the p-component, which are treated separately, before being recombined at the end to determine the Stokes vector. As shown in Fig. 2.1, the magnitude and phase of each component of the reflected beam is described fairly simply by the expression for the incident beam, and all necessary Fresnel coefficients. We must consider two equations for each beam, however, as the two components of the light have a different set of Fresnel coefficients.

This readily lends itself to Jones calculus, where the polarized light is described by a two-element Jones vector, and any encountered interfaces are described by a 4×4 Jones matrix. In this formalism, the first element of the Jones vector is the magnitude and phase of the x-component of the light, and the second element is the magnitude and phase of the y-component of the light.

$$E = \begin{bmatrix} E_x e^{i\phi_x} \\ E_y e^{i\phi_y} \end{bmatrix} \tag{2.1}$$

In an experiment when light encounters a surface at non-normal incidence, s- and p-polarizations are defined with respect to the plane of incidence of the light, dependent on its orientation relative to the incoming light. The plane of incidence is defined by the vector of the incident beam propagation, and the vector normal to the surface. Light polarized in this plane is considered p-polarized, while light polarized in a direction orthogonal to this plane is s-polarized. E_x and E_y can be defined such that E_y is the s-polarized component, and E_x is the p-polarized component. Thus

$$E = \begin{bmatrix} E_p e^{i\phi_p} \\ E_s e^{i\phi_s} \end{bmatrix} \tag{2.2}$$

If a cumulative, complex coefficient can be worked out that describes the multiple-beam interference on reflection for each component, then the resultant Jones vector of the reflected beam, E', can be described simply. These cumulative reflection coefficients can be denoted by $\tilde{r_p}$ and $\tilde{r_s}$. The magnitude and phase of the s- and p-polarized components of the light are equal in the experiment, as 45° incident light is used. Therefore, I can write the Jones matrix representing the reflection process, treating the two elements of the Jones vector separately, each with their own coefficient. The p-polarized component also gets mirrored in reflection, which is accounted for in the Jones matrix by a negative sign.

$$J = \begin{bmatrix} -\tilde{r_p} e^{i\phi} & 0 \\ 0 & \tilde{r_s} e^{i\phi} \end{bmatrix} \tag{2.3}$$

In order to determine the value of $\tilde{r_p}$ and $\tilde{r_s}$, which can be referred to simply as $\tilde{r}$ without restricting generality, I need to consider the equations of all of the beams contributing to the reflected light. I consider each component of the incident light (either the s- or p-polarized component) to be $E_0 = e^{i\phi}$. With reference to Fig. 2.1, I can describe the resultant beams using that component's Fourier reflection coefficients for the magnitude, and the beam's added path length for the phase.

The Fresnel reflections coefficients are written in shorthand notation as r_{ab}, where a and b refer to the layers of incidence and transmission, respectively. In the case of my CZT oxide work, the first layer is air, the second CZT oxide and the third CZT. These coefficients

can be calculated, knowing the refractive indices for the material and the incident angle, using the Fresnel equations, which are different for s- and p- light.

$$r_{s,ab} = \frac{n_a \cos\theta_a - n_b \cos\theta_b}{n_a \cos\theta_a + n_b \cos\theta_b} \tag{2.4a}$$

$$t_{s,ab} = \frac{2n_a \cos\theta_a}{n_a \cos\theta_a + n_b \cos\theta_b} \tag{2.4b}$$

$$r_{p,ab} = \frac{n_b \cos\theta_a - n_a \cos\theta_b}{n_a \cos\theta_b + n_b \cos\theta_a} \tag{2.4c}$$

$$t_{p,ab} = \frac{2n_a \cos\theta_a}{n_a \cos\theta_b + n_b \cos\theta_a} \tag{2.4d}$$

Using these Fresnel coefficients, I work out the equations for either the magnitude of the s- or p-polarized components of the light. For the phase, I consider that after the top-reflected beam, E_1, each beam can be considered to be delayed by an additional phase of δ.

$$\delta = \frac{2\pi L}{\lambda} \tag{2.5}$$

This δ depends on the path difference of one beam from the last, L, as well as the wavelength of the light.

$$L = 2n_2 d \cos\theta_1 \tag{2.6}$$

The path difference depends on the thickness of the oxide layer, and the incident angle, which in combination with the various refractive indices provides the angle of the beam's travel within the thin film. The real part of the refractive index of CZT was measured to be 3.01, while a value of 1.8 for CZT oxide was provided by measurements made by the manufacturing company, Redlen.

This gives all of the components necessary to describe the expressions for the reflected

beam.

$$E_1 = r_{12}e^{i\phi} \tag{2.7a}$$

$$E_2 = t_{12}r_{23}t_{21}e^{i(\phi-\delta)} \tag{2.7b}$$

$$E_3 = t_{12}r_{23}r_{21}r_{23}t_{21}e^{i(\phi-2\delta)} \tag{2.7c}$$

$$E_4 = t_{12}r_{23}(r_{21}r_{23})^2t_{21}e^{i(\phi-3\delta)} \tag{2.7d}$$

$$E_n = t_{12}r_{23}(r_{21}r_{23})^{n-2}t_{21}e^{i(\phi-(n-1)\delta)}, n \geq 2 \tag{2.7e}$$

The summation of these terms is thus simply

$$\begin{aligned} E' &= r_{12}e^{i\phi} + \sum_{n=1}^{\infty} t_{12}r_{23}(r_{21}r_{23})^{n-1}t_{21}e^{i(\phi-n\delta)} \\ &= e^{i\phi}\left(r_{12} + \frac{t_{12}r_{23}t_{21}e^{i\delta}}{1 - r_{21}r_{23}e^{-i\delta}}\right) \end{aligned} \tag{2.8}$$

This then provides that $\tilde{r}$ is

$$\tilde{r} = r_{12} + \frac{t_{12}r_{23}t_{21}e^{i\delta}}{1 - r_{21}r_{23}e^{i\delta}} \tag{2.9}$$

I turn my attention back to the Jones matrix of the reflection process, described earlier in Eq. 2.3. As I am doing the measurement with a Stokes polarimeter, I need to simulate the data in terms of a Stokes vector, which requires first converting this Jones matrix to a Mueller matrix. This can be done using a transformation involving the Kronecker product of the Jones matrix, provided that the Jones matrix is non-depolarizing.

$$M = \begin{bmatrix} 1 & 0 & 0 & 1 \\ 1 & 0 & 0 & -1 \\ 0 & 1 & 1 & 0 \\ 0 & i & -i & 0 \end{bmatrix} (J \otimes J^*) \begin{bmatrix} 1 & 1 & 0 & 0 \\ 0 & 0 & 1 & i \\ 0 & 0 & 1 & -i \\ 1 & -1 & 0 & 0 \end{bmatrix} \tag{2.10}$$

Knowing that the Stokes vector of the incident light, which is linearly polarized at 45°, is $\mathbf{s} = \begin{bmatrix} 1 & 0 & 1 & 0 \end{bmatrix}^T$, Mueller matrix algebra can be used to compute the simulated resultant Stokes vector, $\mathbf{s}'$.

$$\mathbf{s}' = M\mathbf{s} \tag{2.11}$$

2.2.3 Experiment and Results

Given that, experimentally, the incident angle can be set to be anything, I only have one value to compute, which is thickness. Due to the difficulty in solving analytically for thickness in the simulated Stokes vector of the resultant light, it is easier to obtain the result by optimizing a proposed value of thickness, and finding the best value to match the data. This method of fitting is much more precise with multiple data points to fit, and therefore I varied the incident angle and took multiple measurements in the range of 45°–80°.

This process can be visualized in Fig. 2.3. The lines in the figure show the simulated data for thicknesses from 2–12 nm in 2 nm incriments. The first panel shows the expected light intensity at the detector, but the actual data are the normalized Stokes vectors, which are shown in the other three spectra (normalized to s_0). It becomes clear that s_1 and s_2 are not sensitive enough to the thickness to be useful in this experiment; however, s_3 shows high sensitivity and a steady increase in peak minimum in this thickness range. The data points for s_3 fall between the simulation lines for 6 and 8 nm. A fit optimization routine determines that this sample's oxide thickness is 6.9 nm.

2.3 Multiple-beam interference effects on methyl group tilt-angle determination via SFG

In the previous section, I used an optical method to characterize the oxide thin film on CZT. In this section, I analyze the impact of a thin film on an optical technique. In particular, when sum-frequency generation spectroscopy is performed using reflection off a substrate containing a thin film. In this work, I address systems where the SFG signal originates only from adsorbed layers at the polymer–air interface [61–65]; for example, a substrate that does not produce SFG on its own, and a deuterated polymer with negligible non-resonant contribution. This situation is illustrated in Fig. 2.4, noting that SFG therefore originates only from the adsorbed molecules, taking the methyl symmetric stretch as an example. I consider the case of two commonly used substrates, glass and silicon. Glass

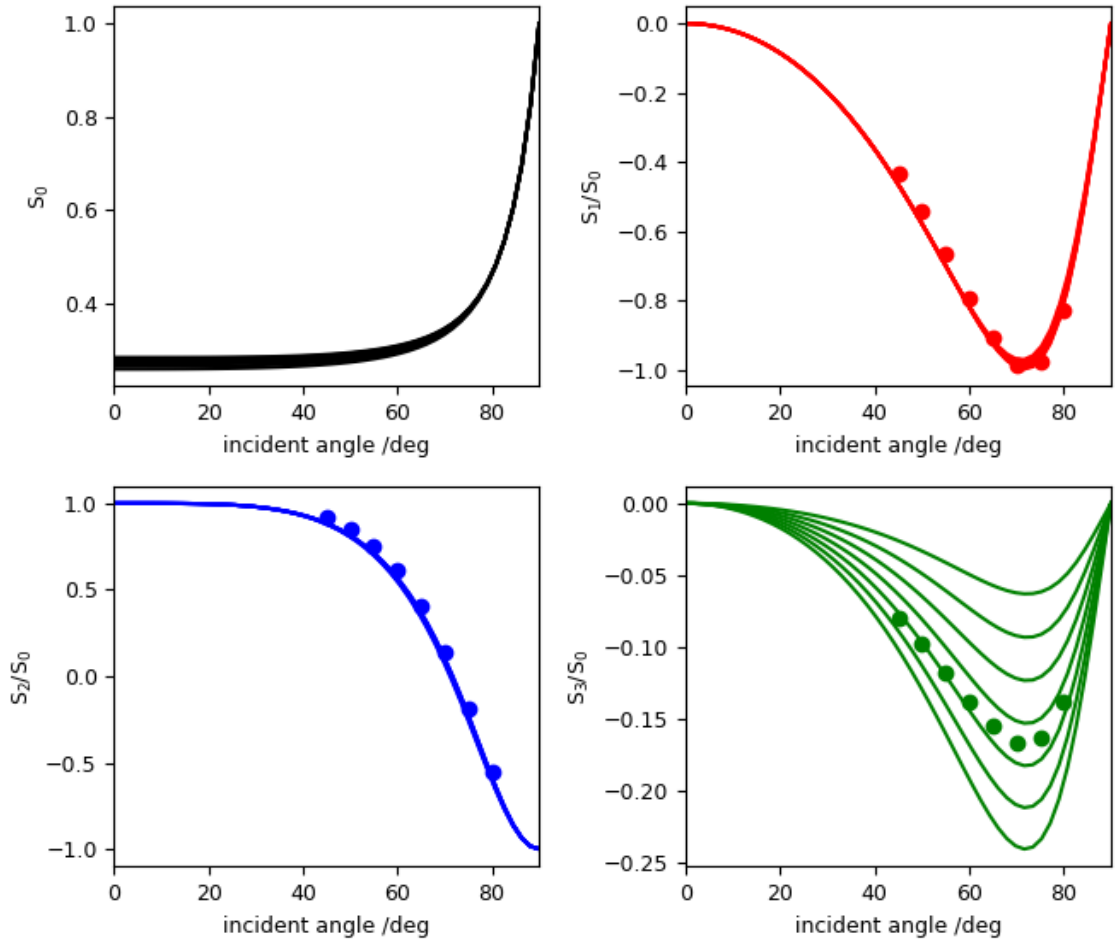

Figure 2.3: Polarimetry measurement of the thickness of the oxide layer on CZT. For a series of thicknesses from 2 nm to 12 nm, in steps of 2 nm, the variation in the Stokes vectors resulting from reflection at different incident angles are shown. The s_0 curve, representing total intensity, in the upper left panel increases with increasing incident angle, so the data is normalized to this to better appreciate the shape of the Stokes elements themselves.

is inexpensive and disposable, although even IR-grade (low water content) fused silica has limited transparency in the mid-IR. Nevertheless, it is widely used for studies in the C–H and O–H stretching region. Silicon is also a common SFG substrate [66–71], but has a strong absorption in the visible region, as typical visible and SFG frequencies are above the band gap. As a result, there is an appreciable nonresonant contribution. However, there has been significant interest in suppressing the nonresonant contribution for a more detailed analysis of adsorbate vibrational modes; several examples have been for Si specifically

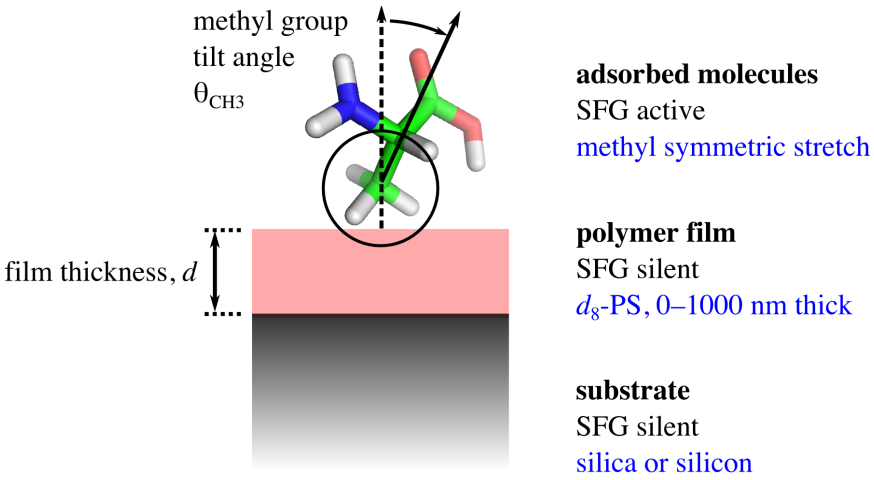

Figure 2.4: A substrate–film–adsorbate system where the SFG signal originates only from the molecules adsorbed to the film.

[72]. I will first describe the basis of including multiple beam interference in the local field corrections, and then illustrate its effect on structure determination of adsorbed molecules.

2.3.1 Background Theory

In an SFG experiment, the measured signal is proportional to the square of the magnitude of the effective second-order susceptiblity. The 27 elements of $\chi^{(2)}_{\text{eff}}$ are related to the $\chi^{(2)}$ tensor elements though

$$\chi^{(2)}_{\text{eff},ijk} = L^{\text{SFG}}_{ii} e^{\text{SFG}}_i \cdot \chi^{(2)}_{ijk} \cdot L^{\text{vis}}_{jj} e^{\text{vis}}_j \cdot L^{\text{IR}}_{kk} e^{\text{IR}}_k \tag{2.12}$$

where $\mathbf{L}$ are the macroscopic local field corrections describing how fields at the surface are related to the incoming visible/IR pump beams, and the SFG beam detected in the far field. In a two-phase interface, these are given by [73]

$$\mathbf{L} = \begin{bmatrix} 1 - r_p & 0 & 0 \\ 0 & 1 + r_s & 0 \\ 0 & 0 & 1 + r_p \end{bmatrix} \tag{2.13}$$

where r_s and r_p are the simple Fresnel reflection coefficients that depend on the angle of incidence, and the refractive indices of the two media [7]. The factors $\mathbf{e}$ in Eq. 2.12 are the unit polarization vectors that project the incoming and outgoing fields from the s/p frame

into the x, y, z Cartesian coordinates

$$\mathbf{e} = \begin{bmatrix} \pm\cos\theta \\ 1 \\ \sin\theta \end{bmatrix} \tag{2.14}$$

for the co-propagating geometry, where e_x is positive for the visible and infrared beams, and negative for the SFG beam [74]. When the interface of interest is air–polymer, the quantities in Eq. 2.13 are typically determined from

$$r_s^{a,f} = \frac{n_a \cos\theta_a - n_f \cos\theta_f}{n_a \cos\theta_a + n_f \cos\theta_f} \tag{2.15a}$$

$$r_p^{a,f} = \frac{n_f \cos\theta_a - n_a \cos\theta_f}{n_a \cos\theta_a + n_f \cos\theta_f} \tag{2.15b}$$

using $n_a = 1$ as the refractive index of air, and the appropriate frequency-dependent values of n_f according to the polymer film of interest. However, if I consider that the film is deposited on a substrate with refractive index n_s, the reflection of fields incident from the air side is described by

$$\tilde{r} = r^{a,f} + \frac{t^{a,f} \cdot t^{f,a} \cdot r^{f,s} \cdot e^{-i\delta}}{1 - r^{f,a} \cdot r^{f,s} \cdot e^{-i\delta}} \tag{2.16}$$

where t are the standard Fresnel transmission coefficients,

$$t_s^{a,f} = \frac{2n_a \cos\theta_a}{n_a \cos\theta_a + n_f \cos\theta_f} \tag{2.17a}$$

$$t_p^{a,f} = \frac{2n_a \cos\theta_a}{n_a \cos\theta_f + n_f \cos\theta_a} \tag{2.17b}$$

δ is the phase change due to the optical path difference

$$\delta = \frac{4\pi}{\lambda} n_f d \cos\theta_f \tag{2.18}$$

with d as the film thickness, θ_f the refracted angle in the polymer film, and λ the wavelength of the corresponding beam [7]. For clarity, I have omitted the polarization superscripts. $\tilde{r}^s$ is calculated using r^s and t^s in Eq. 2.16, while $\tilde{r}^p$ is obtained by using r^p and t^p in the same expression. I therefore construct a set of expressions analogous to Eqs. 2.13 where $\tilde{\mathbf{L}}$ are

Table 2.1: Values of refractive indices corresponding to $\lambda_{\mathrm{SFG}} = 461$ nm, $\lambda_{\mathrm{vis}} = 532$ nm, $\lambda_{\mathrm{IR}} = 3.47$ μm.

material	n_{SFG}	n_{vis}	n_{IR}
d_8-PS	1.612	1.599	1.550
silica	1.465	1.461	1.419
silicon	4.659 + 0.145i	4.152 + 0.0518i	3.432

defined using Eq. 2.16 in place of Eqs. 2.15a.

$$\tilde{L}_{xx} = 1 - \tilde{r}_p \tag{2.19a}$$

$$\tilde{L}_{yy} = 1 + \tilde{r}_s \tag{2.19b}$$

$$\tilde{L}_{zz} = 1 + \tilde{r}_p \tag{2.19c}$$

In this study, I have considered the thin film to be perdeuterated polystyrene, with thickness up to 1 μm. This is the range of film thickness easily achievable by spin coating, drop coating, dipping, and other common preparation methods. Fused silica was considered as a common substrate material. Silicon was also considered as it represents a high refractive index case and is widely used in cases where surface flatness is important. Values of the refractive index at the methyl symmetric stretching frequency ($\omega_{\mathrm{IR}} = 2880\,\mathrm{cm}^{-1}$) are given in Table 1.

2.3.2 Consequences for orientation determination

Although it is possible to determine the orientation of chemical functional groups by comparing two or more vibrational modes associated with a fixed axis or plane in the molecule [75], this requires knowledge of the ratio of those two different hyperpolarizability tensor elements. It is therefore preferred to compare the SFG intensity of the same mode in two or more polarization schemes. We will consider the methyl symmetric stretch as an example, as it is a commonly observed mode, and there have been many models proposed for its molecular response. I will use $R \equiv \alpha^{(2)}_{aac}/\alpha^{(2)}_{ccc} = 2.5$, previously reported

as a typical value [73, 76]. This provides

$$\chi^{(2)}_{yyz} = \frac{N}{2\varepsilon_0}\left[(1+R)\langle\cos\theta_{\mathrm{CH3}}\rangle - (1-R)\langle\cos^3\theta_{\mathrm{CH3}}\rangle\right] \tag{2.20}$$

which may be used to calculate the ssp spectral intensity according to

$$I_{ssp} \propto |\tilde{L}^{\mathrm{SFG}}_{yy}\cdot\tilde{L}^{\mathrm{vis}}_{yy}\cdot\tilde{L}^{\mathrm{IR}}_{zz}\cdot\chi^{(2)}_{yyz}|^2 \tag{2.21}$$

and

$$\chi^{(2)}_{yzy} = \frac{N}{2\varepsilon_0}(1-R)\left[\langle\cos\theta_{\mathrm{CH3}}\rangle - \langle\cos^3\theta_{\mathrm{CH3}}\rangle\right] \tag{2.22}$$

for the determination of the sps response in

$$I_{sps} \propto |\tilde{L}^{\mathrm{SFG}}_{yy}\cdot\tilde{L}^{\mathrm{vis}}_{zz}\cdot\tilde{L}^{\mathrm{IR}}_{yy}\cdot\chi^{(2)}_{yzy}|^2. \tag{2.23}$$

Fig. 2.5 shows a plot of I_{sps}/I_{ssp} as function of the methyl group tilt angle. Results obtained for a polystyrene film thickness of 50 nm are indicated with the fine dashed line, and for 500 nm with the coarse dashed line. In both cases the substrate is silica. For comparison, ignoring multiple beam interference by treating this as a two-phase air–polymer system (using L in place of $\tilde{L}$ in Eqs. 2.21 and 2.23) produces the curve drawn with the solid line. A few illustrative scenarios are highlighted. The first corresponds to an intensity ratio determined in the experiment to be 0.45. If multiple beam interference were not taken into account, there would be no intersection with any methyl tilt angle, as the entire solid curve lies under this value. However, if the film is known to be 50 nm thick, the tilt angle of 82° can be recovered. If the ratio instead was determined to be 0.41, the two-phase analysis would result in a misinterpretation of $\theta_{\mathrm{CH3}} = 80^\circ$, when in fact it is 75° on the 50 nm film, an error of 5°. As a final example, a ratio of 0.34 corresponds to $\theta_{\mathrm{CH3}} = 63^\circ$ for a 50 nm film, or 74° on a 500 nm film. Ignoring multiple beam interference would incur errors of $+2^\circ$ or -9°, respectively. This information is summarized in Fig. 2.5b for a range of film thickness up to 1 μm, as this easily achievable using common spin coating conditions. Warm colours indicate the amount that measurements that neglect MBI

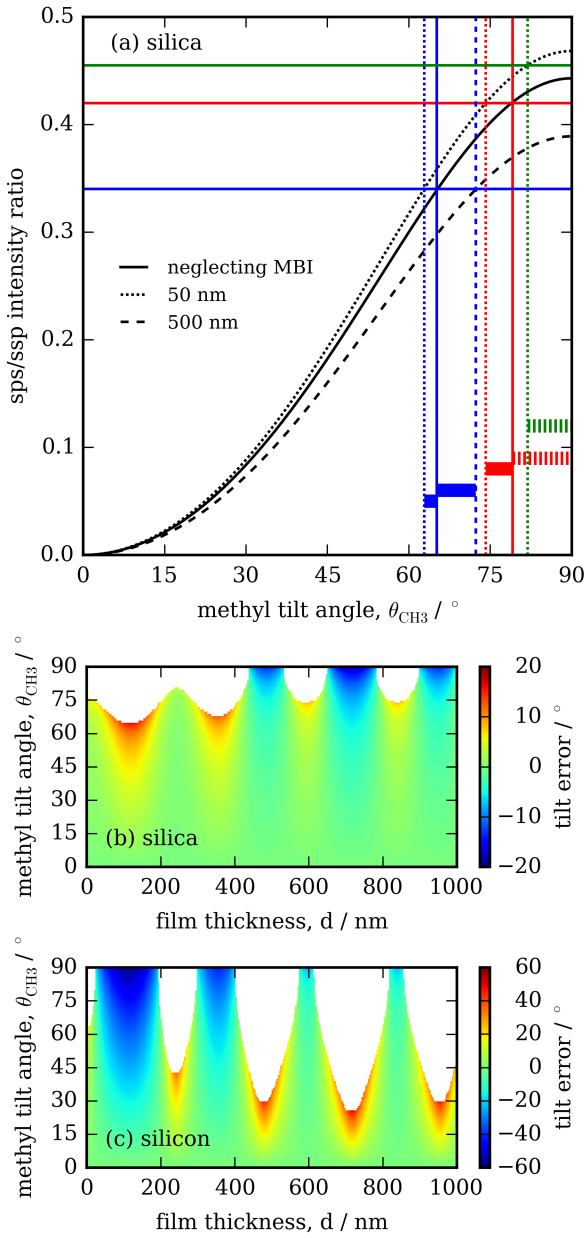

Figure 2.5: (a) Effect of multiple beam interference on methyl group tilt angle determination, for molecules adsorbed at the air–polystyrene thin film interface, on a silica substrate. For a given sps/ssp SFG intensity ratio, the fine dashed curve is used to determine the molecular tilt angle in the case of a 50 nm film, and the wide dashed curve in the case of 500 nm. If multiple beam interference were ignored, the tilt angle would be determined from the solid curve. These errors in tilt angle are summarized in (b) for a silica substrate and (c) for a silicon substrate. Colours indicate the difference between the actual methyl tilt angle, and what would be determined without considering multiple beam interference.

overestimates the tilt angle; cold colours describe the magnitude of the underestimation. White areas of the plot indicate that no solution exists without explicit consideration of MBI, as in the case of the green line in Fig. 2.5a. In Fig. 2.5b, the same calculation is performed, but with silicon as the substrate on top of which the film has been deposited. Here it can be seen that the chance of obtaining a correct measurement of the tilt angle is significantly lower, and the chance of not finding a suitable tilt angle to match the data is much higher. These findings show that analysis of SFG signals from an air–polymer–substrate system are significantly influenced by the thickness of the polymer layer. The amount of error incurred by ignoring the thin-film interference is dependent on the refractive index difference between the polymer and the substrate, but in a common low-difference scenario (polymer and substrate nearly index matched, as shown in Fig. 2.5b) the error is shown to be $\pm 10^{\circ}$ across most methyl tilt angles. When substrate and polymer refractive indices differ significantly as in Fig. 2.5c, the elucidation of tilt angle becomes extremely erratic, with errors of $\pm 40^{\circ}$ incurred across much of the range, and a strong possibility of not finding a solution.

This analysis is not limited to adsorbed species on thin films, but also pertains to studies of the surface structure of the films themselves. In studies seeking to elucidate the structural features of air–polymer interfaces, it is common to justify the specificity of the signal for the air–polymer interface, ruling out contributions from the buried polymer–substrate surface. One method of illustrating this is to prepare films of different thicknesses and monitor the variation of SFG response as a function of thickness [77, 78]. As an example, Chen *et al.* reported only small variations in SFG, as the thickness of a polyurethane film varied. The authors posited that if an SFG signal was being produced by the polymer–substrate interface as well, it would be stronger with thinner samples as less absorption of the IR beam would have occurred on its way through the polymer layer. It was purported that the observed variations were due to uncontrollable molecular-level differences between samples. However, my findings show that the variation in signal is on the order of

what we would predict for an air–polymer–glass system upon inclusion of multiple beam interference [77].

2.3.3 Interpretation of spectral phase

The above results are based on an elucidation of the methyl tilt angle in the range $0^\circ < \theta_{\mathrm{CH3}} < 90^\circ$. As SFG is based on an even order $\chi^{(2)}$ susceptibility tensor, it is sensitive to the polarity of the direction, and can separate chemical groups pointing up to the air from those directed towards the substrate ($90^\circ < \theta_{\mathrm{CH3}} < 180^\circ$). The resolving this quadrant ambiguity requires two steps: measuring the phase of the complex-valued $\chi^{(2)}$ tensor on resonance with the mode of interest, and knowing the sign of the corresponding hyperpolarizability tensor $\alpha^{(2)}$ elements. In the case of the methyl group, it has been determined that $\alpha^{(2)}_{aac} > 0$ and $\alpha^{(2)}_{ccc} < 0$ [79]. Using this knowledge, if $\mathrm{Im}\chi^{(2)} < 0$ in ssp polarization on a two-phase system (air–polymer), I know that the methyl groups are directed towards the air. However, it must be pointed out that the experiment directly measures the phase of the effective susceptibility $\chi^{(2)}_{ssp}$ (Eq. 2.12); this is related to the actual susceptibility by the product of the local field corrections L or $\tilde{L}$. Fig. 2.6 plots the phase of the complex-valued $\tilde{L}^{\mathrm{SFG}}_{yy} \cdot \tilde{L}^{\mathrm{vis}}_{yy} \cdot \tilde{L}^{\mathrm{IR}}_{zz}$ as a function of the polymer film thickness. The results for the silica substrate (blue line) indicate that, depending on the polystyrene thickness, the local field corrections contribute an additional $\pm 15^\circ$ to the phase of $\chi^{(2)}_{yyz}$. If the substrate were silica, the additional phase may lead or lag by more than 90°. Neither of these cases display a large enough phase contribution (not close enough to 180°) to alter the assignment of the polarity of an isolated function group. However, as the phase of $\chi^{(2)}$ changes by 180° as it passes through a normal mode resonance, the superposition of closely spaced modes may alter the phase measured at the frequency of the methyl symmetric stretch ($\pm 90^\circ$ in the isolated case). For this reason, it is useful to know how much MBI contributes to the phase of the effective susceptibility through the local field corrections.

In a study of the air–polystryene interface, Briggman *et al.* have varied the thickness

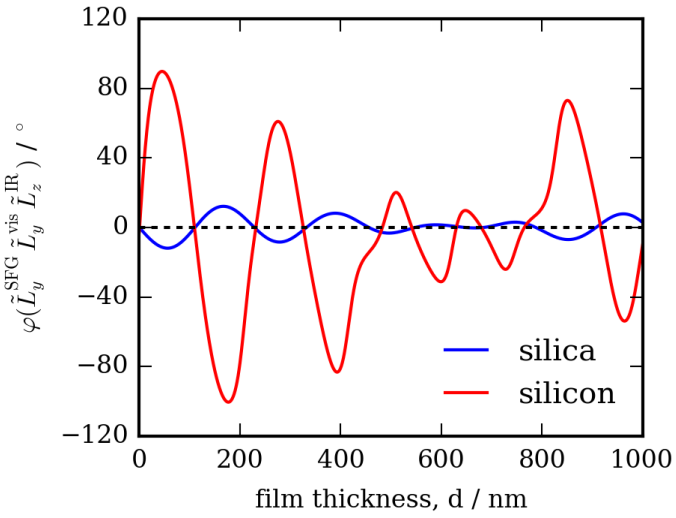

Figure 2.6: Phase of the LLL prefactor that determines the phase of $\chi^{(2)}_{\mathrm{eff}}$ as a function of the polystyrene thickness. Results for the silica substrate are shown in blue; those for silicon in red. The horizontal dashed line indicates the zero-phase result for the air–polystyrene system.

of the polymer films deposited on silicon substrate with native SiO_2 overlayer [80]. They have reported a phase difference between the resonant and nonresonant contributions in the range of 0–12 rad as the polystyrene thickness varies from 0–450 nm. Even though this is an example of a two-source SFG interference system (the resonant response predominantly from the air–polymer interface, and the nonresonant response from the Si), it illustrates how the phase can vary considerably as a result of interference.

2.3.4 Considerations for data collection

As the SFG signal is often weak, there is considerable interest in maximizing the signal-to-noise ratio by choosing an optimal set of incident visible and infrared beam angles. Although the orientation of the probed chemical functional group has the major effect on the beam angles, this is not known prior to the measurement. However, the local field and unit polarization factors appearing in Eq. 2.12 are also dependent on the beam angles, and these are independent of $\chi^{(2)}$. Previous studies of two-phase systems have reported on the optimization of these parameters [81–84]. I now consider the effect of multiple

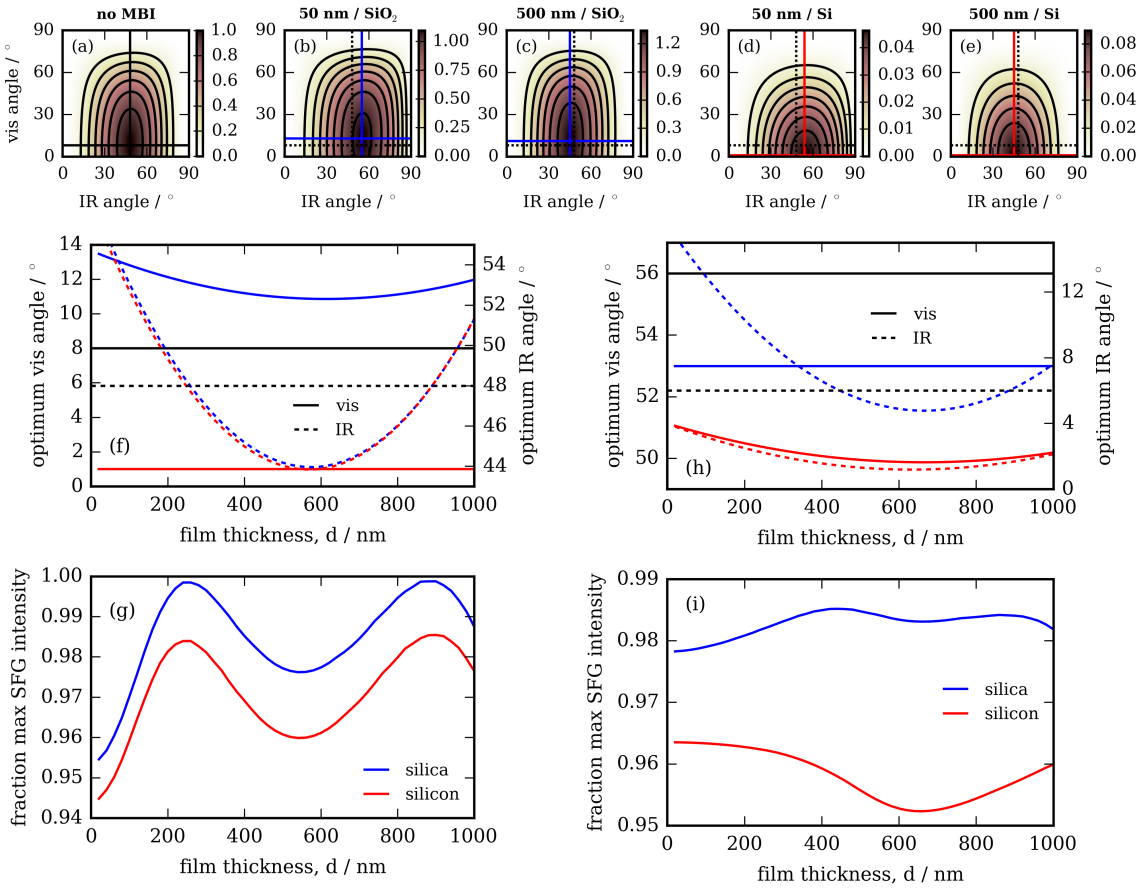

Figure 2.7: (a) Determination of optimal visible and infrared beam angles for ssp polarization at the air–polystyrene interface. The same calculation, but including multiple beam interference for the air–polystyrene–substrate system with (b) 50 nm polymer on silica, (c) 500 nm polymer on silica, (d) 50 nm polymer on silicon, (d) 500 nm polymer on silicon. (f) The optimum visible and IR angles as a function of film thickness; (g) the fraction of the maximum SFG intensity that would be measured if the beam angles were maintained at those optimum for the air–polystyrene surface. For sps beam polarizations, we plot (h) the optimal angles and (i) the fraction of the maximum achievable intensity corresponding to those angles.

beam interference on the optimal beam angles, and the consequence of not optimizing the geometry.

Fig. 2.7a plots the SFG intensity (color scale) as a function of the incident s-polarized visible and p-polarized infrared beam angles at the interface between air and an infinitely-thick polystyrene substrate. This was taken as the reference case, as it also applies to what would be used for a polymer thin film when ignoring multiple beam interference.

It was assumed that the area of each beam on the surface increases by a factor of $\cos\theta$ as the angle becomes more obtuse from normal incidence. This is the reason why the SFG intensity approaches zero as either of the beams approaches grazing incidence. The (black) cross-hairs indicate that the greatest s-polarized SFG intensity occurs at $\theta_{\mathrm{vis}} = 8^{\circ}$ and $\theta_{\mathrm{IR}} = 48^{\circ}$. The SFG intensity at these angles has been assigned a value of unity for reference. I then repeat this analysis for the case of multiple beam interference on the silica substrate with results for a 50 nm PS film in Fig. 2.7b and 500 nm film in Fig. 2.7c; the geometry corresponding to the highest SFG response is indicated by the blue crosshairs. If the substrate is silicon, the results are as shown in Fig 2.7d (50 nm PS) and Fig. 2.7e (500 nm PS) with red crosshairs. In all cases of multiple beam interference (b–e), results of the two-phase system (a) are included with dashed crosshairs for comparison. While these 50 and 500 nm thick cases serve as examples, the ssp results are summarized for all thicknesses up to 1 μm in Fig. 2.7f. Variation in the optimal visible angle is shown in solid lines, and infrared in dashed lines; low index substrate is blue, high index substrate in red. Even though there is not much variation in the ideal geometry, from a practical perspective the figure of merit is how much the SFG intensity would be compromised by not tailoring the experimental geometry according to the film thickness. Fig. 2.7g displays this quantitatively, plotting the fraction of the maximum ssp signal that would be obtained if the beams were fixed at their angles as calculated from a two-phase (air–polymer) system. The corresponding angles and efficiency in the case of sps polarization are shown in Figs. 2.7h and i.

In all cases it can be seen that, although there is a substantial change in the deduced molecular orientation as a result of the thin film interference, there is no appreciable change in the optimal geometry that is required to carry out the measurements. This is a welcome result, as it means the experiments can be performed without knowing the film thickness in advance. This is critical in situations where measuring the film thickness would contaminate the surface, so it is desirable to characterize the films at the end of the

experiment.

2.4 Conclusions

The phenomenon of multiple-beam interference, and its ramifications on light reflected off a surface, can be harnessed as an optical analysis tool for surface characterization. This has been shown for the characterization of oxide film growth on CZT. However, the phenomenon also contributes in unwanted ways to spectroscopic techniques, which is investigated in the context of sum-frequency generation spectroscopy.

In cases where multiple sources of SFG contribute to the detected response, the interference between them as a function of their separation is at times evident in the appearance of the data. It has been illustrated that, in the case where all of the signal originates at a single interface, the effects of multiple beam interference may still be substantial. It was determined that the effects of the multiple beam interference and the resulting film thickness dependence of the local field factors are more pronounced with higher index substrate materials.

Chapter 3

Design and Calibration of a Broadband IR Stokes Polarimeter

Previously, the Hore group has utilized and reported a Mueller matrix ellipsometer in the mid-infrared, constructed with a polarization-state generator (PSG) and polarization-state analyzer (PSA), each of which contains one PEM [26]. Such an instrument can measure all 16 elements of the Mueller matrix, providing the optical characteristics of any material, but must perform measurements in multiple azimuthal configurations of the PEMs in order to characterize any depolarization. When using a polarimeter for an ellipsometric application, one can measure depolarization, without making any assumptions about the material, using a single configuration. Here I present a demonstration of a novel broadband FTIR-based mid-infrared polarimeter that operates between 2.5–11 μm.

3.1 Instrument design and theory

3.1.1 Definitions and Approach

The Stokes polarimeter described here is an instrument designed to measure each of the four Stokes elements (which comprise the Stokes vector) at each wavelength in the mid-infrared. The input Stokes vector to be measured is defined as:

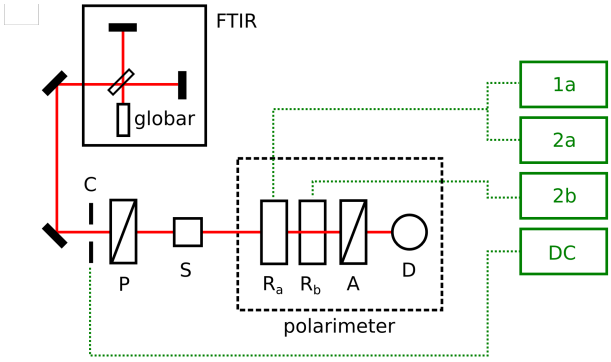

Figure 3.1: Stokes polarimeter based on two photoelastic modulators, indicating the polarizers ($\mathbf{P}$, or $\mathbf{A}$ in the case of the analyzer), sample position ($\mathbf{S}$), single-element integrating detector ($\mathbf{D}$). The first modulator is denoted $\mathbf{R}_a$ and the second one is $\mathbf{R}_b$. Optics are drawn in black, the beam path is shown in red, and electronics are shown in green.

$$\mathbf{s} = \begin{bmatrix} s_0 \\ s_1 \\ s_2 \\ s_3 \end{bmatrix}. \tag{3.1}$$

A Stokes polarimeter measures the polarization state of light by way of a detector which can only measure intensity. One approach is to build time-domain information into the intensity signal by way of polarization-modulating optical components with defined frequencies. In terms of optical elements, this Stokes polarimeter contains a photoelastic modulator PEM_1 with fast axis at 0 radians with retardation $\delta_1 = A_1 \cos(\omega_1 t) + \delta_1^0$, possessing amplitude A_1, static retardation δ_1^0 and frequency $\omega_1/2\pi$, a photoelastic modulator PEM_2 with fast axis at $\frac{\pi}{4}$ radians with retardation $\delta_2 = A_2 \cos(\omega_2 t) + \delta_2^0$, possessing amplitude A_2, static retardation δ_2^0 and frequency $\omega_2/2\pi$, and a linear polarizer A with its optical axis at $\pi/8$ rad. The instrumental configuration can be seen in Fig. 3.1.

To define the Mueller matrices of the optics, I first need to define the rotation matrix R.

$$R(\theta) = \begin{bmatrix} 1 & 0 & 0 & 0 \\ 0 & \cos 2\theta & \sin 2\theta & 0 \\ 0 & -\sin 2\theta & \cos 2\theta & 0 \\ 0 & 0 & 0 & 1 \end{bmatrix}. \tag{3.2}$$

A is a polarizer with azimuthal angle $\pi/8$, so the Mueller matrix is

$$A\left(\frac{\pi}{8}\right) = R\left(-\frac{\pi}{8}\right) \cdot \frac{1}{2} \begin{bmatrix} 1 & 1 & 0 & 0 \\ 1 & 1 & 0 & 0 \\ 0 & 0 & 0 & 0 \\ 0 & 0 & 0 & 0 \end{bmatrix} \cdot R\left(\frac{\pi}{8}\right). \tag{3.3}$$

PEM_1 and PEM_2 function as waveplates, with azimuthal angles 0 rad and $\pi/4$ rad, and retardances δ_1 and δ_2 respectively. The Mueller matrices are referred to as M_1 and M_2.

$$M_1\left(\delta_1, 0\right) = R\left(0\right) \begin{bmatrix} 1 & 0 & 0 & 0 \\ 0 & 1 & 0 & 0 \\ 0 & 0 & \cos\delta_1 & \sin\delta_1 \\ 0 & 0 & -\sin\delta_1 & \cos\delta_1 \end{bmatrix} R\left(0\right). \tag{3.4a}$$

$$M_2\left(\delta_2, \frac{\pi}{4}\right) = R\left(-\frac{\pi}{4}\right) \begin{bmatrix} 1 & 0 & 0 & 0 \\ 0 & 1 & 0 & 0 \\ 0 & 0 & \cos\delta_2 & \sin\delta_2 \\ 0 & 0 & -\sin\delta_2 & \cos\delta_2 \end{bmatrix} R\left(\frac{\pi}{4}\right). \tag{3.4b}$$

The Stokes vector of the light as it enters the detector is calculated by

$$\mathbf{s}' = A\left(\frac{\pi}{8}\right) \cdot M_2\left(\delta_2(t), \frac{\pi}{4}\right) \cdot M_1\left(\delta_1(t), 0\right) \cdot \mathbf{s} \tag{3.5}$$

Given that the signal produced at the detector is solely based on the intensity of the light (the first of the four Stokes elements), it is only this element, denoted as $\mathbf{s}'_0$, which needs to be considered.

$$\begin{aligned} \mathbf{s}'_0 = {} & \frac{1}{2}\mathbf{s}_0 + \frac{\sqrt{2}}{4}\cos\left(A_2\cos\left(\omega_2 t\right) + \delta_2^0\right)\mathbf{s}_1 \\ & + \frac{\sqrt{2}}{4}\Big(\cos\left(A_1\cos\left(\omega_1 t\right) + \delta_1^0\right) + \sin\left(A_2\cos\left(\omega_2 t\right) + \delta_2^0\right)\sin\left(A_1\cos\left(\omega_1 t\right) + \delta_1^0\right)\Big)\mathbf{s}_2 \\ & + \frac{\sqrt{2}}{4}\Big(\sin\left(A_1\cos\left(\omega_1 t\right) + \delta_1^0\right) - \sin\left(A_2\cos\left(\omega_2 t\right) + \delta_2^0\right)\cos\left(A_1\cos\left(\omega_1 t\right) + \delta_1^0\right)\Big)\mathbf{s}_3 \end{aligned} \tag{3.6}$$

The value of each Stokes element plays a role in the expression for $\mathbf{s}'_0$, and the objective is thus to isolate each Stokes element in separate equations. It is well-known with this methodology that each element can be isolated through demodulation of the signal at four different frequencies [85]. For our instrument, this is done using a lock-in amplifier, which will provide the signal demodulated at I_{DC}, $I_{2\omega_2}$, $I_{2\omega_1}$ and I_{ω_1}.

Fourier analysis can be used to determine how each Stokes element contributes to each of these four intensity values at each wavelength. From there, I will rearrange this relationship to elucidate of how each of these four intensity values contributes to each Stokes element at each wavelength. This method assumes that the amplitude and static retardation are known values at each wavelength for both PEMs.

It is also important to note that the optical path for the instrument contains a chopper, and thus what I denote as the I_{DC} signal is not truly a DC signal. It is unwieldly to attempt to describe a square wave in the derivation, so instead, I pretend in this mathematical derivation that the chopper does not exist. In practice, I_{DC} demodulates at the frequency of the chopper. A lock-in amplifier measures a square wave oscillating between a given amplitude and zero as having a $2/\pi$ intensity at that frequency. The result of this is that the measured I_{DC} signal from the lock-in must be divided by $2/\pi$. In addition, the chopper blocks the beam half of the time while the other lock-in amplifiers are measuring, which imparts a factor of one-half on the measurements of those frequency components. Thus the other intensities all must be multiplied by a factor of 2, in order to match with the mathematical derivation. The derivation to follow can be thought of with a single wavelength in mind, as the data can, in theory, be analyzed one wavelength at a time. The amplitude and static retardation values vary from wavelength to wavelength in a broadband setup.

3.1.2 Fourier Analysis

Fourier analysis is based on the principle that any original periodic function $f(x)$ with period $2L$ can be expressed as a series of cosine and sine terms.

$$f(x) = a_0 + \sum_{n=1}^{\infty} a_n \cos\left(\frac{\pi}{L} nx\right) + b_n \sin\left(\frac{\pi}{L} nx\right) \tag{3.7}$$

If $f(x)$ is initially written in a different form, then it convert can be converted to the above series form by calculating the coefficients a_i and b_i. In this case, I measure four of those coefficients directly with lock-in amplifiers, and in order to interpret those numbers, I need

to generate expressions for what those coefficients mean. Deriving expressions for the coefficients is relatively straightforward, and is based on the following two equations, with $f(x)$ as described above.

$$\int_{-L}^{L} f(x)dx = 2La_0 \tag{3.8}$$

$$\int_{-L}^{L} f(x)\cos\left(\frac{\pi}{L}ix\right)dx = La_i \tag{3.9}$$

It is important to note that the chosen bounds of integration are $-L$ and L, which defines exactly one period for the term with $n = 1$. For the rest of this derivation, L will be changed to π, and ω_1 and ω_2, which are the exact frequencies of the PEMs in rad/s, are treated as though they are integers. Much of the mathematical derivation to follow will be peformed under the assumption that these two frequencies be integers; however, making this assumption does not restrict generality and practically speaking, there is no need for these frequencies to be integers. In employing Fourier analysis, $f(x)$ is assumed to be a periodic function with a defined period. This period will, by necessity, represent an integer number of periods of all contributing frequency components, and this then implies that there is always a rational relationship between any two frequency components such that $n\omega_i = m\omega_j$ for some integers n and m. The overall period of $f(x)$ will be determined by how large a number L must be in order for all component frequencies to be integer multiples of $1/L$, and the math to follow is equally applicable to any system where this is the case, whether $L = \pi$ or not.

The possibility of having an irrational relationship between the two frequencies of the PEMs can be ignored. If this were the case, the waveform at the detector would not be periodic, as there would be no defined period. Thus, Fourier analysis would have to be approximated by rounding these frequencies to force a rational relationship. This approximation is not expected to have a significant impact on the results.

3.1.3 Expressing I_{dc}

Demodulation of the signal to produce I_{dc} can be mathematically described as

$$
\begin{aligned}
I_{dc} &= \frac{\int_{-\pi}^{\pi} \mathbf{s}_0' dt}{2\pi} \\
&= \int_{-\pi}^{\pi} \Bigg[\frac{1}{4\pi}\mathbf{s}_0 + \frac{\sqrt{2}}{8\pi} \cos\left(A_2 \cos\left(\omega_2 t\right) + \delta_2^0\right)\mathbf{s}_1 \\
&+ \frac{\sqrt{2}}{8\pi}\Bigg(\cos\left(A_1 \cos\left(\omega_1 t\right) + \delta_1^0\right) \\
&+ \sin\left(A_2 \cos\left(\omega_2 t\right) + \delta_2^0\right) \sin\left(A_1 \cos\left(\omega_1 t\right) + \delta_1^0\right)\Bigg)\mathbf{s}_2 \\
&- \frac{\sqrt{2}}{8\pi}\Bigg(\sin\left(A_1 \cos\left(\omega_1 t\right) + \delta_1^0\right) \\
&- \sin\left(A_2 \cos\left(\omega_2 t\right) + \delta_2^0\right) \cos\left(A_1 \cos\left(\omega_1 t\right) + \delta_1^0\right)\Bigg)\mathbf{s}_3 \Bigg] dt \\
&= \mathbf{s}_0 \int_{-\pi}^{\pi} \frac{1}{4\pi} dt + \frac{\sqrt{2}}{8\pi}\Bigg[\mathbf{s}_1 \int_{-\pi}^{\pi} \cos\left(A_2 \cos\left(\omega_2 t\right) + \delta_2^0\right) dt \\
&+ \mathbf{s}_2 \Bigg(\int_{-\pi}^{\pi} \cos\left(A_1 \cos\left(\omega_1 t\right) + \delta_1^0\right) dt \\
&+ \int_{-\pi}^{\pi} \sin\left(A_2 \cos\left(\omega_2 t\right) + \delta_2^0\right) \sin\left(A_1 \cos\left(\omega_1 t\right) + \delta_1^0\right) dt \Bigg) \\
&+ \mathbf{s}_3 \Bigg(\int_{-\pi}^{\pi} \sin\left(A_1 \cos\left(\omega_1 t\right) + \delta_1^0\right) dt \\
&- \int_{-\pi}^{\pi} \sin\left(A_2 \cos\left(\omega_2 t\right) + \delta_2^0\right) \cos\left(A_1 \cos\left(\omega_1 t\right) + \delta_1^0\right) dt \Bigg) \Bigg]
\end{aligned}
\tag{3.10}
$$

At this point, it was found that the computer software being used, and indeed any mathematical software I tried, was incapable of simplifying integrals analytically. It is possible to simplify these integrals to find an analytical solution, using some identities. The identities used are discussed in Appendix A.

The expression for I_{dc} from Eq. 3.10 becomes easier to solve if broken down into the contributions from each Stokes element individually. The solutions of the integral terms shown below in Eq. 3.12 make use of Eq. A.5, and those in Eqs. 3.13 and 3.14 make use of

Eq. A.7

$$\mathbf{s}_0 \int_{-\pi}^{\pi} \frac{1}{4\pi} dt$$

$$= \frac{1}{2} \cdot \mathbf{s}_0 \tag{3.11}$$

$$\mathbf{s}_1 \cdot \frac{\sqrt{2}}{8\pi} \int_{-\pi}^{\pi} \cos\left(A_2 \cos(\omega_2 t) + \delta_2^0\right) dt$$
$$= \mathbf{s}_1 \cdot \frac{\sqrt{2}}{8\pi} \int_{-\pi}^{\pi} \left[\cos(A_2 \cos(\omega_2 t)) \cos\left(\delta_2^0\right) - \sin(A_2 \cos(\omega_2 t)) \sin\left(\delta_2^0\right) \right] dt$$
$$= \mathbf{s}_1 \cdot \frac{\sqrt{2}}{8\pi} \left[\cos\left(\delta_2^0\right) \underbrace{\int_{-\pi}^{\pi} \cos(A_2 \cos(\omega_2 t)) dt}_{2\pi J_0(A_2)} - \sin\left(\delta_2^0\right) \underbrace{\int_{-\pi}^{\pi} \sin(A_2 \cos(\omega_2 t)) dt}_{0} \right]$$

$$= \frac{1}{2\sqrt{2}} \cos\left(\delta_2^0\right) J_0(A_2) \cdot \mathbf{s}_1 \tag{3.12}$$

$$\mathbf{s}_2 \cdot \frac{\sqrt{2}}{8\pi} \left[\underbrace{\int_{-\pi}^{\pi} \cos\left(A_1 \cos(\omega_1 t) + \delta_1^0\right) dt}_{2\pi \cos(\delta_1^0) J_0(A_1)} \right.$$
$$\left. + \int_{-\pi}^{\pi} \sin\left(A_2 \cos(\omega_2 t) + \delta_2^0\right) \sin\left(A_1 \cos(\omega_1 t) + \delta_1^0\right) dt \right]$$
$$= \mathbf{s}_2 \cdot \frac{\sqrt{2}}{8\pi} \left[2\pi \cos\left(\delta_1^0\right) J_0(A_1) \right.$$
$$+ \int_{-\pi}^{\pi} \left(\cos\left(\delta_2^0\right) \sin(A_2 \cos(\omega_2 t)) + \sin\left(\delta_2^0\right) \cos(A_2 \cos(\omega_2 t)) \right)$$
$$\left. \times \left(\cos\left(\delta_1^0\right) \sin(A_1 \cos(\omega_1 t)) + \sin\left(\delta_1^0\right) \cos(A_1 \cos(\omega_1 t)) \right) dt \right]$$

$$
\begin{aligned}
&= \mathbf{s}_2 \cdot \frac{\sqrt{2}}{8\pi} \Big[2\pi \cos\left(\delta_1^0\right) J_0(A_1) \\
&+ \sin\left(\delta_1^0\right) \sin\left(\delta_2^0\right) \cancelto{2\pi J_0(A_1) J_0(A_2)}{\int_{-\pi}^{\pi} \cos\left(A_1 \cos\left(\omega_1 t\right)\right) \cos\left(A_2 \cos\left(\omega_2 t\right)\right) dt} \\
&\quad + \sin\left(\delta_1^0\right) \cos\left(\delta_2^0\right) \cancelto{0}{\int_{-\pi}^{\pi} \cos\left(A_1 \cos\left(\omega_1 t\right)\right) \sin\left(A_2 \cos\left(\omega_2 t\right)\right) dt} \\
&\quad + \cos\left(\delta_1^0\right) \sin\left(\delta_2^0\right) \cancelto{0}{\int_{-\pi}^{\pi} \sin\left(A_1 \cos\left(\omega_1 t\right)\right) \cos\left(A_2 \cos\left(\omega_2 t\right)\right) dt} \\
&\quad + \cos\left(\delta_1^0\right) \cos\left(\delta_2^0\right) \cancelto{0}{\int_{-\pi}^{\pi} \sin\left(A_1 \cos\left(\omega_1 t\right)\right) \sin\left(A_2 \cos\left(\omega_2 t\right)\right) dt} \Big] \\
&= \frac{1}{2\sqrt{2}} \Big(\cos\left(\delta_1^0\right) J_0(A_1) + \sin\left(\delta_1^0\right) \sin\left(\delta_2^0\right) J_0(A_1) J_0(A_2) \Big) \cdot \mathbf{s}_2
\end{aligned}
\tag{3.13}
$$

$$
\begin{aligned}
&\mathbf{s}_3 \cdot \frac{\sqrt{2}}{8\pi} \Bigg[\cancelto{2\pi \sin\left(\delta_1^0\right) J_0(A_1)}{\int_{-\pi}^{\pi} \sin\left(A_1 \cos\left(\omega_1 t\right) + \delta_1^0\right) dt} \\
&- \int_{-\pi}^{\pi} \sin\left(A_2 \cos\left(\omega_2 t\right) + \delta_2^0\right) \cos\left(A_1 \cos\left(\omega_1 t\right) + \delta_1^0\right) dt \Bigg] \\
&= \mathbf{s}_3 \cdot \frac{\sqrt{2}}{8\pi} \Big[2\pi \sin\left(\delta_1^0\right) J_0(A_1) \\
&- \int_{-\pi}^{\pi} \Bigg(\cos\left(\delta_2^0\right) \sin\left(A_2 \cos\left(\omega_2 t\right)\right) + \sin\left(\delta_2^0\right) \cos\left(A_2 \cos\left(\omega_2 t\right)\right) \Bigg) \\
&\times \Bigg(\cos\left(\delta_1^0\right) \cos\left(A_1 \cos\left(\omega_1 t\right)\right) - \sin\left(\delta_1^0\right) \sin\left(A_1 \cos\left(\omega_1 t\right)\right) \Bigg) dt \Big]
\end{aligned}
$$

$$
\begin{aligned}
&= \mathbf{s}_3 \cdot \frac{\sqrt{2}}{8\pi}\Bigg[2\pi \sin\left(\delta_1^0\right) J_0(A_1) \\
&\quad - \cos\left(\delta_1^0\right) \sin\left(\delta_2^0\right) \int_{-\pi}^{\pi} \cos\left(A_1 \cos\left(\omega_1 t\right)\right) \cos\left(A_2 \cos\left(\omega_2 t\right)\right) dt \quad \rightarrow 2\pi J_0(A_1) J_0(A_2) \\
&\quad - \cos\left(\delta_1^0\right) \cos\left(\delta_2^0\right) \int_{-\pi}^{\pi} \cos\left(A_1 \cos\left(\omega_1 t\right)\right) \sin\left(A_2 \cos\left(\omega_2 t\right)\right) dt \quad \rightarrow 0 \\
&\quad + \sin\left(\delta_1^0\right) \sin\left(\delta_2^0\right) \int_{-\pi}^{\pi} \sin\left(A_1 \cos\left(\omega_1 t\right)\right) \cos\left(A_2 \cos\left(\omega_2 t\right)\right) dt \quad \rightarrow 0 \\
&\quad + \sin\left(\delta_1^0\right) \cos\left(\delta_2^0\right) \int_{-\pi}^{\pi} \sin\left(A_1 \cos\left(\omega_1 t\right)\right) \sin\left(A_2 \cos\left(\omega_2 t\right)\right) dt \quad \rightarrow 0 \Bigg] \\
&= \frac{1}{2\sqrt{2}} \left(\sin\left(\delta_1^0\right) J_0(A_1) - \cos\left(\delta_1^0\right) \sin\left(\delta_2^0\right) J_0(A_1) J_0(A_2)\right) \cdot \mathbf{s}_3
\end{aligned} \tag{3.14}
$$

The expression for I_{dc} in terms of the Stokes elements can now be written as

$$
\begin{aligned}
I_{dc} = &\frac{1}{2} \cdot \mathbf{s}_0 + \frac{1}{2\sqrt{2}} \Bigg[\cos\left(\delta_2^0\right) J_0(A_2) \cdot \mathbf{s}_1 \\
&+ \left(\sin\left(\delta_1^0\right) \sin\left(\delta_2^0\right) J_0(A_1) J_0(A_2) + \cos\left(\delta_1^0\right) J_0(A_1)\right) \cdot \mathbf{s}_2 \\
&- \left(\cos\left(\delta_1^0\right) \sin\left(\delta_2^0\right) J_0(A_1) J_0(A_2) - \sin\left(\delta_1^0\right) J_0(A_1)\right) \cdot \mathbf{s}_3 \Bigg]
\end{aligned} \tag{3.15}
$$

3.1.4 Expressing I_{ω_1}

Demodulation of the signal at the fundamental frequency of the first PEM is accomplished by integrating the signal expression multiplied by $\cos \omega_1$ over the same range.

$$
I_{\omega_1} = \frac{\int_{-\pi}^{\pi} \mathbf{s}_0' \cdot \cos\left(\omega_1 t\right) dt}{\pi}
$$

$$
\begin{aligned}
&= \int_{-\pi}^{\pi} \Bigg[\frac{1}{2\pi}\mathbf{s}_0 + \frac{\sqrt{2}}{4\pi} \cos\left(A_2 \cos\left(\omega_2 t\right) + \delta_2^0\right)\mathbf{s}_1 \\
&+ \frac{\sqrt{2}}{4\pi}\Bigg(\cos\left(A_1 \cos\left(\omega_1 t\right) + \delta_1^0\right) \\
&+ \sin\left(A_2 \cos\left(\omega_2 t\right) + \delta_2^0\right) \sin\left(A_1 \cos\left(\omega_1 t\right) + \delta_1^0\right)\Bigg)\mathbf{s}_2 \\
&+ \frac{\sqrt{2}}{4\pi}\Bigg(\sin\left(A_1 \cos\left(\omega_1 t\right) + \delta_1^0\right) \\
&- \sin\left(A_2 \cos\left(\omega_2 t\right) + \delta_2^0\right) \cos\left(A_1 \cos\left(\omega_1 t\right) + \delta_1^0\right)\Bigg)\mathbf{s}_3 \Bigg] \cdot \cos\left(\omega_1 t\right) dt
\end{aligned}
$$

$$
\begin{aligned}
&= \mathbf{s}_0 \int_{-\pi}^{\pi} \frac{\cos\left(\omega_1 t\right)}{2\pi} dt + \frac{\sqrt{2}}{4\pi}\Bigg[\mathbf{s}_1 \int_{-\pi}^{\pi} \cos\left(A_2 \cos\left(\omega_2 t\right) + \delta_2^0\right) \cos\left(\omega_1 t\right) dt \\
&+ \mathbf{s}_2 \Bigg(\int_{-\pi}^{\pi} \cos\left(A_1 \cos\left(\omega_1 t\right) + \delta_1^0\right) \cos\left(\omega_1 t\right) dt \\
&+ \int_{-\pi}^{\pi} \sin\left(A_2 \cos\left(\omega_2 t\right) + \delta_2^0\right) \sin\left(A_1 \cos\left(\omega_1 t\right) + \delta_1^0\right) \cos\left(\omega_1 t\right) dt \Bigg) \\
&+ \mathbf{s}_3 \Bigg(\int_{-\pi}^{\pi} \sin\left(A_1 \cos\left(\omega_1 t\right) + \delta_1^0\right) \cos\left(\omega_1 t\right) dt \\
&- \int_{-\pi}^{\pi} \sin\left(A_2 \cos\left(\omega_2 t\right) + \delta_2^0\right) \cos\left(A_1 \cos\left(\omega_1 t\right) + \delta_1^0\right) \cos\left(\omega_1 t\right) dt \Bigg) \Bigg]
\end{aligned} \tag{3.16}
$$

Once again, I will break down the expression for I_{ω_1} into the terms for each Stokes element. The integrals encountered upon expansion can be solved using Eqs. A.11–A.13 and A.15–A.18.

$$
\begin{aligned}
&\mathbf{s}_0 \int_{-\pi}^{\pi} \frac{\cos(\omega_1 t)}{2\pi} dt \\
&= 0
\end{aligned} \tag{3.17}
$$

$$
\begin{aligned}
&\mathbf{s}_1 \cdot \frac{\sqrt{2}}{4\pi} \int_{-\pi}^{\pi} \cos\left(A_2 \cos\left(\omega_2 t\right) + \delta_2^0\right) \cos(\omega_1 t) dt \\
&= \mathbf{s}_1 \cdot \frac{\sqrt{2}}{4\pi} \int_{-\pi}^{\pi} \Bigg[\cos\left(A_2 \cos\left(\omega_2 t\right)\right) \cos\left(\delta_2^0\right) \cos(\omega_1 t) \\
&- \sin\left(A_2 \cos\left(\omega_2 t\right)\right) \sin\left(\delta_2^0\right) \cos(\omega_1 t) \Bigg] dt
\end{aligned}
$$

$$= \mathbf{s}_1 \cdot \frac{\sqrt{2}}{4\pi}\Bigg[\cos\left(\delta_2^0\right)\underbrace{\int_{-\pi}^{\pi}\cos\left(A_2\cos\left(\omega_2 t\right)\right)\cos(\omega_1 t)dt}_{\to 0}$$

$$-\sin\left(\delta_2^0\right)\underbrace{\int_{-\pi}^{\pi}\sin\left(A_2\cos\left(\omega_2 t\right)\right)\cos(\omega_1 t)dt}_{\to 0}\Bigg]$$

$$= 0 \tag{3.18}$$

$$\mathbf{s}_2 \cdot \frac{\sqrt{2}}{4\pi}\Bigg[\int_{-\pi}^{\pi}\cos\left(A_1\cos\left(\omega_1 t\right)+\delta_1^0\right)\cos(\omega_1 t)dt$$

$$+\int_{-\pi}^{\pi}\sin\left(A_2\cos\left(\omega_2 t\right)+\delta_2^0\right)\sin\left(A_1\cos\left(\omega_1 t\right)+\delta_1^0\right)\cos(\omega_1 t)dt\Bigg]$$

$$= \mathbf{s}_2 \cdot \frac{\sqrt{2}}{4\pi}\Bigg(\int_{-\pi}^{\pi}\Bigg[\cos\left(A_1\cos\left(\omega_1 t\right)\right)\cos\left(\delta_1^0\right)\cos(\omega_1 t)$$

$$-\sin\left(A_1\cos\left(\omega_1 t\right)\right)\sin\left(\delta_1^0\right)\cos(\omega_1 t)\Bigg]dt$$

$$+\int_{-\pi}^{\pi}\Bigg[\cos\left(\delta_2^0\right)\sin\left(A_2\cos\left(\omega_2 t\right)\right)+\sin\left(\delta_2^0\right)\cos\left(A_2\cos\left(\omega_2 t\right)\right)\Bigg]$$

$$\times\Bigg[\cos\left(\delta_1^0\right)\sin\left(A_1\cos\left(\omega_1 t\right)\right)+\sin\left(\delta_1^0\right)\cos\left(A_1\cos\left(\omega_1 t\right)\right)\Bigg]\cos(\omega_1 t)dt\Bigg)$$

$$
\begin{aligned}
&= \mathbf{s}_2 \cdot \frac{\sqrt{2}}{4\pi}\Bigg(\cos\left(\delta_1^0\right) \underbrace{\int_{-\pi}^{\pi} \cos\left(A_1 \cos\left(\omega_1 t\right)\right) \cos(\omega_1 t) dt}_{\to 0} \\
&- \sin\left(\delta_1^0\right) \underbrace{\int_{-\pi}^{\pi} \sin\left(A_1 \cos\left(\omega_1 t\right)\right) \cos(\omega_1 t) dt}_{\to 2\pi J_1(A_1)} \\
&+ \sin\left(\delta_1^0\right) \sin\left(\delta_2^0\right) \underbrace{\int_{-\pi}^{\pi} \cos\left(A_1 \cos\left(\omega_1 t\right)\right) \cos\left(A_2 \cos\left(\omega_2 t\right)\right) \cos(\omega_1 t) dt}_{\to 0} \\
&+ \cos\left(\delta_1^0\right) \sin\left(\delta_2^0\right) \underbrace{\int_{-\pi}^{\pi} \sin\left(A_1 \cos\left(\omega_1 t\right)\right) \cos\left(A_2 \cos\left(\omega_2 t\right)\right) \cos(\omega_1 t) dt}_{\to 2\pi J_1(A_1) J_0(A_2)} \\
&+ \sin\left(\delta_1^0\right) \cos\left(\delta_2^0\right) \underbrace{\int_{-\pi}^{\pi} \cos\left(A_1 \cos\left(\omega_1 t\right)\right) \sin\left(A_2 \cos\left(\omega_2 t\right)\right) \cos(\omega_1 t) dt}_{\to 0} \\
&+ \cos\left(\delta_1^0\right) \cos\left(\delta_2^0\right) \underbrace{\int_{-\pi}^{\pi} \sin\left(A_1 \cos\left(\omega_1 t\right)\right) \sin\left(A_2 \cos\left(\omega_2 t\right)\right) \cos(\omega_1 t) dt}_{\to 0} \Bigg) \\
&= \mathbf{s}_2 \cdot \frac{1}{\sqrt{2}}\Big(\cos(\delta_1^0) \sin(\delta_2^0) J_1(A_1) J_0(A_2) - \sin(\delta_1^0) J_1(A_1) \Big)
\end{aligned} \tag{3.19}
$$

$$
\begin{aligned}
&\mathbf{s}_3 \cdot \frac{\sqrt{2}}{4\pi}\Bigg[\int_{-\pi}^{\pi} \sin\left(A_1 \cos\left(\omega_1 t\right) + \delta_1^0\right) \cos(\omega_1 t) dt \\
&- \int_{-\pi}^{\pi} \sin\left(A_2 \cos\left(\omega_2 t\right) + \delta_2^0\right) \cos\left(A_1 \cos\left(\omega_1 t\right) + \delta_1^0\right) \cos(\omega_1 t) dt \Bigg] \\
&= \mathbf{s}_3 \cdot \frac{-\sqrt{2}}{4\pi}\Bigg(\int_{-\pi}^{\pi} \Big[\cos\left(\delta_2^0\right) \sin\left(A_2 \cos\left(\omega_2 t\right)\right) + \sin\left(\delta_2^0\right) \cos\left(A_2 \cos\left(\omega_2 t\right)\right) \Big] \\
&\times \Big[\cos\left(\delta_1^0\right) \cos\left(A_1 \cos\left(\omega_1 t\right)\right) - \sin\left(\delta_1^0\right) \sin\left(A_1 \cos\left(\omega_1 t\right)\right) \Big] \cdot \cos(\omega_1 t) dt \\
&- \int_{-\pi}^{\pi} \Big[\sin\left(A_1 \cos\left(\omega_1 t\right)\right) \cos\left(\delta_1^0\right) \cos(\omega_1 t) \\
&+ \cos\left(A_1 \cos\left(\omega_1 t\right)\right) \sin\left(\delta_1^0\right) \cos(\omega_1 t) \Big] dt \Bigg)
\end{aligned}
$$

$$
\begin{aligned}
&= \mathbf{s}_3 \cdot \frac{-\sqrt{2}}{4\pi}\Bigg(\cos\left(\delta_1^0\right)\cos\left(\delta_2^0\right)\int_{-\pi}^{\pi} \cos\left(A_1\cos\left(\omega_1 t\right)\right)\sin\left(A_2\cos\left(\omega_2 t\right)\right)\cos(\omega_1 t)dt \quad \to 0 \\
&- \sin\left(\delta_1^0\right)\cos\left(\delta_2^0\right)\int_{-\pi}^{\pi} \sin\left(A_1\cos\left(\omega_1 t\right)\right)\sin\left(A_2\cos\left(\omega_2 t\right)\right)\cos(\omega_1 t)dt \quad \to 0 \\
&+ \cos\left(\delta_1^0\right)\sin\left(\delta_2^0\right)\int_{-\pi}^{\pi} \cos\left(A_1\cos\left(\omega_1 t\right)\right)\cos\left(A_2\cos\left(\omega_2 t\right)\right)\cos(\omega_1 t)dt \quad \to 0 \\
&- \sin\left(\delta_1^0\right)\sin\left(\delta_2^0\right)\int_{-\pi}^{\pi} \sin\left(A_1\cos\left(\omega_1 t\right)\right)\cos\left(A_2\cos\left(\omega_2 t\right)\right)\cos(\omega_1 t)dt \quad \to 2\pi J_1(A_1)J_0(A_2) \\
&- \cos\left(\delta_1^0\right)\int_{-\pi}^{\pi} \sin\left(A_1\cos\left(\omega_1 t\right)\right)\cos(\omega_1 t)dt \quad \to 2\pi J_1(A_1) \\
&- \sin\left(\delta_1^0\right)\int_{-\pi}^{\pi} \cos\left(A_1\cos\left(\omega_1 t\right)\right)\cos(\omega_1 t)dt\Bigg) \quad \to 0 \\
&= \mathbf{s}_3 \cdot \frac{1}{\sqrt{2}}\Bigg(\sin\left(\delta_1^0\right)\sin\left(\delta_2^0\right)J_1(A_1)J_0(A_2) + \cos\left(\delta_1^0\right)J_1(A_1)\Bigg)
\end{aligned}
\tag{3.20}
$$

I can now write the expression for I_{ω_1} in terms of the Stokes elements.

$$
\begin{aligned}
I_{\omega_1} =& \frac{1}{\sqrt{2}}\Bigg[\Big(\cos(\delta_1^0)\sin(\delta_2^0)J_1(A_1)J_0(A_2) - \sin(\delta_1^0)J_1(A_1)\Big)\cdot \mathbf{s}_2 \\
&+ \Big(\sin\left(\delta_1^0\right)\sin\left(\delta_2^0\right)J_1(A_1)J_0(A_2) + \cos\left(\delta_1^0\right)J_1(A_1)\Big)\cdot \mathbf{s}_3\Bigg]
\end{aligned}
\tag{3.21}
$$

3.1.5 Expressing $I_{2\omega_1}$

Similarly to the previous section, the demodulation of the signal at $I_{2\omega_1}$ is accomplished by integrating the function multiplied by $\cos 2\omega_1$ from $-\pi$ to π.

$$I_{2\omega_1} = \frac{\int_{-\pi}^{\pi} \mathbf{s}_0' \cdot \cos(2\omega_1 t)dt}{\pi}$$

$$\begin{aligned}
&= \int_{-\pi}^{\pi} \Bigg[\frac{1}{2\pi}\mathbf{s}_0 + \frac{\sqrt{2}}{4\pi}\cos\big(A_2\cos(\omega_2 t) + \delta_2^0\big)\mathbf{s}_1 \\
&+ \frac{\sqrt{2}}{4\pi}\Bigg(\cos\big(A_1\cos(\omega_1 t) + \delta_1^0\big) \\
&+ \sin\big(A_2\cos(\omega_2 t) + \delta_2^0\big)\sin\big(A_1\cos(\omega_1 t) + \delta_1^0\big)\Bigg)\mathbf{s}_2 \\
&+ \frac{\sqrt{2}}{4\pi}\Bigg(\sin\big(A_1\cos(\omega_1 t) + \delta_1^0\big) \\
&- \sin\big(A_2\cos(\omega_2 t) + \delta_2^0\big)\cos\big(A_1\cos(\omega_1 t) + \delta_1^0\big)\Bigg)\mathbf{s}_3\Bigg] \cdot \cos(2\omega_1 t)dt
\end{aligned}$$

$$\begin{aligned}
&= \mathbf{s}_0 \int_{-\pi}^{\pi} \frac{\cos(2\omega_1 t)}{2\pi}dt + \frac{\sqrt{2}}{4\pi}\Bigg[\mathbf{s}_1 \int_{-\pi}^{\pi} \cos\big(A_2\cos(\omega_2 t) + \delta_2^0\big)\cos(2\omega_1 t)dt \\
&+ \mathbf{s}_2\Bigg(\int_{-\pi}^{\pi} \cos\big(A_1\cos(\omega_1 t) + \delta_1^0\big)\cos(2\omega_1 t)dt \\
&+ \int_{-\pi}^{\pi} \sin\big(A_2\cos(\omega_2 t) + \delta_2^0\big)\sin\big(A_1\cos(\omega_1 t) + \delta_1^0\big)\cos(2\omega_1 t)dt\Bigg) \\
&+ \mathbf{s}_3\Bigg(\int_{-\pi}^{\pi} \sin\big(A_1\cos(\omega_1 t) + \delta_1^0\big)\cos(2\omega_1 t)dt \\
&- \int_{-\pi}^{\pi} \sin\big(A_2\cos(\omega_2 t) + \delta_2^0\big)\cos\big(A_1\cos(\omega_1 t) + \delta_1^0\big)\cos(2\omega_1 t)dt\Bigg)\Bigg]
\end{aligned} \tag{3.22}$$

As previously, I break down the expression for $I_{2\omega_1}$ into the terms for each Stokes element. The integrals can be solved making use of Eqs. A.19–A.25.

$$\mathbf{s}_0 \int_{-\pi}^{\pi} \frac{\cos(2\omega_1 t)}{2\pi}dt$$

$$= 0 \tag{3.23}$$

$$
\begin{aligned}
&\mathbf{s}_1 \cdot \frac{\sqrt{2}}{4\pi} \int_{-\pi}^{\pi} \cos\left(A_2 \cos\left(\omega_2 t\right) + \delta_2^0\right) \cos(2\omega_1 t) dt \\
&= \mathbf{s}_1 \cdot \frac{\sqrt{2}}{4\pi} \int_{-\pi}^{\pi} \Bigg[\cos\left(A_2 \cos\left(\omega_2 t\right)\right) \cos\left(\delta_2^0\right) \cos(2\omega_1 t) \\
&- \sin\left(A_2 \cos\left(\omega_2 t\right)\right) \sin\left(\delta_2^0\right) \cos(2\omega_1 t) \Bigg] dt \\
&= \mathbf{s}_1 \cdot \frac{\sqrt{2}}{4\pi} \Bigg[\cos\left(\delta_2^0\right) \underbrace{\int_{-\pi}^{\pi} \cos\left(A_2 \cos\left(\omega_2 t\right)\right) \cos(2\omega_1 t) dt}_{\to 0} \\
&- \sin\left(\delta_2^0\right) \underbrace{\int_{-\pi}^{\pi} \sin\left(A_2 \cos\left(\omega_2 t\right)\right) \cos(2\omega_1 t) dt}_{\to 0} \Bigg] \\
&= 0
\end{aligned}
\tag{3.24}
$$

$$
\begin{aligned}
&\mathbf{s}_2 \cdot \frac{\sqrt{2}}{4\pi} \Bigg[\int_{-\pi}^{\pi} \cos\left(A_1 \cos\left(\omega_1 t\right) + \delta_1^0\right) \cos(2\omega_1 t) dt \\
&+ \int_{-\pi}^{\pi} \sin\left(A_2 \cos\left(\omega_2 t\right) + \delta_2^0\right) \sin\left(A_1 \cos\left(\omega_1 t\right) + \delta_1^0\right) \cos(2\omega_1 t) dt \Bigg] \\
&= \mathbf{s}_2 \cdot \frac{\sqrt{2}}{4\pi} \Bigg(\int_{-\pi}^{\pi} \Bigg[\cos\left(A_1 \cos\left(\omega_1 t\right)\right) \cos\left(\delta_1^0\right) \cos(2\omega_1 t) \\
&- \sin\left(A_1 \cos\left(\omega_1 t\right)\right) \sin\left(\delta_1^0\right) \cos(2\omega_1 t) \Bigg] dt \\
&+ \int_{-\pi}^{\pi} \Bigg[\cos\left(\delta_2^0\right) \sin\left(A_2 \cos\left(\omega_2 t\right)\right) + \sin\left(\delta_2^0\right) \cos\left(A_2 \cos\left(\omega_2 t\right)\right) \Bigg] \\
&\times \Bigg[\cos\left(\delta_1^0\right) \sin\left(A_1 \cos\left(\omega_1 t\right)\right) + \sin\left(\delta_1^0\right) \cos\left(A_1 \cos\left(\omega_1 t\right)\right) \Bigg] \cos(2\omega_1 t) dt \Bigg)
\end{aligned}
$$

$$
\begin{aligned}
&= \mathbf{s}_2 \cdot \frac{\sqrt{2}}{4\pi}\Bigg(\cos\left(\delta_1^0\right) \int_{-\pi}^{\pi} \cos\left(A_1 \cos\left(\omega_1 t\right)\right) \cos(2\omega_1 t) dt \quad \xrightarrow{-2\pi J_2(A_1)} \\
&- \sin\left(\delta_1^0\right) \int_{-\pi}^{\pi} \sin\left(A_1 \cos\left(\omega_1 t\right)\right) \cos(2\omega_1 t) dt \quad \xrightarrow{0} \\
&+ \sin\left(\delta_1^0\right) \sin\left(\delta_2^0\right) \int_{-\pi}^{\pi} \cos\left(A_1 \cos\left(\omega_1 t\right)\right) \cos\left(A_2 \cos\left(\omega_2 t\right)\right) \cos(2\omega_1 t) dt \quad \xrightarrow{-2\pi J_2(A_1) J_0(A_2)} \\
&+ \cos\left(\delta_1^0\right) \sin\left(\delta_2^0\right) \int_{-\pi}^{\pi} \sin\left(A_1 \cos\left(\omega_1 t\right)\right) \cos\left(A_2 \cos\left(\omega_2 t\right)\right) \cos(2\omega_1 t) dt \quad \xrightarrow{0} \\
&+ \sin\left(\delta_1^0\right) \cos\left(\delta_2^0\right) \int_{-\pi}^{\pi} \cos\left(A_1 \cos\left(\omega_1 t\right)\right) \sin\left(A_2 \cos\left(\omega_2 t\right)\right) \cos(2\omega_1 t) dt \quad \xrightarrow{0} \\
&+ \cos\left(\delta_1^0\right) \cos\left(\delta_2^0\right) \int_{-\pi}^{\pi} \sin\left(A_1 \cos\left(\omega_1 t\right)\right) \sin\left(A_2 \cos\left(\omega_2 t\right)\right) \cos(2\omega_1 t) dt \Bigg) \quad \xrightarrow{0} \\
&= \mathbf{s}_2 \cdot \frac{-1}{\sqrt{2}}\Bigg(\sin(\delta_1^0) \sin(\delta_2^0) J_2(A_1) J_0(A_2) + \cos(\delta_1^0) J_2(A_1) \Bigg)
\end{aligned} \tag{3.25}
$$

$$
\begin{aligned}
&\mathbf{s}_3 \cdot \frac{\sqrt{2}}{4\pi}\Bigg[\int_{-\pi}^{\pi} \sin\left(A_1 \cos\left(\omega_1 t\right) + \delta_1^0\right) \cos(2\omega_1 t) dt \\
&- \int_{-\pi}^{\pi} \sin\left(A_2 \cos\left(\omega_2 t\right) + \delta_2^0\right) \cos\left(A_1 \cos\left(\omega_1 t\right) + \delta_1^0\right) \cos(2\omega_1 t) dt \Bigg] \\
&= \mathbf{s}_3 \cdot \frac{-\sqrt{2}}{4\pi}\Bigg(\int_{-\pi}^{\pi} \Bigg[\cos\left(\delta_2^0\right) \sin\left(A_2 \cos\left(\omega_2 t\right)\right) + \sin\left(\delta_2^0\right) \cos\left(A_2 \cos\left(\omega_2 t\right)\right) \Bigg] \\
&\times \Bigg[\cos\left(\delta_1^0\right) \cos\left(A_1 \cos\left(\omega_1 t\right)\right) - \sin\left(\delta_1^0\right) \sin\left(A_1 \cos\left(\omega_1 t\right)\right) \Bigg] \cdot \cos(2\omega_1 t) dt \\
&- \int_{-\pi}^{\pi} \Bigg[\sin\left(A_1 \cos\left(\omega_1 t\right)\right) \cos\left(\delta_1^0\right) \cos(2\omega_1 t) \\
&+ \cos\left(A_1 \cos\left(\omega_1 t\right)\right) \sin\left(\delta_1^0\right) \cos(2\omega_1 t) \Bigg] dt \Bigg)
\end{aligned}
$$

$$
\begin{aligned}
&= \mathbf{s}_3 \cdot \frac{-\sqrt{2}}{4\pi}\Bigg(\cos\left(\delta_1^0\right)\cos\left(\delta_2^0\right)\int_{-\pi}^{\pi} \cos\left(A_1\cos\left(\omega_1 t\right)\right)\sin\left(A_2\cos\left(\omega_2 t\right)\right)\cos(2\omega_1 t)dt \quad \to 0 \\
&- \sin\left(\delta_1^0\right)\cos\left(\delta_2^0\right)\int_{-\pi}^{\pi} \sin\left(A_1\cos\left(\omega_1 t\right)\right)\sin\left(A_2\cos\left(\omega_2 t\right)\right)\cos(2\omega_1 t)dt \quad \to 0 \\
&+ \cos\left(\delta_1^0\right)\sin\left(\delta_2^0\right)\int_{-\pi}^{\pi} \cos\left(A_1\cos\left(\omega_1 t\right)\right)\cos\left(A_2\cos\left(\omega_2 t\right)\right)\cos(2\omega_1 t)dt \quad \to -2\pi J_2(A_1)J_0(A_2) \\
&- \sin\left(\delta_1^0\right)\sin\left(\delta_2^0\right)\int_{-\pi}^{\pi} \sin\left(A_1\cos\left(\omega_1 t\right)\right)\cos\left(A_2\cos\left(\omega_2 t\right)\right)\cos(2\omega_1 t)dt \quad \to 0 \\
&- \cos\left(\delta_1^0\right)\int_{-\pi}^{\pi} \sin\left(A_1\cos\left(\omega_1 t\right)\right)\cos(2\omega_1 t)dt \quad \to 0 \\
&- \sin\left(\delta_1^0\right)\int_{-\pi}^{\pi} \cos\left(A_1\cos\left(\omega_1 t\right)\right)\cos(2\omega_1 t)dt \Bigg) \quad \to -2\pi J_2(A_1) \\
&= \mathbf{s}_3 \cdot \frac{1}{\sqrt{2}}\Bigg(\cos\left(\delta_1^0\right)\sin\left(\delta_2^0\right)J_2(A_1)J_0(A_2) - \sin\left(\delta_1^0\right)J_2(A_1)\Bigg)
\end{aligned}
$$

I can then write the expression for $I_{2\omega_1}$ in terms of the Stokes elements.

$$
\begin{aligned}
I_{2\omega_1} =& \frac{1}{\sqrt{2}}\Bigg[-\left(\sin(\delta_1^0)\sin(\delta_2^0)J_2(A_1)J_0(A_2) + \cos(\delta_1^0)J_2(A_1)\right)\cdot \mathbf{s}_2 \\
&+ \left(\cos\left(\delta_1^0\right)\sin\left(\delta_2^0\right)J_2(A_1)J_0(A_2) - \sin\left(\delta_1^0\right)J_2(A_1)\right)\cdot \mathbf{s}_3\Bigg]
\end{aligned}
\tag{3.26}
$$

3.1.6 Expressing $I_{2\omega_2}$

The approach is the same as in previous sections.

$$I_{2\omega_2} = \frac{\int_{-\pi}^{\pi} \mathbf{s}_0' \cdot \cos(2\omega_2 t)dt}{\pi}$$

$$\begin{aligned}
&= \int_{-\pi}^{\pi} \Bigg[\frac{1}{2\pi}\mathbf{s}_0 + \frac{\sqrt{2}}{4\pi} \cos\left(A_2 \cos(\omega_2 t) + \delta_2^0\right)\mathbf{s}_1 \\
&+ \frac{\sqrt{2}}{4\pi}\Bigg(\cos\left(A_1 \cos(\omega_1 t) + \delta_1^0\right) \\
&+ \sin\left(A_2 \cos(\omega_2 t) + \delta_2^0\right) \sin\left(A_1 \cos(\omega_1 t) + \delta_1^0\right)\Bigg)\mathbf{s}_2 \\
&+ \frac{\sqrt{2}}{4\pi}\Bigg(\sin\left(A_1 \cos(\omega_1 t) + \delta_1^0\right) \\
&- \sin\left(A_2 \cos(\omega_2 t) + \delta_2^0\right) \cos\left(A_1 \cos(\omega_1 t) + \delta_1^0\right)\Bigg)\mathbf{s}_3\Bigg] \cdot \cos(2\omega_2 t)dt
\end{aligned}$$

$$\begin{aligned}
&= \mathbf{s}_0 \int_{-\pi}^{\pi} \frac{\cos(2\omega_2 t)}{2\pi}dt + \frac{\sqrt{2}}{4\pi}\Bigg[\mathbf{s}_1 \int_{-\pi}^{\pi} \cos\left(A_2 \cos(\omega_2 t) + \delta_2^0\right)\cos(2\omega_2 t)dt \\
&+ \mathbf{s}_2\Bigg(\int_{-\pi}^{\pi} \cos\left(A_1 \cos(\omega_1 t) + \delta_1^0\right)\cos(2\omega_2 t)dt \\
&+ \int_{-\pi}^{\pi} \sin\left(A_2 \cos(\omega_2 t) + \delta_2^0\right)\sin\left(A_1 \cos(\omega_1 t) + \delta_1^0\right)\cos(2\omega_2 t)dt\Bigg) \\
&+ \mathbf{s}_3\Bigg(\int_{-\pi}^{\pi} \sin\left(A_1 \cos(\omega_1 t) + \delta_1^0\right)\cos(2\omega_2 t)dt \\
&- \int_{-\pi}^{\pi} \sin\left(A_2 \cos(\omega_2 t) + \delta_2^0\right)\cos\left(A_1 \cos(\omega_1 t) + \delta_1^0\right)\cos(2\omega_2 t)dt\Bigg)\Bigg] \qquad (3.27)
\end{aligned}$$

(3.28)

Once again, the expression is broken down into the contribution from each Stokes element for clarity.

$$\mathbf{s}_0 \int_{-\pi}^{\pi} \frac{\cos(2\omega_2 t)}{2\pi}dt$$

$$= 0 \qquad (3.29)$$

$$
\begin{aligned}
&\mathbf{s}_1 \cdot \frac{\sqrt{2}}{4\pi} \int_{-\pi}^{\pi} \cos\left(A_2 \cos\left(\omega_2 t\right) + \delta_2^0\right) \cos(2\omega_2 t) dt \\
&= \mathbf{s}_1 \cdot \frac{\sqrt{2}}{4\pi} \int_{-\pi}^{\pi} \Bigg[\cos\left(A_2 \cos\left(\omega_2 t\right)\right) \cos\left(\delta_2^0\right) \cos(2\omega_2 t) \\
&- \sin\left(A_2 \cos\left(\omega_2 t\right)\right) \sin\left(\delta_2^0\right) \cos(2\omega_2 t) \Bigg] dt \\
&= \mathbf{s}_1 \cdot \frac{\sqrt{2}}{4\pi} \Bigg[\cos\left(\delta_2^0\right) \int_{-\pi}^{\pi} \cos\left(A_2 \cos\left(\omega_2 t\right)\right) \cos(2\omega_2 t) dt \quad \rightarrow -2\pi J_2(A_2) \\
&- \sin\left(\delta_2^0\right) \int_{-\pi}^{\pi} \sin\left(A_2 \cos\left(\omega_2 t\right)\right) \cos(2\omega_2 t) dt \Bigg] \quad \rightarrow 0 \qquad (3.30) \\
&= \mathbf{s}_1 \cdot \frac{-1}{\sqrt{2}} \cos(\delta_2^0) J_2(A_2) \qquad (3.31) \\
&\mathbf{s}_2 \cdot \frac{\sqrt{2}}{4\pi} \Bigg[\int_{-\pi}^{\pi} \cos\left(A_1 \cos\left(\omega_1 t\right) + \delta_1^0\right) \cos(2\omega_2 t) dt \qquad (3.32) \\
&+ \int_{-\pi}^{\pi} \sin\left(A_2 \cos\left(\omega_2 t\right) + \delta_2^0\right) \sin\left(A_1 \cos\left(\omega_1 t\right) + \delta_1^0\right) \cos(2\omega_2 t) dt \Bigg] \\
&= \mathbf{s}_2 \cdot \frac{\sqrt{2}}{4\pi} \Bigg(\int_{-\pi}^{\pi} \Bigg[\cos\left(A_1 \cos\left(\omega_1 t\right)\right) \cos\left(\delta_1^0\right) \cos(2\omega_2 t) \\
&- \sin\left(A_1 \cos\left(\omega_1 t\right)\right) \sin\left(\delta_1^0\right) \cos(2\omega_2 t) \Bigg] dt \\
&+ \int_{-\pi}^{\pi} \Bigg[\cos\left(\delta_2^0\right) \sin\left(A_2 \cos\left(\omega_2 t\right)\right) + \sin\left(\delta_2^0\right) \cos\left(A_2 \cos\left(\omega_2 t\right)\right) \Bigg] \\
&\cdot \Bigg[\cos\left(\delta_1^0\right) \sin\left(A_1 \cos\left(\omega_1 t\right)\right) + \sin\left(\delta_1^0\right) \cos\left(A_1 \cos\left(\omega_1 t\right)\right) \Bigg] \cos(2\omega_2 t) dt \Bigg)
\end{aligned}
$$

$$
\begin{aligned}
&= \mathbf{s}_2 \cdot \frac{\sqrt{2}}{4\pi}\Bigg(\cos\left(\delta_1^0\right) \cancelto{0}{\int_{-\pi}^{\pi} \cos\left(A_1 \cos\left(\omega_1 t\right)\right) \cos(2\omega_2 t) dt} \\
&- \sin\left(\delta_1^0\right) \cancelto{0}{\int_{-\pi}^{\pi} \sin\left(A_1 \cos\left(\omega_1 t\right)\right) \cos(2\omega_2 t) dt} \\
&+ \sin\left(\delta_1^0\right) \sin\left(\delta_2^0\right) \cancelto{-2\pi J_0(A_1) J_2(A_2)}{\int_{-\pi}^{\pi} \cos\left(A_1 \cos\left(\omega_1 t\right)\right) \cos\left(A_2 \cos\left(\omega_2 t\right)\right) \cos(2\omega_2 t) dt} \\
&+ \cos\left(\delta_1^0\right) \sin\left(\delta_2^0\right) \cancelto{0}{\int_{-\pi}^{\pi} \sin\left(A_1 \cos\left(\omega_1 t\right)\right) \cos\left(A_2 \cos\left(\omega_2 t\right)\right) \cos(2\omega_2 t) dt} \\
&+ \sin\left(\delta_1^0\right) \cos\left(\delta_2^0\right) \cancelto{0}{\int_{-\pi}^{\pi} \cos\left(A_1 \cos\left(\omega_1 t\right)\right) \sin\left(A_2 \cos\left(\omega_2 t\right)\right) \cos(2\omega_2 t) dt} \\
&+ \cos\left(\delta_1^0\right) \cos\left(\delta_2^0\right) \cancelto{0}{\int_{-\pi}^{\pi} \sin\left(A_1 \cos\left(\omega_1 t\right)\right) \sin\left(A_2 \cos\left(\omega_2 t\right)\right) \cos(2\omega_2 t) dt}\Bigg) \\
&= \mathbf{s}_2 \cdot \frac{-1}{\sqrt{2}} \sin(\delta_1^0) \sin(\delta_2^0) J_0(A_1) J_2(A_2)
\end{aligned} \tag{3.33}
$$

$$
\begin{aligned}
&\mathbf{s}_3 \cdot \frac{\sqrt{2}}{4\pi}\Bigg[\int_{-\pi}^{\pi} \sin\left(A_1 \cos\left(\omega_1 t\right) + \delta_1^0\right) \cos(2\omega_2 t) dt \\
&- \int_{-\pi}^{\pi} \sin\left(A_2 \cos\left(\omega_2 t\right) + \delta_2^0\right) \cos\left(A_1 \cos\left(\omega_1 t\right) + \delta_1^0\right) \cos(2\omega_2 t) dt\Bigg] \\
&= \mathbf{s}_3 \cdot \frac{-\sqrt{2}}{4\pi}\Bigg(\int_{-\pi}^{\pi} \Bigg[\cos\left(\delta_2^0\right) \sin\left(A_2 \cos\left(\omega_2 t\right)\right) + \sin\left(\delta_2^0\right) \cos\left(A_2 \cos\left(\omega_2 t\right)\right)\Bigg] \\
&\times \Bigg[\cos\left(\delta_1^0\right) \cos\left(A_1 \cos\left(\omega_1 t\right)\right) - \sin\left(\delta_1^0\right) \sin\left(A_1 \cos\left(\omega_1 t\right)\right)\Bigg] \cdot \cos(2\omega_2 t) dt \\
&- \int_{-\pi}^{\pi} \Bigg[\sin\left(A_1 \cos\left(\omega_1 t\right)\right) \cos\left(\delta_1^0\right) \cos(2\omega_2 t) \\
&+ \cos\left(A_1 \cos\left(\omega_1 t\right)\right) \sin\left(\delta_1^0\right) \cos(2\omega_2 t)\Bigg] dt\Bigg)
\end{aligned}
$$

$$
\begin{aligned}
&= \mathbf{s}_3 \cdot \frac{-\sqrt{2}}{4\pi}\Bigg(\cos\left(\delta_1^0\right)\cos\left(\delta_2^0\right)\int_{-\pi}^{\pi} \cos\left(A_1\cos\left(\omega_1 t\right)\right)\sin\left(A_2\cos\left(\omega_2 t\right)\right)\cos(2\omega_2 t)dt \quad \to 0 \\
&- \sin\left(\delta_1^0\right)\cos\left(\delta_2^0\right)\int_{-\pi}^{\pi} \sin\left(A_1\cos\left(\omega_1 t\right)\right)\sin\left(A_2\cos\left(\omega_2 t\right)\right)\cos(2\omega_2 t)dt \quad \to 0 \\
&+ \cos\left(\delta_1^0\right)\sin\left(\delta_2^0\right)\int_{-\pi}^{\pi} \cos\left(A_1\cos\left(\omega_1 t\right)\right)\cos\left(A_2\cos\left(\omega_2 t\right)\right)\cos(2\omega_2 t)dt \quad \to -2\pi J_0(A_1)J_2(A_2) \\
&- \sin\left(\delta_1^0\right)\sin\left(\delta_2^0\right)\int_{-\pi}^{\pi} \sin\left(A_1\cos\left(\omega_1 t\right)\right)\cos\left(A_2\cos\left(\omega_2 t\right)\right)\cos(2\omega_2 t)dt \quad \to 0 \\
&- \cos\left(\delta_1^0\right)\int_{-\pi}^{\pi} \sin\left(A_1\cos\left(\omega_1 t\right)\right)\cos(2\omega_2 t)dt \quad \to 0 \\
&- \sin\left(\delta_1^0\right)\int_{-\pi}^{\pi} \cos\left(A_1\cos\left(\omega_1 t\right)\right)\cos(2\omega_2 t)dt \quad \to 0 \Bigg) \\
&= \mathbf{s}_3 \cdot \frac{1}{\sqrt{2}}\cos\left(\delta_1^0\right)\sin\left(\delta_2^0\right)J_0(A_1)J_2(A_2)
\end{aligned}
\tag{3.34}
$$

The expression for $I_{2\omega_2}$ can now be written in terms of the Stokes elements.

$$
\begin{aligned}
I_{2\omega_2} = &\frac{-1}{\sqrt{2}}\Big[\cos(\delta_2^0)J_2(A_2)\cdot\mathbf{s}_1 + \sin(\delta_1^0)\sin(\delta_2^0)J_0(A_1)J_2(A_2)\cdot\mathbf{s}_2 \\
&- \cos\left(\delta_1^0\right)\sin\left(\delta_2^0\right)J_0(A_1)J_2(A_2)\cdot\mathbf{s}_3\Big]
\end{aligned}
\tag{3.35}
$$

3.1.7 F coefficient variables

To make things simpler going forward, it makes sense to replace the coefficient expressions with variables, such that the expressions for each of the four lock-in signals can be written

as

$$I_{dc} = \frac{1}{2} \cdot \mathbf{s}_0 + F_{dc,1} \cdot \mathbf{s}_1 + F_{dc,2} \cdot \mathbf{s}_2 + F_{dc,3} \cdot \mathbf{s}_3 \tag{3.36a}$$

$$I_{\omega_1} = F_{1\omega_1,2} \cdot \mathbf{s}_2 + F_{1\omega_1,3} \cdot \mathbf{s}_3 \tag{3.36b}$$

$$I_{2\omega_1} = F_{2\omega_1,2} \cdot \mathbf{s}_2 + F_{2\omega_1,3} \cdot \mathbf{s}_3 \tag{3.36c}$$

$$I_{2\omega_2} = F_{2\omega_2,1} \cdot \mathbf{s}_1 + F_{2\omega_2,2} \cdot \mathbf{s}_2 + F_{2\omega_2,3} \cdot \mathbf{s}_3 \tag{3.36d}$$

The definitions for these coefficients are

$$F_{dc,1} = \frac{1}{2\sqrt{2}} \cos(\delta_2^0) J_0(A_2) \tag{3.37a}$$

$$F_{dc,2} = \frac{1}{2\sqrt{2}} \big(\sin(\delta_1^0) \sin(\delta_2^0) J_0(A_1) J_0(A_2) + \cos(\delta_1^0) J_0(A_1) \big) \tag{3.37b}$$

$$F_{dc,3} = \frac{-1}{2\sqrt{2}} \big(\cos(\delta_1^0) \sin(\delta_2^0) J_0(A_1) J_0(A_2) - \sin(\delta_1^0) J_0(A_1) \big) \tag{3.37c}$$

$$F_{1\omega_1,2} = \frac{1}{\sqrt{2}} \big(\cos\left(\delta_1^0\right) \sin\left(\delta_2^0\right) J_1(A_1) J_0(A_2) - \sin\left(\delta_1^0\right) J_1(A_1) \big) \tag{3.37d}$$

$$F_{1\omega_1,3} = \frac{1}{\sqrt{2}} \big(\sin\left(\delta_1^0\right) \sin\left(\delta_2^0\right) J_1(A_1) J_0(A_2) + \cos\left(\delta_1^0\right) J_1(A_1) \big) \tag{3.37e}$$

$$F_{2\omega_1,2} = \frac{-1}{\sqrt{2}} \big(\sin\left(\delta_1^0\right) \sin\left(\delta_2^0\right) J_2(A_1) J_0(A_2) + \cos\left(\delta_1^0\right) J_2(A_1) \big) \tag{3.37f}$$

$$F_{2\omega_1,3} = \frac{1}{\sqrt{2}} \big(\cos\left(\delta_1^0\right) \sin\left(\delta_2^0\right) J_2(A_1) J_0(A_2) - \sin\left(\delta_1^0\right) J_2(A_1) \big) \tag{3.37g}$$

$$F_{2\omega_2,1} = \frac{-1}{\sqrt{2}} \cos(\delta_2^0) J_2(A_2) \tag{3.37h}$$

$$F_{2\omega_2,2} = \frac{-1}{\sqrt{2}} \sin(\delta_1^0) \sin(\delta_2^0) J_0(A_1) J_2(A_2) \tag{3.37i}$$

$$F_{2\omega_2,3} = \frac{1}{\sqrt{2}} \cos(\delta_1^0) \sin(\delta_2^0) J_0(A_1) J_2(A_2) \tag{3.37j}$$

3.1.8 Isolating the Stokes elements

The simplest route to the desired solutions is to isolate the Stokes elements in reverse order; i.e. starting with $\mathbf{s}_3$ and working back to $\mathbf{s}_0$. The first step is arranging Eq. 3.36b in order to isolate $\mathbf{s}_2$.

$$\begin{aligned} I_{\omega_1} &= F_{1\omega_1,2} \cdot \mathbf{s}_2 + F_{1\omega_1,3} \cdot \mathbf{s}_3 \\ \mathbf{s}_2 &= \frac{I_{\omega_1} - F_{1\omega_1,3} \cdot \mathbf{s}_3}{F_{1\omega_1,2}} \end{aligned} \tag{3.38}$$

This allows the removal of $\mathbf{s}_2$ entirely from Eq. 3.36c.

$$\begin{aligned} I_{2\omega_1} &= F_{2\omega_1,2} \cdot \mathbf{s}_2 + F_{2\omega_1,3} \cdot \mathbf{s}_3 \\ I_{2\omega_1} &= F_{2\omega_1,2} \left(\frac{I_{\omega_1} - F_{1\omega_1,3} \cdot \mathbf{s}_3}{F_{1\omega_1,2}} \right) + F_{2\omega_1,3} \cdot \mathbf{s}_3 \\ F_{1\omega_1,2} I_{2\omega_1} &= F_{2\omega_1,2} I_{\omega_1} - F_{2\omega_1,2} F_{1\omega_1,3} \cdot \mathbf{s}_3 + F_{1\omega_1,2} F_{2\omega_1,3} \cdot \mathbf{s}_3 \end{aligned} \tag{3.39}$$

$$\mathbf{s}_3 = \frac{F_{1\omega_1,2} I_{2\omega_1} - F_{2\omega_1,2} I_{\omega_1}}{F_{1\omega_1,2} F_{2\omega_1,3} - F_{1\omega_1,3} F_{2\omega_1,2}}$$

In Eq. 3.38, $\mathbf{s}_2$ was already isolated, and now I only need to substitute in for $\mathbf{s}_3$ in that expression.

$$\begin{aligned} \mathbf{s}_2 &= \frac{I_{\omega_1} - F_{1\omega_1,3} \cdot \mathbf{s}_3}{F_{1\omega_1,2}} \\ \mathbf{s}_2 &= \frac{I_{\omega_1} - F_{1\omega_1,3} \cdot \frac{F_{1\omega_1,2} I_{2\omega_1} - F_{2\omega_1,2} I_{\omega_1}}{F_{1\omega_1,2} F_{2\omega_1,3} - F_{1\omega_1,3} F_{2\omega_1,2}}}{F_{1\omega_1,2}} \\ \left(F_{1\omega_1,2} F_{2\omega_1,3} - F_{1\omega_1,3} F_{2\omega_1,2}\right) F_{1\omega_1,2} \cdot \mathbf{s}_2 &= F_{1\omega_1,2} F_{2\omega_1,3} I_{\omega_1} - \cancel{F_{1\omega_1,3} F_{2\omega_1,2} I_{\omega_1}} \\ &\quad - F_{1\omega_1,3} F_{1\omega_1,2} I_{2\omega_1} + \cancel{F_{1\omega_1,3} F_{2\omega_1,2} I_{\omega_1}} \\ \left(F_{1\omega_1,2} F_{2\omega_1,3} - F_{1\omega_1,3} F_{2\omega_1,2}\right) \cancel{F_{1\omega_1,2}} \cdot \mathbf{s}_2 &= \cancel{F_{1\omega_1,2}} F_{2\omega_1,3} I_{\omega_1} - F_{1\omega_1,3} \cancel{F_{1\omega_1,2}} I_{2\omega_1} \\ \mathbf{s}_2 &= \frac{F_{2\omega_1,3} I_{\omega_1} - F_{1\omega_1,3} I_{2\omega_1}}{F_{1\omega_1,2} F_{2\omega_1,3} - F_{1\omega_1,3} F_{2\omega_1,2}} \end{aligned} \tag{3.40}$$

Now I can re-work Eq. 3.36d in terms of $\mathbf{s}_2$, substituting in these above expressions for $\mathbf{s}_2$ and $\mathbf{s}_3$.

$$
\begin{aligned}
I_{2\omega_2} =& F_{2\omega_2,1}\cdot\mathbf{s}_1 + F_{2\omega_2,2}\cdot\mathbf{s}_2 + F_{2\omega_2,3}\cdot\mathbf{s}_3 \\
I_{2\omega_2} =& F_{2\omega_2,1}\cdot\mathbf{s}_1 + F_{2\omega_2,2}\cdot\frac{F_{2\omega_1,3}I_{\omega_1} - F_{1\omega_1,3}I_{2\omega_1}}{F_{1\omega_1,2}F_{2\omega_1,3} - F_{1\omega_1,3}F_{2\omega_1,2}} \\
&+ F_{2\omega_2,3}\cdot\frac{F_{1\omega_1,2}I_{2\omega_1} - F_{2\omega_1,2}I_{\omega_1}}{F_{1\omega_1,2}F_{2\omega_1,3} - F_{1\omega_1,3}F_{2\omega_1,2}} \\
F_{2\omega_2,1}\cdot\mathbf{s}_1 =& I_{2\omega_2} \\
&- \frac{F_{2\omega_2,2}F_{2\omega_1,3}I_{\omega_1} - F_{2\omega_2,2}F_{1\omega_1,3}I_{2\omega_1} + F_{2\omega_2,3}F_{1\omega_1,2}I_{2\omega_1} - F_{2\omega_2,3}F_{2\omega_1,2}I_{\omega_1}}{F_{1\omega_1,2}F_{2\omega_1,3} - F_{1\omega_1,3}F_{2\omega_1,2}}
\end{aligned}
$$

$$
\begin{aligned}
\mathbf{s}_1 =& \frac{\left(F_{2\omega_1,2}F_{2\omega_2,3} - F_{2\omega_1,3}F_{2\omega_2,2}\right)I_{\omega_1} + \left(F_{1\omega_1,3}F_{2\omega_2,2} - F_{1\omega_1,2}F_{2\omega_2,3}\right)I_{2\omega_1}}{F_{2\omega_2,1}\left(F_{1\omega_1,2}F_{2\omega_1,3} - F_{1\omega_1,3}F_{2\omega_1,2}\right)} \\
&+ \frac{I_{2\omega_2}}{F_{2\omega_2,1}}
\end{aligned} \tag{3.41}
$$

Similarly, I can simply substitute my expressions for $\mathbf{s}_1$, $\mathbf{s}_2$ and $\mathbf{s}_3$ into Eq. 3.36a in order to determine the expression for $\mathbf{s}_0$.

$$
\begin{aligned}
I_{dc} =& \frac{1}{2}\cdot\mathbf{s}_0 + F_{dc,1}\cdot\mathbf{s}_1 + F_{dc,2}\cdot\mathbf{s}_2 + F_{dc,3}\cdot\mathbf{s}_3 \\
\frac{1}{2}\cdot\mathbf{s}_0 =& I_{dc} - \Bigg(\Bigg(\frac{\left(F_{2\omega_1,2}F_{2\omega_2,3} - F_{2\omega_1,3}F_{2\omega_2,2}\right)I_{\omega_1}}{F_{2\omega_2,1}\left(F_{1\omega_1,2}F_{2\omega_1,3} - F_{1\omega_1,3}F_{2\omega_1,2}\right)} \\
&+ \frac{\left(F_{1\omega_1,3}F_{2\omega_2,2} - F_{1\omega_1,2}F_{2\omega_2,3}\right)I_{2\omega_1}}{F_{2\omega_2,1}\left(F_{1\omega_1,2}F_{2\omega_1,3} - F_{1\omega_1,3}F_{2\omega_1,2}\right)} + \frac{I_{2\omega_2}}{F_{2\omega_2,1}} \Bigg) F_{dc,1} \\
&+ \left(\frac{F_{2\omega_1,3}I_{\omega_1} - F_{1\omega_1,3}I_{2\omega_1}}{F_{1\omega_1,2}F_{2\omega_1,3} - F_{1\omega_1,3}F_{2\omega_1,2}}\right)F_{dc,2} + \left(\frac{F_{1\omega_1,2}I_{2\omega_1} - F_{2\omega_1,2}I_{\omega_1}}{F_{1\omega_1,2}F_{2\omega_1,3} - F_{1\omega_1,3}F_{2\omega_1,2}}\right)F_{dc,3}\Bigg) \\
\mathbf{s}_0 =& 2I_{dc} - 2\Bigg(\Bigg(\frac{\left(F_{2\omega_1,2}F_{2\omega_2,3}F_{dc,1} - F_{2\omega_1,3}F_{2\omega_2,2}F_{dc,1}\right)I_{\omega_1}}{F_{2\omega_2,1}\left(F_{1\omega_1,2}F_{2\omega_1,3} - F_{1\omega_1,3}F_{2\omega_1,2}\right)} \\
&+ \frac{\left(F_{1\omega_1,3}F_{2\omega_2,2}F_{dc,1} - F_{1\omega_1,2}F_{2\omega_2,3}F_{dc,1}\right)I_{2\omega_1}}{F_{2\omega_2,1}\left(F_{1\omega_1,2}F_{2\omega_1,3} - F_{1\omega_1,3}F_{2\omega_1,2}\right)} + \frac{F_{dc,1}I_{2\omega_2}}{F_{2\omega_2,1}} \Bigg) \\
&+ \left(\frac{F_{2\omega_1,3}F_{dc,2}I_{\omega_1} - F_{1\omega_1,3}F_{dc,2}I_{2\omega_1}}{F_{1\omega_1,2}F_{2\omega_1,3} - F_{1\omega_1,3}F_{2\omega_1,2}}\right) + \left(\frac{F_{1\omega_1,2}F_{dc,3}I_{2\omega_1} - F_{2\omega_1,2}F_{dc,3}I_{\omega_1}}{F_{1\omega_1,2}F_{2\omega_1,3} - F_{1\omega_1,3}F_{2\omega_1,2}}\right)\Bigg)
\end{aligned}
$$

$$
\begin{aligned}
\mathbf{s}_0 =& 2I_{dc} - \frac{2}{F_{2\omega_2,1}\left(F_{1\omega_1,2}F_{2\omega_1,3} - F_{1\omega_1,3}F_{2\omega_1,2}\right)}\Bigg(\left(F_{dc,1}F_{2\omega_1,2}F_{2\omega_2,3}\right. \\
&\left. - F_{dc,1}F_{2\omega_1,3}F_{2\omega_2,2} + F_{dc,2}F_{2\omega_1,3}F_{2\omega_2,1} - F_{dc,3}F_{2\omega_1,2}F_{2\omega_2,1}\right)\cdot I_{\omega_1} \\
&+ \left(F_{dc,1}F_{1\omega_1,3}F_{2\omega_2,2} - F_{dc,1}F_{1\omega_1,2}F_{2\omega_2,3}\right. \\
&\left. + F_{dc,3}F_{1\omega_1,2}F_{2\omega_2,1} - F_{dc,2}F_{1\omega_1,3}F_{2\omega_2,1}\right)\cdot I_{2\omega_1}\Bigg) \\
&+ 2\frac{F_{dc,1}}{F_{2\omega_2,1}}\cdot I_{2\omega_2} \qquad (3.42)
\end{aligned}
$$

(3.43)

Using a Stokes polarimeter comprised of a two photoelastic modulators, operating at 0° and 45° respectively, and at completely different frequencies (having $x\omega_1 = y\omega_2$ at only very high integer values of x and y), followed by a polarizer with its optical axis at 22.5°, this derivation shows how the signal demodulated at four different frequencies can be used to calculate the Stokes vector at any wavelength, provided the amplitude and static retardation of the PEMs is known at that wavelength. The expressions to calculate each

Stokes element are

$$\mathbf{s}_0 = 2I_{dc} \tag{3.44}$$

$$- 2\Bigg(\frac{F_{dc,1}F_{2\omega_1,2}F_{2\omega_2,3} - F_{dc,1}F_{2\omega_1,3}F_{2\omega_2,2} + F_{dc,2}F_{2\omega_1,3}F_{2\omega_2,1} - F_{dc,3}F_{2\omega_1,2}F_{2\omega_2,1}}{F_{2\omega_2,1}\left(F_{1\omega_1,2}F_{2\omega_1,3} - F_{1\omega_1,3}F_{2\omega_1,2}\right)} \cdot I_{\omega_1} \tag{3.45}$$

$$+ \frac{F_{dc,1}F_{1\omega_1,3}F_{2\omega_2,2} - F_{dc,1}F_{1\omega_1,2}F_{2\omega_2,3} + F_{dc,3}F_{1\omega_1,2}F_{2\omega_2,1} - F_{dc,2}F_{1\omega_1,3}F_{2\omega_2,1}}{F_{2\omega_2,1}\left(F_{1\omega_1,2}F_{2\omega_1,3} - F_{1\omega_1,3}F_{2\omega_1,2}\right)} \cdot I_{2\omega_1} \tag{3.46}$$

$$+ \frac{F_{dc,1}}{F_{2\omega_2,1}} \cdot I_{2\omega_2} \Bigg) \tag{3.47}$$

$$\mathbf{s}_1 = \frac{\left(F_{2\omega_1,2}F_{2\omega_2,3} - F_{2\omega_1,3}F_{2\omega_2,2}\right) I_{\omega_1} + \left(F_{1\omega_1,3}F_{2\omega_2,2} - F_{1\omega_1,2}F_{2\omega_2,3}\right) I_{2\omega_1}}{F_{2\omega_2,1}\left(F_{1\omega_1,2}F_{2\omega_1,3} - F_{1\omega_1,3}F_{2\omega_1,2}\right)} + \frac{I_{2\omega_2}}{F_{2\omega_2,1}} \tag{3.48}$$

$$\mathbf{s}_2 = \frac{F_{2\omega_1,3}I_{\omega_1} - F_{1\omega_1,3}I_{2\omega_1}}{F_{1\omega_1,2}F_{2\omega_1,3} - F_{1\omega_1,3}F_{2\omega_1,2}} \tag{3.49}$$

$$\mathbf{s}_3 = \frac{F_{1\omega_1,2}I_{2\omega_1} - F_{2\omega_1,2}I_{\omega_1}}{F_{1\omega_1,2}F_{2\omega_1,3} - F_{1\omega_1,3}F_{2\omega_1,2}} \tag{3.50}$$

$$\tag{3.51}$$

where

$$
\begin{aligned}
F_{dc,1} &= \frac{1}{2\sqrt{2}}\cos(\delta_2^0)J_0(A_2) \\
F_{dc,2} &= \frac{1}{2\sqrt{2}}\big(\sin(\delta_1^0)\sin(\delta_2^0)J_0(A_1)J_0(A_2) + \cos(\delta_1^0)J_0(A_1)\big) \\
F_{dc,3} &= \frac{-1}{2\sqrt{2}}\big(\cos(\delta_1^0)\sin(\delta_2^0)J_0(A_1)J_0(A_2) - \sin(\delta_1^0)J_0(A_1)\big) \\
F_{1\omega_1,2} &= \frac{1}{\sqrt{2}}\big(\cos\left(\delta_1^0\right)\sin\left(\delta_2^0\right)J_1(A_1)J_0(A_2) - \sin\left(\delta_1^0\right)J_1(A_1)\big) \\
F_{1\omega_1,3} &= \frac{1}{\sqrt{2}}\big(\sin\left(\delta_1^0\right)\sin\left(\delta_2^0\right)J_1(A_1)J_0(A_2) + \cos\left(\delta_1^0\right)J_1(A_1)\big) \\
F_{2\omega_1,2} &= \frac{-1}{\sqrt{2}}\big(\sin\left(\delta_1^0\right)\sin\left(\delta_2^0\right)J_2(A_1)J_0(A_2) + \cos\left(\delta_1^0\right)J_2(A_1)\big) \\
F_{2\omega_1,3} &= \frac{1}{\sqrt{2}}\big(\cos\left(\delta_1^0\right)\sin\left(\delta_2^0\right)J_2(A_1)J_0(A_2) - \sin\left(\delta_1^0\right)J_2(A_1)\big) \\
F_{2\omega_2,1} &= \frac{-1}{\sqrt{2}}\cos(\delta_2^0)J_2(A_2) \\
F_{2\omega_2,2} &= \frac{-1}{\sqrt{2}}\sin(\delta_1^0)\sin(\delta_2^0)J_0(A_1)J_2(A_2) \\
F_{2\omega_2,3} &= \frac{1}{\sqrt{2}}\cos(\delta_1^0)\sin(\delta_2^0)J_0(A_1)J_2(A_2)
\end{aligned}
$$

Experimentally, the amplitudes and static retardations for each PEM at every wavelength in the spectrum are first calibrated, for which methods have been previously established [26, 85, 86], and used in the calculations of the Stokes elements. As mentioned previously, the experimental data result in four frequency-domain spectra. At each wavelength, I extract I_{DC}, I_{2b}, I_{2a} and I_{1a}, and these values, along with the values for A and δ_0 for each PEM are substituted into Eqs. 3.51. The result is a frequency-domain spectrum for each Stokes element.

3.2 Interpretation of data and results

Now that a working instrument has been described, I illustrate measurement of Stokes vectors in the mid-infrared. In addition to calculating the expected Stokes vectors using known incident polarization states and Mueller matrices of well-characterized samples, I use calibration data to model the expected frequency-domain spectra from the instrument in

order to validate the methods presented above. As an example, I first consider light linearly polarized at 60°. Experimentally, this is achieved with the polarizer $\mathbf{P}$ in Fig. 3.1, but $\mathbf{S}$ absent. For my simulation, the frequencies of the two PEMs are set such that $\omega_1 \neq \omega_2$, $\omega_1 \neq 2\omega_2$ and $2\omega_1 \neq \omega_2$, achieved using $\omega_1/2\pi = 37$ kHz and $\omega_2/2\pi = 50$ kHz. For each frequency in the region of interest (from 2.5–11 μm), I create a 100 μs time vector. Time-dependent retardations of the PEMs were introduced previously, and their Mueller matrices described by Eqs. 3.4. The resultant Stokes vector at the detector, $\mathbf{s}'$, is obtained by Mueller matrix algebra

$$\mathbf{s}' = \mathbf{P}(22.5^\circ) \cdot \mathbf{M}_2(\delta_2^0, 45^\circ) \cdot \mathbf{M}_1(\delta_1^0, 0^\circ) \cdot \mathbf{s}. \tag{3.52}$$

The first element of the resultant Stokes vector represents the intensity of the signal at the detector, and so I end up with a representation of the detector waveform as would be supplied to the lock-in amplifiers in the experiment. The Fourier coefficients of interest for this waveform with a period of 100 μs are then obtained at 100 kHz ($2\omega_2$), 74 kHz ($2\omega_1$) and 37 kHz (ω_1). This results in what I will refer to from here on as the I_{DC}, I_{2b}, I_{2a} and I_{1a} signals in the frequency domain. To enable comparison of these signals with experimental results, the last four signals are normalized to I_{DC}. Eqs. 3.51 then provide spectra of the normalized Stokes vector elements at each wavelength of interest. As shown in Fig. 3.2b, the measured wavelength-domain spectra for I_{2b}/I_{DC} and I_{2a}/I_{DC} are in excellent agreement with the model based purely on the predicted Stokes vector and Eqs. 3.36. The normalized Stokes vectors (Fig. 3.2b) are at their expected values of $\mathbf{s} = [1 \ -1/2 \ \sqrt{3}/2 \ 0]^T$ throughout the wavelength region, consistent with a 60° linearly-polarized input state. As a more rigorous demonstration of the broadband operation of this mid-infrared polarimeter, I have also measured the Stokes vectors of linearly-polarized light at 0° transmitted through a quartz waveplate, in the sample position represented by $\mathbf{S}$ in Fig. 3.1. The optic is multi-order $\lambda/4$ for 632.8 nm, and is oriented with its fast axis at 60°. Interferograms collected for this experiment are shown in Fig. 3.2d. The Fourier-transformed signals are indicated in points in Fig. 3.2e from 2.5–3 μm, and

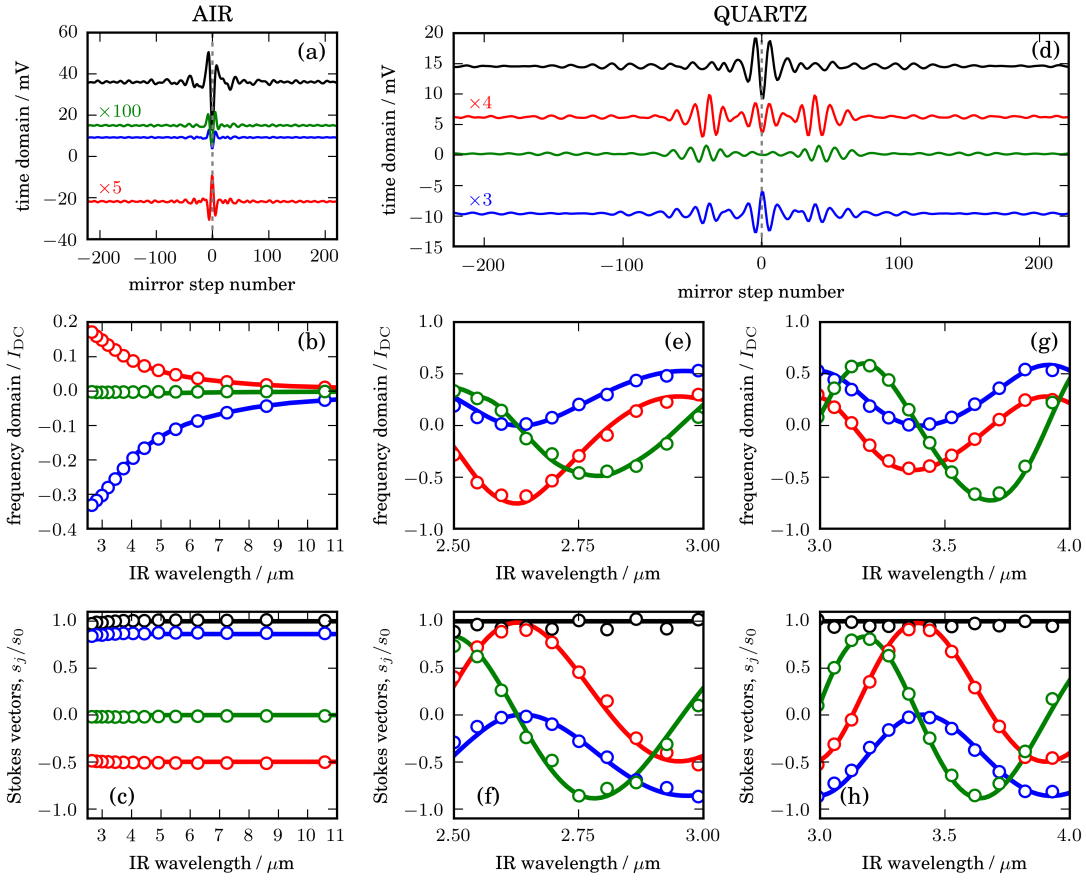

Figure 3.2: (a) Double-sided interferograms for 60° linearly polarized light collected in the step-scan mode of the FTIR, illustrating the DC (black), I_{2b} (red), I_{2a} (blue), and I_{1a} (green) components as demodulated by the lock-in amplifiers. (b) Fourier-transformed signals from 3–11 μm, with I_{2b}/I_{DC} in red, I_{2a}/I_{DC} in blue and I_{1a}/I_{DC} in green. Points are experimental data; lines are model obtained using Eqs. 3.36. (c) Resulting Stokes vector elements after processing the data using Eqs. 3.51 with s_1/s_0 in red, s_2/s_0 in blue, s_3/s_0 in green, and the degree of polarization in black. (d) Interferograms collected when a quartz waveplate is in the beam path, with corresponding (e) Fourier-transformed signals and (f) Stokes vectors in the 2.5–3 μm region, (g,h) 3–4 μm region. The solid lines in (e,f) are calculated based on literature dispersion data for quartz up to 3 μm. The lines in (g,h) are using dispersion data obtained in this experiment; further details of this determination appear in Fig. 3.3.

resulting Stokes vector elements in Fig. 3.2f. Again, the experimental data are indicated by points. The lines are calculated from the ordinary n_o and extraordinary (n_e) dispersion data from Radhakrishnan [87, 88]. These data are available only to 3 μm, the commonly accepted transparency limit for quartz where the absorption coefficient remains negligible for many applications. The periodicity reveals that this multi-order retarder has an absolute retardation 17.25 λ at 632.8 nm (effectively $\lambda/4$).

For some applications, however, quartz is still a useful choice for wavelengths up to 4 μm. This is particularly true for nonlinear optical experiments such as visible-infrared sum-frequency generation, where optics need to be transparent to visible and infrared wavelengths [89]. Materials with better transparency than quartz in this region are typically opaque to visible wavelengths. This is also true in UV-vis-IR experiments where multi-wavelength or broadband sources are employed. The data points in Fig. 3.2g and h are an example of the frequency-domain signals and resulting Stokes vectors in this extended wavelength operation region. Although there is no Δn dispersion data readily available in the 3–4 μm region, I am now in a position to provide this from my measured Stokes vectors. This is plotted as $\Delta n = n_e - n_o$ in Fig. 3.3a and retardation in units of fractional wavelength in Fig. 3.3b, over the entire 2.5–4 μm region. For comparison, the literature curves are overlaid in dashed red lines, up to 3 μm. It has been shown that such an approach may be used to determine the dispersion of the birefringence [26]. I therefore fit Δn to a third-degree polynomial to obtain the relationship

$$\Delta n = a\lambda^3 + b\lambda^2 + c\lambda + d \tag{3.53}$$

displayed with the solid black line in Fig. 3.3a, and transformed into retardation taking the thickness of the sample into account as the solid black in line in Fig. 3.3b. Although Cauchy's and Sellmeier equations are more common dispersion models for the refractive index, I use a polynomial as we are fitting the birefringence in this measurement, without access to the refractive index data directly. It is interesting to note that, although this derived dispersion model provides a better description of Δn in the 2–3 μm region, the literature

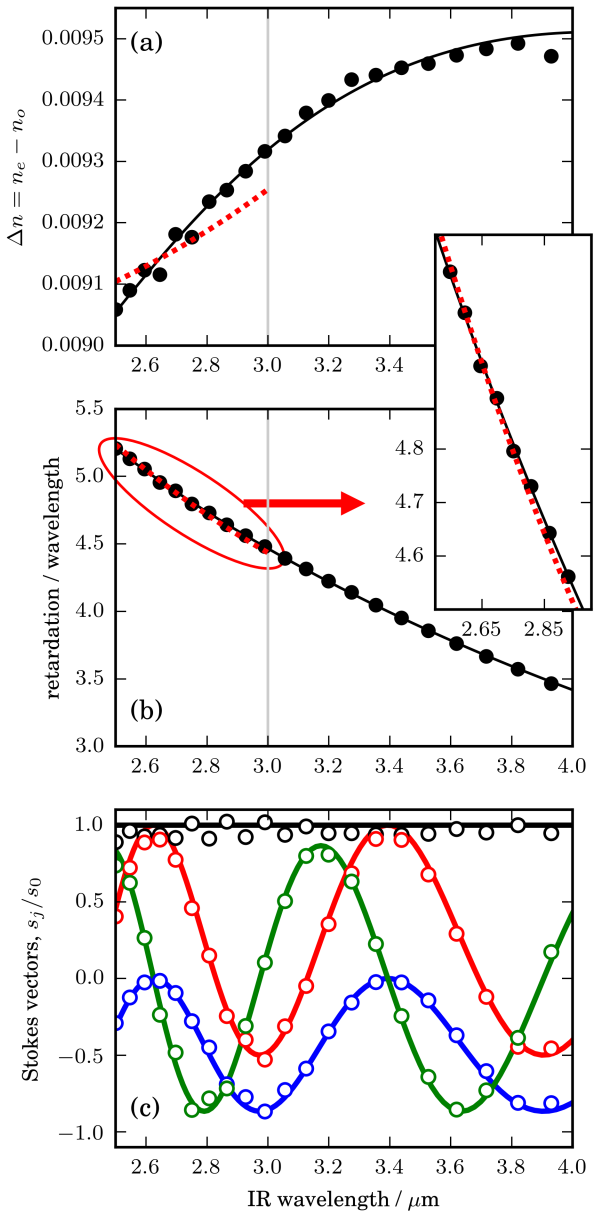

Figure 3.3: (a) Birefringence dispersion as determined from (b) the sample's retardation and thickness, ultimately from (c) the measured Stokes vectors. Experimental data indicated by points. The black line in (a) is a fit to a third-degree dispersion model, given in Eq. 3.53 with $a = 7.624 \times 10^{-5}$, $b = -9.626 \times 10^{-4}$, $c = 4.112 \times 10^{-3}$, and $d = 3.591 \times 10^{-3}$. The corresponding literature model is indicated by the dashed red line up to 3 μm. The inset to (b) shows a zoom-in of the difference between our fit data and the literature-predicted retardation. The model Stokes vectors, indicated by lines in (c) are calculated from a fit to the dispersion data over the entire 2.5–4 μm region.

model is sufficient for the retardation. The inset to Fig. 3.3b displays a zoomed in view of this lower wavelength region for inspection. It is important to keep in mind that the literature model was parameterized over a very wide wavelength region (180 nm to 3 μm), and so this edge of mid-infrared represents the extremity of Radhakrishnan's range, with the fitting weighted towards the UV-vis and near-IR regions. It is therefore not surprising that my limited-region dispersion model should fit the data better in the 2.5–4 μm range. Eq. 3.53 has been used to construct the model frequency domain signals (lines in Fig. 3.2g) and Stokes vectors (lines in Fig. 3.2h) for the 3–4 μm region, and model Stokes vectors in the entire wavelength span in Fig. 3.3c.

3.3 Conclusion

I have demonstrated that a mid-infrared instrument based on an FTIR and photoelastic modulators is capable of broadband spectropolarimetry. The operating wavelength region of such an instrument is only limited by the optics used in the interferometer beamsplitter, the modulator material, and any lenses used in focusing the beam. This lifts the sensitivity limitation of dispersive mid-IR instruments. The instrumentation described is equally applicable using a quantum cascade laser (QCL) source, with the wavelength stepped instead of the mirror position. Unlike scanning instruments with a dispersive source, the intensity at each wavelength will be strong enough for robust measurements.

Chapter 4

Electro-optic characterization of CZT with DC applied voltage

4.1 Introduction

Cadmium zinc telluride (CZT) is a crystalline material with high infrared transmission from 1 to 20 μm which possesses the Pockels effect, and thus is a candidate for creating variable retardation across the mid-IR. In the previous chapter, I discussed my experimental set-up for broadband Stokes polarimetry measurement across the mid-infrared. By using this instrument, I aim to quantify the electro-optic properties of CZT and evaluate its usefulness as a variable retarder across the mid-IR.

The birefringence developed in CZT is related linearly to the applied voltage as per the Pockels effect. As a class $\bar{4}3m$ crystal, the electro-optic coefficient is r_{41}, and the equation which relates voltage applied in the $[\bar{1}10]$ direction to the retardation (in radians) experienced by light travelling in the $[110]$ direction [90] is

$$\delta = \frac{2\pi}{\lambda} n_0^3 r_{41} E l \tag{4.1}$$

In this equation, l represents the distance the light travels through the crystal, and E is the electric field strength the light experiences. If it can be assumed that the electric field is uniformly distributed throughout the material, then I can make the substitution that $E = V/L$, where L is the distance between electrodes. δ, the retardation, refers to the amount of phase delay between orthogonal components of light.

The ability of a pair of electrodes to create a uniform electric field through a crystal is heavily dependent on the work function of the electrodes with respect to the material to which they are attached. The attachment of the metal to the crystal material creates a metal-semiconductor junction, with CZT being an n-type semiconductor. In such situations, a significant difference in work function between the two components, ϕ_{M} for the electrode and ϕ_{CZT} for the semiconductor material in this case, creates a Schottky barrier when $\phi_{\mathrm{M}} > \phi_{\mathrm{CZT}}$. The depletion region created by this effect leads to a gradient in electric field strength that extends from the metal-semiconductor junction to the edge of the depletion region. The size of this depletion region depends on the disparity in the work functions, and the magnitude of the voltage applied. In the case where $\phi_{\mathrm{M}} < \phi_{\mathrm{CZT}}$, however, an ohmic contact is created, and the electric field is expected to be uniform through the crystal [91]. CZT is studied in this research with two different metals used for electrodes: gold and indium.

4.2 Experimental

4.2.1 Cadmium zinc telluride EO crystals

The two CZT samples that are used in this investigation were grown by Redlen Technologies Inc. in Saanichton, British Columbia using their travelling heater method (THM). They are polished, and feature no anti-reflection coating. The crystals have slightly different dimensions, but are both approximately 50 mm long, and 5 mm in the other two dimensions. On one crystal, two of the long sides opposite one another are metallized with gold electrodes, and gold wires are attached to one end of each face to apply the voltage in the $[\bar{1}10]$ direction. Light propagates along the long axis of the crystal, $[110]$, as shown in Fig. 4.1. On the other crystal, the electrodes are indium, with gold wires attached.

4.2.2 Enclosure for high voltage application

In order to securely position the CZT electro-optic bars for analysis, the sample is rested with no applied pressure in a specially-designed enclosure, which is shown in Fig. 4.2, and

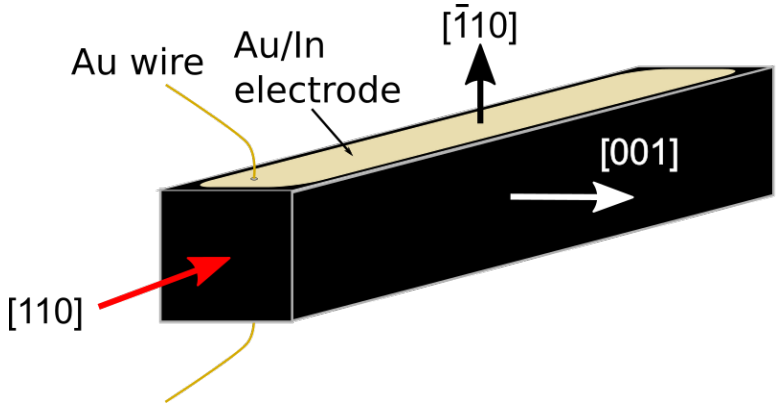

Figure 4.1: Crystal axes and orientation of CZT samples used. Light propagates along the $[110]$ axis and experiences birefringence when voltage is applied on the $[\bar{1}10]$ axis across electrodes on opposite faces.

which was designed and assembled by Andrew McDonald, with the interior PVC milled by Jeff Trafton. High voltage is applied through an SHV cable from the power supply, and a second co-axial outlet on the enclosure allows for measurement of the leakage current through the sample.

The voltage is relayed across its circuitry to two wires which are attached to the crystal's two electrodes. This circuitry is per the manual recommendations of the picoammeter, which can only handle up to 505 V in the event of a short-circuit. The series protection resistor limits short-circuit current to below 1 mA. The parallel low-leakage diodes do not turn on during normal operation with the burden voltage below 200 mV. The circuit is housed in an aluminum enclosure, and the SHV connector shield connection is isolated from the enclosure, both of which reduce measurement noise.

4.2.3 Broadband mid-infared Stokes polarimetry

For all of the experimental analysis methods, an FTIR in step-scan mode is used as the source for materials analysis. For the first scheme, after preparing the incident light polarization state and transmitting through the sample, the Stokes vector is measured using the Stokes polarimeter described in the previous chapter. The advantage of using the Stokes polarimeter to study the electro-optic properties of CZT is that with one configuration, I can

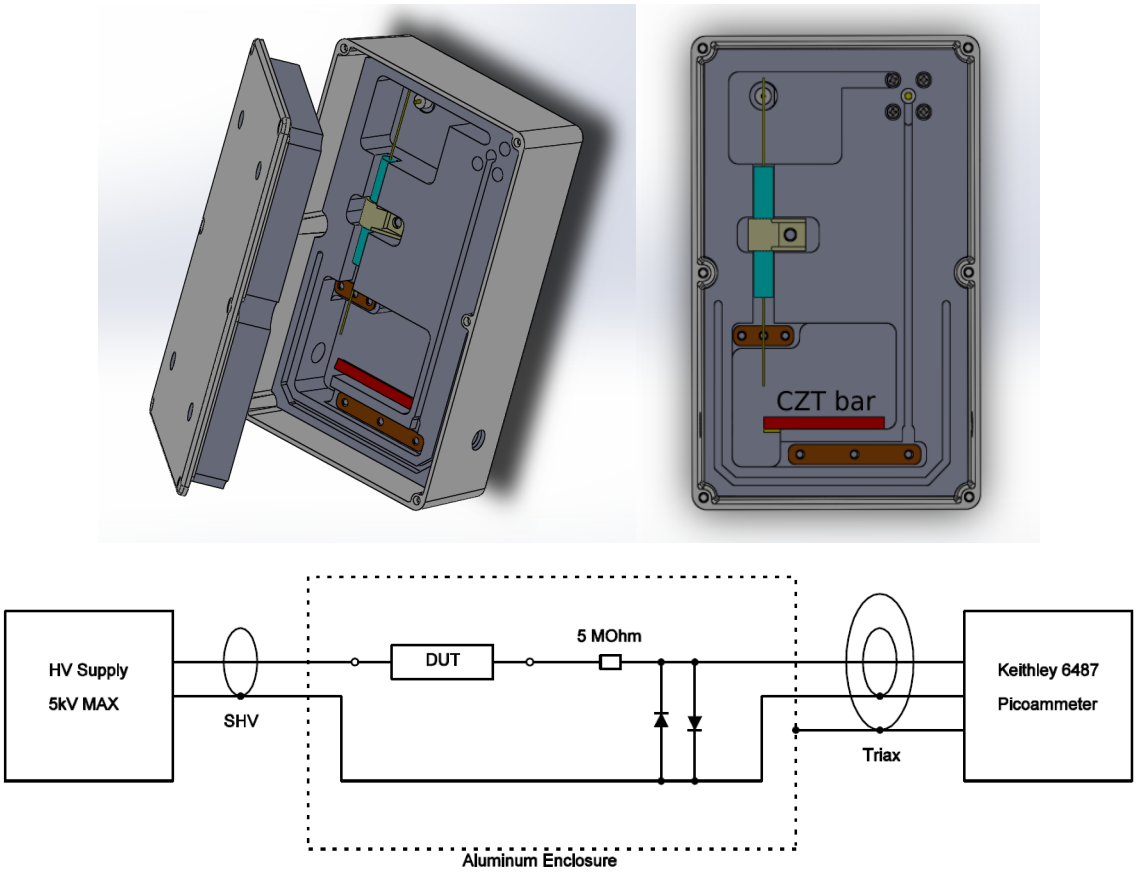

Figure 4.2: At the top, 3-D renderings of the specially-designed enclosure used to house the CZT sample. This allowed the crystal (device under testing, or DUT in the diagram) to be securely held without added pressure, which could change the characteristics of the material. On the bottom, the circuit diagram for applying high voltage and measuring leakage current.

collect a complete picture of the electro-optic effect as well as depolarization across the spectrum, with other configurations being used purely to confirm that no other polarization modulation effects are present.

The incident light is polarized at 0° with respect to the polarimeter, and the crystal's optical axis develops at 45° as voltage is applied. This means that in measuring the resultant Stokes vector, s_2 should remain at zero so long as the only effect of the crystal on the polarization state is the electro-optic effect. From this, the retardation of the crystal can be deduced based on the ratio of s_3 to s_1.

Elements of the Stokes vector are related by Eq. 1.2, where the equality of the sum of

the squares of s_1, s_2 and s_3 to the square of s_0 holds in the case of perfectly polarized light (no depolarization of transmitted light).

Fully polarized light has a degree of polarization of exactly 1. As discussed in previous chapters, if each of the four elements of $\mathbf{s}$ is measured independently, it is possible to describe the azimuth, ellipticity, and handedness of the polarization ellipse, in addition to the fraction of the light that is depolarized.

Many materials which display electro-optic effects also depolarize the light as they modulate its polarization state. In some electro-optic materials, the effect is quite significant. Often, the depolarization of the light is attributed to small scattering bodies within the material. Such scattering is proportional to the inverse of the fourth power of the wavelength, and so is more pronounced at shorter wavelengths.

Depolarization is also expected to occur if all of the beam of light does not encounter the same material properties within a material. When the Stokes vector of the light resulting from transmission through a sample is a superposition of many different polarization states, the result is a degree of polarization less than one.

4.2.4 Polarized IR transmittance measurements

A more conventional and simplistic approach to measuring depolarization of light upon transmission through a sample is to place the sample between two polarizers, with the front polarizer and back polarizer (analyzer) each azimuthally offset from the sample's optical axis by 45°. In one possible configuration, the polarizers are crossed with respect to one another. If the front polarizer is considered to be 0°, then the sample is at 45° and the analyzer at 90°. Unity transmission can be defined by the intensity of light measured after the sample with the analyzer removed.

Assuming no depolarization from the sample, then no light should be transmitted through the analyzer in the case of no retardation from the sample. As the retardation increases, the transmission through the analyzer increases until it reaches a maximum when

the retardation is a half-wave. The transmission then decreases until no light is transmitted with a full-wave retardation. This pattern of maxima at 1 and minima at 0 transmittance, at $2n\pi + 1$ and $2n\pi$ respectively, continues as the retardation increases.

However, any depolarized light will always transmit exactly 50% of its intensity through a polarizer. Thus, if a certain fraction of the light becomes depolarized, D, then the minimum possible intensity transmitted through the back polarizer is $D/2$. Similarly, the maximum possible intensity transmitted is reduced by $D/2$. If, by varying either the wavelength or any parameter that varies retardation, it is possible to take the retardation beyond a half-wave, then this experiment can reveal the amount of depolarization of the sample. In practice, the measurement will report the fraction of light that is polarized, known as the degree of polarization or DOP.

A complementary and confirmatory experiment can be run alongside of it, with the analyzer at 0°, parallel to the front polarizer. In this scheme, the first extremum encountered is a minimum at a half-wave retardation, with its divergence from zero revealing depolarization. The sum of the traces from these two experiments should always be unity, as the same light is being measured by the analyzer in each case, and two orthogonal components are being measured by the two configurations.

In the case of CZT, using an FTIR spectrometer in continuous scan mode allows collection of the transmission spectrum across the mid-IR with a certain voltage applied to the crystal. At high enough voltages, the retardation reaches as much as 1.5-wave retardation at shorter wavelengths. Thus, this method is applicable to measuring depolarization in CZT.

4.2.5 Leakage current measurements

In order to create an electric field within the crystal, it must be ensured that the voltage being applied is not causing a current to arc from one electrode to the other. CZT acts is a dielectric material, but some small current, referred to as leakage current, still manages

to pass through the sample. It is important to monitor the amount of leakage current, as excessive leakage current can lead to material break-down. The leakage current was measured using a pico-ammeter. This measurement is facilitated by the circuitry within the sample holder, which provides a coaxial port to connect directly to the measurement instrumentation. One major advantage of CZT over CdTe is a slightly increased resistivity, which means operating at high voltages is not a problem.

Fig. 4.3 shows the leakage current increasing with applied voltage for both samples. It can be seen that the indium-electrode sample shows slightly greater leakage current than the gold-electrode sample, but with similar shapes.

4.3 Results

4.3.1 Electro-optic characterization

Fig. 4.4 shows the normalized Stokes vectors (each of the four Stokes elements are normalized by s_0, which means s_0 is always unity) across the wavelength spectrum for the range of voltage that the power source is capable of supplying, 0 to 5 kV. The left column shows the results for the gold electrode sample, and the right column shows the results for the indium electrode sample. In both columns, the trends for the Stokes elements fit our expectations. At 0 V, I measure the incident state ($s_1 = 1$,$s_2 = s_3 = 0$), as the crystal is isotropic with no applied voltage. Because of the chosen experimental configuration, s_2 is zero at all voltages and wavelengths. Deviation of s_2 would indicate mis-alignment, or behaviour of the crystal contrary to the expectation of a single optical axis at 45°. As the retardation increases with voltage at any wavelength, s_1 falls from 1 and oscillates sinusoidally, while s_3 increases from zero and also oscillates sinusoidally. Retardation changes occur more rapidly at lower wavelengths, as a given refractive index difference creates more retardation relative to the wavelength if the wavelength is shorter. For instance, the retardation which creates a quarter-wave retardation at 6 μm creates half-wave retardation at 3 μm. Hence it can be seen that each of s_1 and s_3 undergo more

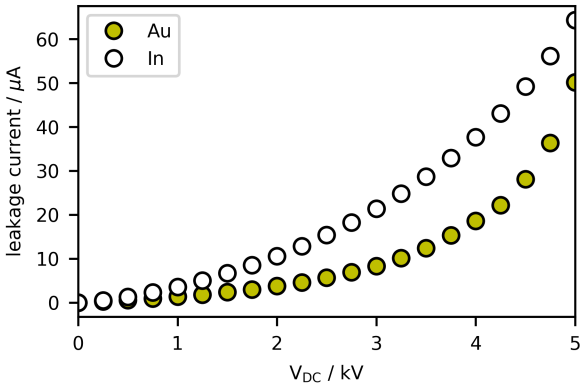

Figure 4.3: The leakage current of the gold- and indium-electrode CZT samples as increasing DC voltage is applied.

oscillation on the 3 μm side of the figure than on the 11 μm side. On the shorter wavelength end of the spectrum, the highs and lows of s_1 and s_3 fail to reach 1 and -1, which would have been the expectation if no depolarization were occurring in this configuration. The degree of polarization everywhere across the measurement range is shown in the bottom row of the Fig. 4.4. The sample with gold electrodes has a significant drop-off in DOP after crossing a threshold at around 750 V. This apparent depolarization is greater at shorter wavelengths, but doesn't seem to grow consistently with more applied voltage. The sample with indium electrodes maintains a DOP close to 1 across all wavelengths and voltages.

The plots of s_1 and s_3 are used to calculate the retardation, which can be more clearly seen in Fig. 4.5. The complete data set is shown in the lower panel, and a few wavelength slices are shown in the upper panel. From these wavelength slices, it can be seen that the electro-optic effect in CZT is linear (Pockels effect) after overcoming a barrier threshold. In the lower panel, black traces show the voltages required to achieve quarter- and half-wave retardation. These traces are of particular interest for applications, as quarter-wave retardation is key for polarization state generation, and half-wave retardation is key for light-valve applications. All of the trends shown in these figures match the expectation for a Pockels material, with the amount of retardation increasing with higher voltage and shorter wavelength. None of these analyses of the retardation consider depolarization, as

the ratio of s_3/s_1 removes the degree of polarization from the equation. What is obtained is the retardation of the light considering only the polarized part which emerges from the sample.

4.3.2 Depolarization

In the bottom left panel of Fig. 4.4, it can be seen that the DOP for the gold-electrode sample starts at 1, meaning that all of the light is polarized, and as the voltage is increase, a threshold is encountered around 750 V after which the light is heavily depolarized on the shorter wavelength end of the spectrum.

In order to further study this measured depolarization, a more common experimental configuration was used consisting of the CZT sample between two polarizers. With the initial polarizer at the same orientation of 0° as in the Stokes polarimetry measurements, and the CZT sample with its optical axis 45° relative to this, the back polarizer was oriented either parallel (0°) or crossed (90°) to this first polarizer, and the transmittance of the light was measured with the FTIR source working in continuous scanning mode at a series of increasing applied voltages. The background used was the parallel-polarizer configuration at 0 V applied voltage. In this scheme, the only decrease in intensity comes from the transmittance of the crystal itself. Theoretically, this should be consistent, and it can be seen that it is in the second panel of Fig. 4.8. Both of these measurement schemes begin with the polarized light at 0° encountering the crystal with its axis at 45°, so the same light intensity will always be present as it encounters the second polarizer. Thus the intensity seen at the detector, relative to this maximum intensity, only varies due to the polarization state and portion of depolarized light.

The data is shown in Fig. 4.6. In a sample with no depolarization, the crossed-polarizer configuration would be expected to show a transmittance of unity when a half-wave retardation is achieved, and a transmittance of 0 when a full-wave retardation is achieved. The parallel-polarizer configuration would be expected to show a transmittance of 0 when a

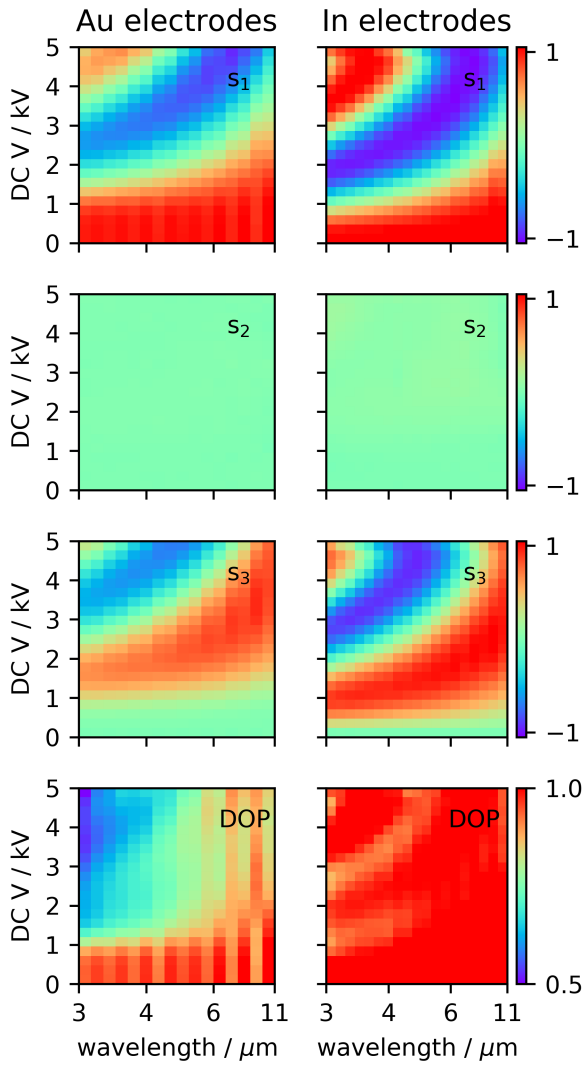

Figure 4.4: The normalized Stokes vectors resulting from a linear polarizer with 0° linearly polarized light incident on a CZT sample with the optical axis oriented at 45°, measured at each wavelength across the instrument range, with voltage applied to the crystal ranging from 0 to 5 kV. s_1, s_2 and s_3 are shown divided by s_0, and these values are used to calculate the degree of polarization via DOP = $\sqrt{s_1^2 + s_2^2 + s_3^2}$.

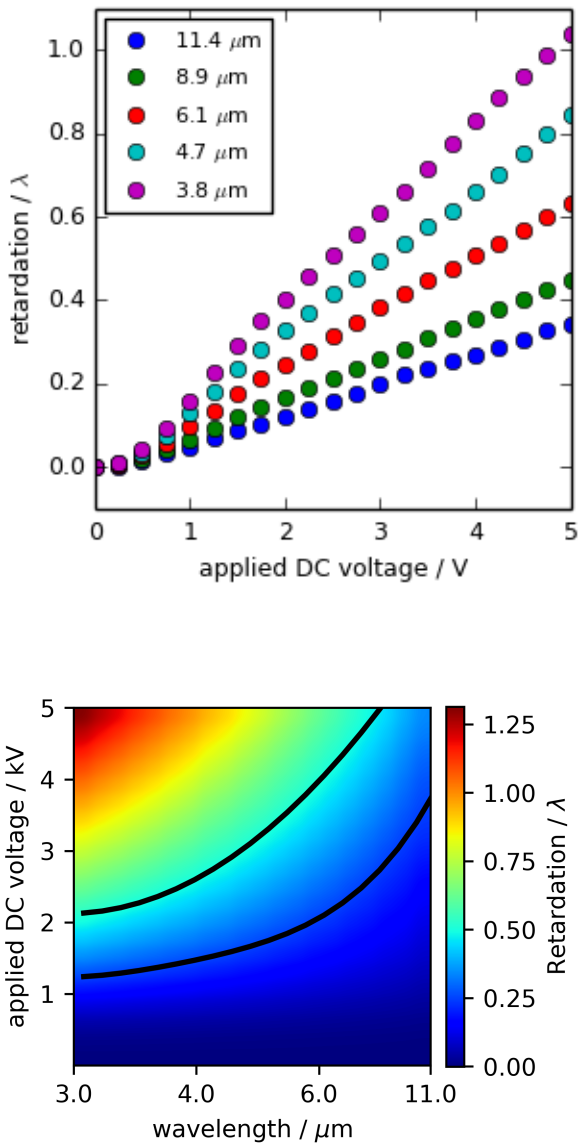

Figure 4.5: The electro-optic effect of CZT displayed in two ways. In the upper panel, the retardation with respect to wavelength is plotted for a few selected wavelengths. This corresponds to vertical slices of the lower panel, which shows the retardation at all of the wavelengths and all of the voltages together. The black traces on the lower panel show the voltages required for quarter- (lower) and half-wave (upper) retardation at each wavelength across the instrument range.

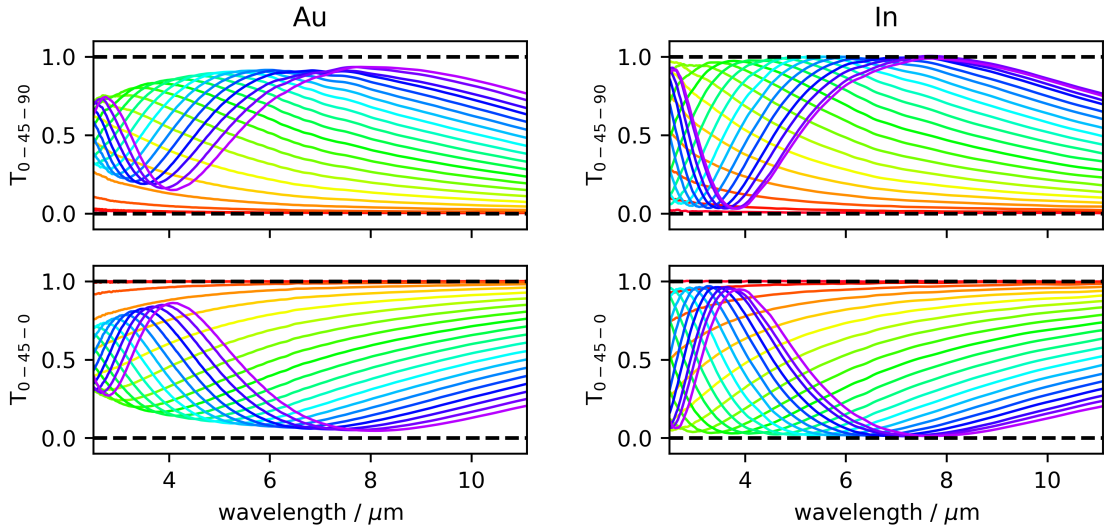

Figure 4.6: For both CZT samples, the transmission spectrum of light through a crossed- and parallel-polarizer system, at a range of applied voltages (0 kV in red progressing to 5 kV in violet) is shown in the top and bottom panel, respectively, normalized to the spectrum through parallel polarizers with no applied voltage to the crystal. The CZT optical axis is at 45° relative to the front polarizer. The deviation of the maxima and minima from 1 and 0 can be attributed to depolarization of the incident light as it passes through the CZT sample.

half-wave retardation is achieved, and a transmittance of unity when a full-wave retardation is achieved.

It can be seen that while the data does show maxima and minima when a high enough voltage is applied, the maxima never achieve unity and the minima never achieve 0. This can be attributed to depolarization. Any unpolarized portion of the light emerging from the sample will transmit exactly 50% of its intensity through the back polarizer regardless of the polarizer's azimuth. Thus in the case of the crossed-polarizer configuration at a half-wave retardation, all of the polarized portion of the light will get through, but 50% of the depolarized light will be blocked by the analyzer, so the transmittance cannot be unity. Similarly, in the parallel-polarizer configuration at half-wave retardation, all of the polarized portion of the light will be blocked by the back polarizer, but 50% of the depolarized portion of the light will be transmitted, so the transmittance cannot be 0. The amount of deviation from 1 and from 0 is directly related to the amount of the light that is

depolarized, and the same theories apply to full-wave and one-and-a-half wave retardation as seen at shorter wavelengths with higher applied voltage. If we follow the position of the half-wave maximum in the crossed-polarizer experiment, we can see that the amount of depolarization decreases as the maximum moves to higher voltages. This is in keeping with the degree of polarization plot in Fig. 4.4.

Depolarization is often seen in electro-optic materials, with the phenomenon usually explained as being caused by isotropic scattering. In order to investigate whether the depolarization seen is isotropic or anisotropic, the same crossed-polarizer experiment was performed, but with the incident light parallel to the sample's optical axis. The results with increasing applied voltage can be seen in Fig. 4.7, and there is negligible increase in the transmittance. Any depolarized portion of the light resulting from transmission through the sample would see 50% of its intensity passed through the back polarizer, so it seems based on this test, and the fact that the increase in transmittance is negligible, that no depolarization occurs for this configuration. The very small baseline transmittance can be explained here by the inherent static strain on the sample causing a very small birefringence, and the small increase in transmission could be a result in a fraction of a degree error in azimuthal alignment. The depolarization appears to be completely anisotropic- that is to say, dependent on the incident light polarization state.

To determine whether the depolarization could be caused by scattering, the transmittance of the sample itself was tested with no back polarizer. Light scattering should cause an overall decrease in the intensity of the light which gets through to the detector, as any light scattered would only have a small chance of continuing on its initial trajectory. The measurement was performed with incident light both parallel to, and 45° rotated with respect to, the optical axis of the crystal. Interestingly, the only dependence of transmittance on applied voltage that was observed was in the parallel configuration, which is where no depolarization is seen. In that experiment, there is a very small drop in transmitted intensity which coincides with the threshold where depolarization is seen to

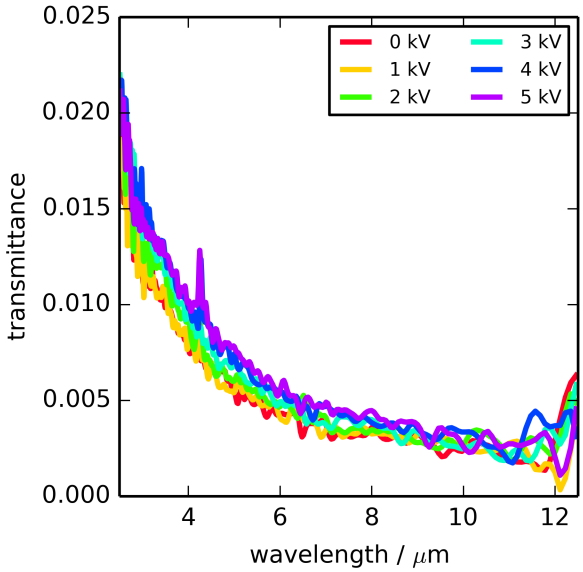

Figure 4.7: Transmittance of light through the crystal in a 45-45-135 configuration. Depolarization here would result in a proportional increase in transmitted intensity, but a negligible amount is seen as the voltage is ramped up to 5 kV.

develop in Fig. 4.4. In the configuration where depolarization is observed, there is no apparent dependence of transmittance on applied voltage, which leads to the conclusion that scattering is not responsible for the depolarization.

In order to further test this hypothesis, the transmittance through the crossed-polarizer system was measured at three different locations on the crystal, with the 'top' spot closest to the top electrode, and the 'bottom' spot closer to the bottom electrode face on the crystal. As can be seen in Fig. 4.9, the retardation does definitely increase towards the top electrode. In addition, because these measurements were taken with a more restricted beam spot size using an iris, a narrower distribution of retardations is measured at each spot, and the divergence of the maxima from 1 and the minimum from 0 is less if compared to Fig. 4.6.

Finally, we image the retardation in the crystal in a qualitative sense, and compare it to that of the indium sample, which shows virtually no depolarization. The transmission of all wavelengths through the crystal between parallel polarizers is used to image the clear aperture of the crystal, and this image is used as the background in order to image the

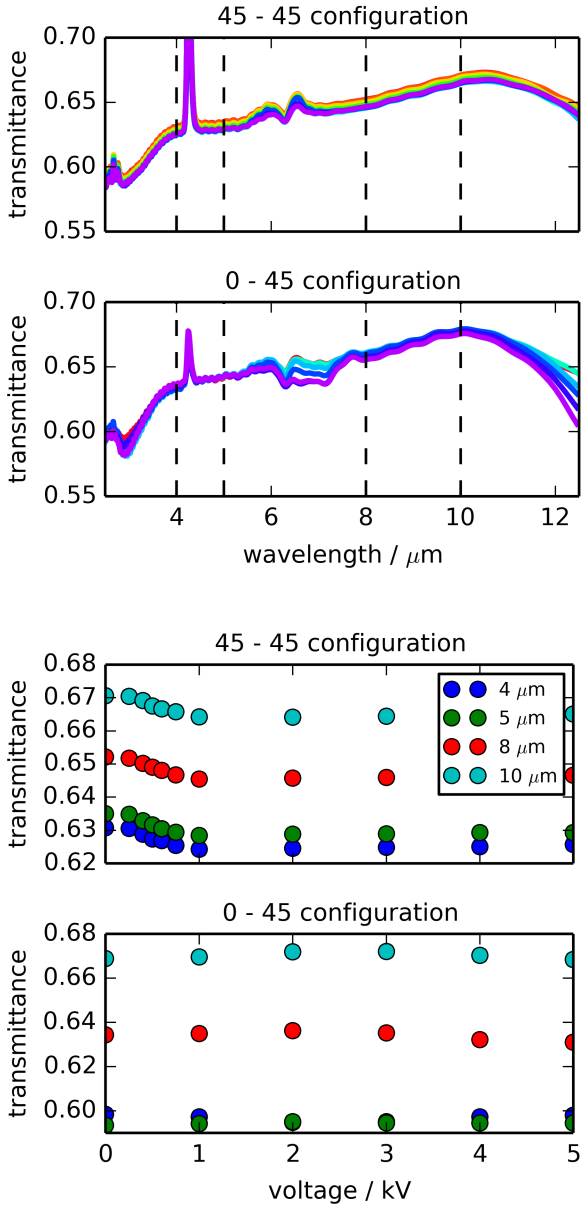

Figure 4.8: The raw transmittance of light through the crystal as a function of voltage (0 kV in red progressing to 5 kV in violet) for two incident polarization states. With incident light oriented parallel to the electro-optic optical axis, we see a small decrease in transmission which coincides with the drop in degree of polarization. However, this is not seen in the case of incident light oriented 45° off the optical axis, which is the application configuration. Overall, there seems to be very little light intensity lost to scattering, if any. Wavelengths to focus on in the bottom two panels were selected so as to avoid the CO_2 and water absorptions, which cause erratic data as the conditions vary within the experimental setup.

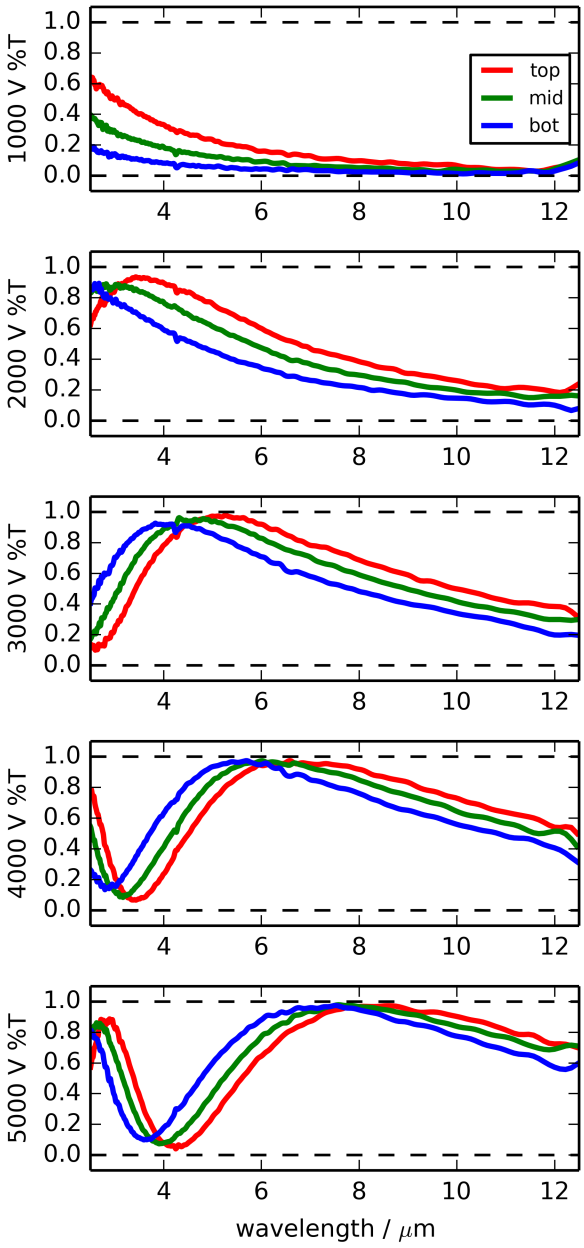

Figure 4.9: At five different voltages, the transmittance spectrum of the crossed-polarizer system is measured at three different locations in the crystal cross-section. The retardation increases from the bottom to the top of the crystal.

retardation, and thereby the electric field. A voltage difference of 1 kV is applied across the crystal, at which I can be sure that all wavelengths and all locations on the crystal are below a half-wave retardation, and the transmission through the crossed-polarizer system is mapped around the clear aperture defined by the previous experiment. The transmittance values in this setup are divided by this background in order to eliminate any effects of beam clipping along the edges of the crystal. The image obtained in Fig. 4.10 shows the retardation in the crystal decreasing from one electrode to the other. It is worth noting that the precise shapes of the clear apertures are insignificant, as for each crystal, the aperture was restricted beyond the edges of the crystal manually, in order to ensure that no light reached the detector without encountering the crystal. When the voltage is reversed, the image is also more or less reversed, with the gradient decreasing from the bottom electrode instead of the top electrode.

In the indium crystal, on the other hand, the retardation is more consistent from one electrode to the other. There is no clear gradient, and though there are regions of higher retardation and lower retardation throughout the crystal, they do not appear to follow a steady gradient from one electrode to the other. This can be seen as an expected result once the work function of the two electrode metals is taken into account. With a work function closer to that of the CZT, the indium-CZT interface should form a better ohmic contact, with a very small depletion region.

4.4 Modeling

Based on the depolarization in the gold-electrode sample being anisotropic, and not being caused by scattering, it was theorized that it is simply the result of the retardation of the sample not being consistent across the area of the crystal surface that the focused infrared beam analyzes. Mapping the transmission through a crossed-polarizer configuration supported this theory, and shows the electric field follows a gradient from the top electrode to the bottom, implying a non-linear voltage drop across the material, which allows a model

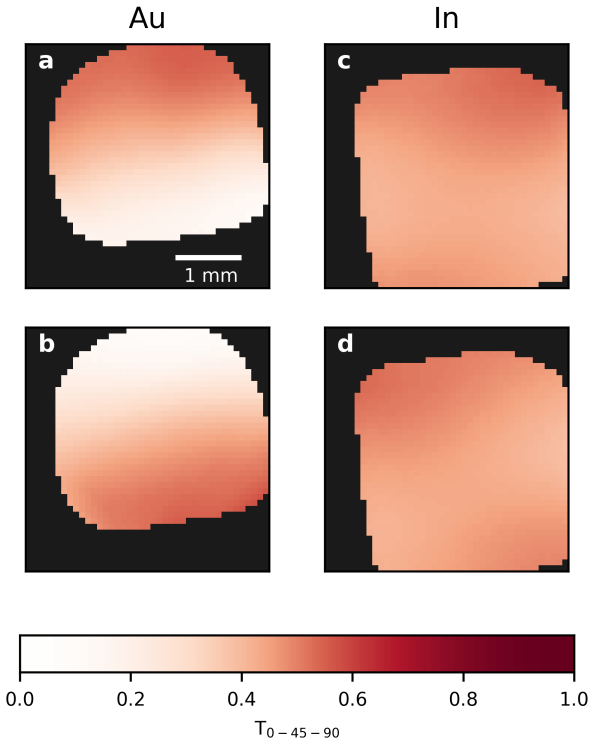

Figure 4.10: The electric field of each crystal imaged at 1 kV applied voltage. This is achieved in a qualitative sense in a 4 mm x 4 mm array, with bias applied in each direction on the top and bottom, respectively. The electric field is taken as the amount of light transmitted through a 0-45-90 configuration, normalized to the amount of light obtained through a 0-45-0 configuration at 0 applied voltage. Areas where no light reached the detector in the latter configuration are blacked out.

to be created to fit the experimental data. Doing so provides us with a complete, predictive characterization of the material properties.

A Gaussian distribution was determined as a good approximation of the distribution of retardations that the beam of IR light would encounter within the crystal. As I am theorizing that the electric field follows a decending, linear gradient from the top electrode to the bottom, the distribution of electro-optic coefficient is directly related to the distribution of distances from the bottom electrode. If the beam was of perfectly consistent intensity throughout the area of its circular beam spot, then I could use the equation of the width of a circle with respect to vertical position in order to approximate the distribution. However, because the beam's intensity tapers from the centre to the edges, more weight needs to be

given to the centre of the distribution, and therefore I expect that a normal distribution is a better representation of what is probably happening.

$$f(\delta) = \frac{1}{\sqrt{2\pi\sigma^2}} \exp\left[-\frac{(\delta - \bar{\delta})^2}{2\sigma^2}\right] \tag{4.2}$$

The CZT material is taken to be a waveplate with its optical axis at 45°. The retardation is not considered to be constant throughout, and thus I use the PDF, f, from Eq. 4.2 to generate a Mueller matrix which accounts for the distribution of retardations that the light will encounter.

$$\mathbf{M} = \int_{-\infty}^{\infty} \begin{bmatrix} 1 & 0 & 0 & 0 \\ 0 & \cos\delta & 0 & \sin\delta \\ 0 & 0 & 1 & 0 \\ 0 & -\sin\delta & 0 & \cos\delta \end{bmatrix} f(\delta) d\delta \tag{4.3}$$

As the expressions for the elements of this matrix can not be solved analytically, I instead have to evaluate guesses for the mean, $\bar{\delta}$, and the width, σ^2, of the distribution, by creating simulated data given the resulting Mueller matrix for the material. The two experiments are simulated using Mueller matrices of the constituent components, with consideration to the value being measured at the end. In either experiment, the initial Stokes vector created, $\mathbf{s_{in}}$, is horizontally polarized light, or $\begin{bmatrix} 1 & 1 & 0 & 0 \end{bmatrix}^T$. In the case of the Stokes polarimetry data, I simulate the Stokes elements which are measured by the polarimeter.

$$\mathbf{s}_{out} = M(\phi, 45°) \cdot \mathbf{s_{in}} \tag{4.4}$$

I can also simulate the intensity of light transmitted through the cross-polarizer setup in a similar manner. In this experiment, transmittance is measured, and not the Stokes vector. The signal intensity is measured after encountering a linear polarizer at 90° after the sample

$$P(90°) = \begin{bmatrix} 0.5 & -0.5 & 0 & 0 \\ -0.5 & 0.5 & 0 & 0 \\ 0 & 0 & 0 & 0 \\ 0 & 0 & 0 & \end{bmatrix} \tag{4.5}$$

and the transmittance can thus be calculated by calculating the resultant Stokes vector. Its first element, $\mathbf{s'_0}$, represents the transmittance.

$$\mathbf{s}' = P(90°) \cdot M(\phi, 45°) \cdot \mathbf{s_{in}} \tag{4.6}$$

In Fig. 4.11, both of these fits are shown in the lower two panels. In the middle panel, the crossed-polarizer data at 5 kV applied voltage is shown as black dots. In the lower panel, the Stokes vectors at 5 kV are shown along with the DOP. A model distribution for the retardation is shown in the top panel, and is used to produce the models in the lower two panels via the above method. The retardation is shown in units of μm, as we consider one value of retardation across all wavelengths. For instance, half-wave retardation at 4 μm would be quarter-wave retardation at 8 μm, and would be reported simply as 2 μm retardation. The assumption that retardation scales with wavelength is valid provided the properties of the material don't change significantly across our wavelength range, which is what is expected.

In determining the values of mean and width for the retardation model, the two parameters have different and separable effects on the simulated data. For the Stokes element curves, and for the crossed-polarizer data, a higher mean retardation means more rapidly oscillating behaviour in the data. For instance, in the s_3 curve on the bottom panel, the minimum around 5.5 μm will be shifted to the left or right in the figure if the mean retardation is increased or decreased, respectively. The width of the model distribution affects the value of the maxima and minima of oscillation. The most sensitive part of the data to this is the DOP curve, however, as the width of the distribution of retardations directly relates to how quickly DOP falls from 1 as the wavelengths get shorter. By optimizing these two parameters, simulated data can be created that seems to do a good job of predicting the depolarization across the wavelength spectrum, and fits the data from both experiments quite well. The fitting process is undergone for the data sets from every applied voltage in the range from 250 V to 5 kV.

The same exercise can be gone through with the indium-electrode sample. The fitting values for each voltage can be compared between the two crystals, and are shown in Fig. 4.12. I compensate for the slightly different dimensions of the two crystals by multiplying by the distance between electrodes, d, and dividing by the length of the

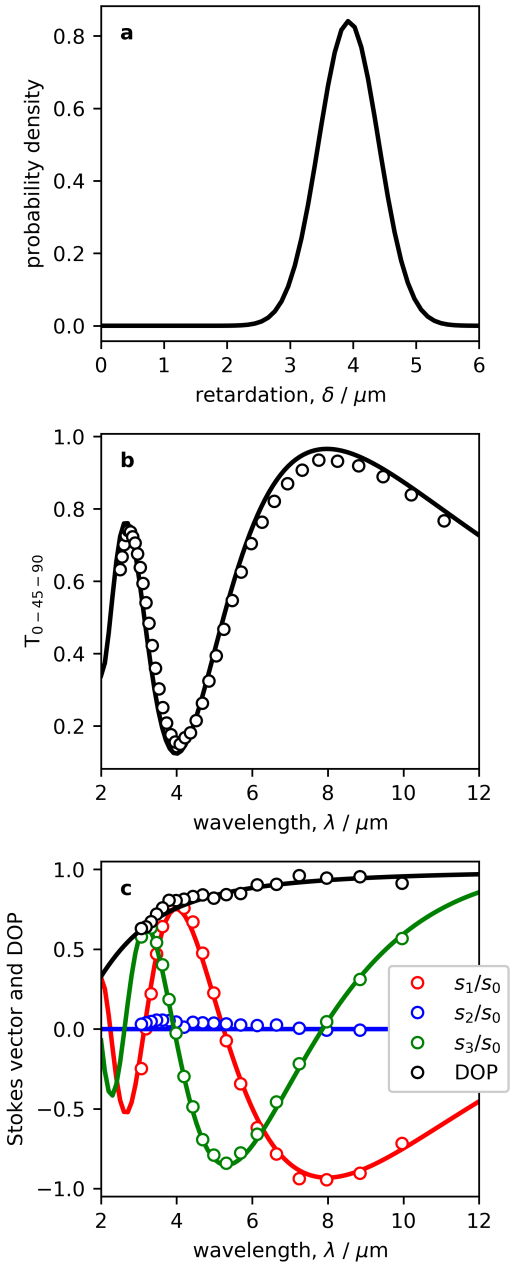

Figure 4.11: A depolarization model is shown for a crystal with 5 kV applied DC voltage, where depolarization results from a distribution of different retardations throughout the sample. The top panel shows the distribution of retardations being considered for the cross-section of the beam. The middle panel shows the model for the transmission in the 0-45-90 configuration given this distribution compared to the experimental data. The bottom panel shows the model (lines) for the resulting Stokes vector from a 0-45 configuration compared to the experimental data (points).

crystal, L. Mean retardations are not very different between the two materials. Provided that the most significant difference between the samples is the electrode, this shows that the CZT electro-optic properties are not overly different between the samples. Where a significant difference is seen is in the distribution widths, which is in-keeping with all of our observations to this point, and likely has a lot to do with the metal-CZT junction.

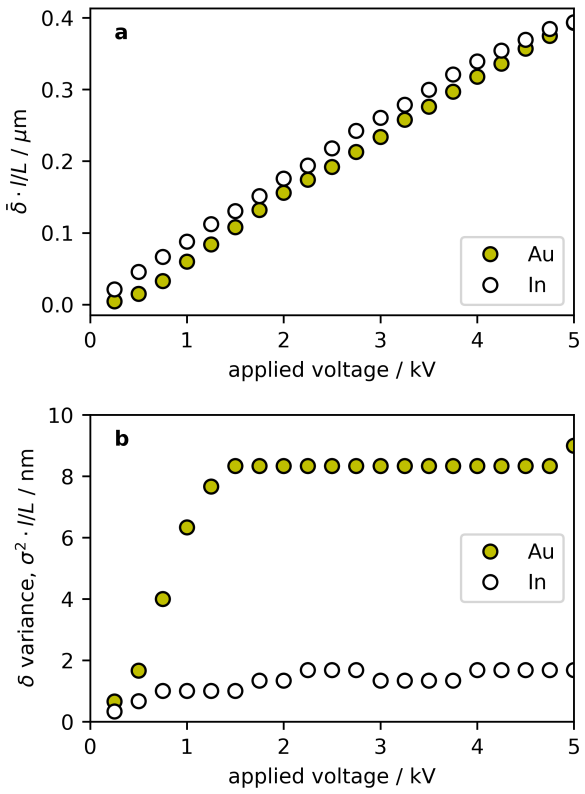

Figure 4.12: The mean electro-optic coefficient and the width of the distribution which best fit both crossed-polarizer and Stokes polarimeter data are shown for each crystal.

4.5 Discussion

Clearly, the compiled data indicate that CZT operates predictably as an electro-optic material with applied voltage up to 5 kV. In order to fully harness the property for most applications, however, the material needs to be capable of manipulating the polarization state light without depolarizing it. For instance, in operation as a light valve, an electro-

optic material at azimuthal orientation 45° from an incident linear polarizer applies half-wave retardation when a voltage is applied. A polarizer after the material, either parallel or perpendicular to the initial polarizer, transmits either all or none of the light. The voltage is typically applied in the form of a fast-switching pulse, and the system, together, creates a pulsed light source. However, depending on the configuration of the second polarizer in the system, having a portion of the transmitted light depolarized either brightens the dark state, or darkens the bright state. In either case, the best contrast between dark and bright state results from light always being fully polarized upon transmission through the electro-optic device.

One potential application that CZT could be suitable for would be as a variable retarder. A CZT electro-optic crystal could be calibrated such that any polarization state can be created for any wavelength in the mid-IR by setting the voltage applied to the crystal such that quarter-wave retardation is generated for the desired wavelength. However, there are few applications where slightly-depolarized light is desirable, and so it is very important that a variable retarder not reduce the degree of polarization of the light.

In my investigation of CZT's electro-optic properties, it seems very clear that the ability of the material to perform efficiently in applications such as the above depends heavily on the metal used for the electrodes to apply high voltage. I have only covered two electrode materials, but of course several other materials could be used. The results with gold and indium make sense with the expected trend, as set out in the introduction. The ideal scenario with a perfect ohmic contact between the electrode and the CZT material would create a uniform electric field from one electrode to the other when high voltage is applied, and an ideal sample would show no variation in retardation across its cross-section, and therefore no depolarization. Gold's work function is such that a large Schottky barrier is created, and a depletion region extends far into the CZT sample. Instead of voltage dropping linearly from one electrode to the other, it drops quickly through the depletion region, and tapers off from there. As electric field is the derivative of voltage with respect

to distance, this means a relatively linear gradient of electric field through the material.

The initial aim of this investigation was to measure the r_{41} coefficient of CZT; however, given the inconsistent electric field seen in both materials, it does not seem that such a value can be elucidated from the data. A uniform electric field would have allowed the r_{41} to be calculated using the voltage and dimensions of the crystal as per Eq. 4.1, but in order to calculate it in the presence of a non-uniform field, the electric field would need to be directly measured. This presented a challenge as to how the crystals could be characterized, if not by their electro-optic coefficients.

By creating a model for experimental results using a normal distribution of retardations, I have created a means to compare the ability of an electro-optic device to function for applications. In the case of gold and indium, it can be seen that the electro-optic properties of the CZT are very similar, but due to the different metal contacts, indium is much closer to being a useful device which doesn't depolarize light. In fact, given the low amount of depolarization in this sample, for a sufficiently focused laser, negligible depolarization should be observed. However, this still presents the problem of the properties not being consistent in all locations, and therefore this presents calibration issues if attempting to use this sample for applications. If the metal-semiconductor junction properties could be further improved, the width of the distribution could be further reduced, until it becomes negligible, which would make for an ideal, useful device.

In comparing gold and indium as electrode choices, Fig. 4.10 shows that not only is the indium sample more consistent, the shape and type of the small inconsistency is very different. The gold sample shows a very clear gradient from one electrode to the other, while the smaller inconsistency in the indium sample takes a different shape, with a region of lesser electric field spanning from one corner to the other, and the image being reversed side-to-side upon changing the direction of the applied voltage. It is likely that the inconsistency in the electric field could be due to some factor other than the metal-semiconductor junction in the case of this sample. If so, for a different CZT sample with

indium electrodes, the electric field could be even more uniform with applied voltage.

The modeling is also useful as a predictive tool. The determined mean and width of the electro-optic coefficient at various voltages can be used to precisely predict the resultant polarization state and degree of polarization when light is transmitted through an electro-optic device which has been characterized in this manner.

4.6 Summary

I have used both Stokes polarimetry and a polarizer-based method of analysis to study the electro-optic properties and depolarization of two CZT electro-optic modulators, with gold and indium electrodes, respectively. The material displays a consistent Pockels effect in either case, but also depolarizes light in the crystal when gold electrodes are used due to the large Schottky barrier at the metal-semiconductor junction. Indium electrodes show a much more consistent electric field through the crystal, and thus allow more useful devices to be made.

Chapter 5

Electro-optic characterization of CZT with AC applied voltage

5.1 Introduction

In the previous chapter, I explored the electro-optic properties of two CZT electro-optic modulator crystals, each with different metal electrodes. The properties were measured with DC applied voltage, which explores the usability of the material as a variable retarder, among other things. Of the two, the indium-electrode crystal proves to be the more useful of the two, as the metal-semiconductor junction forms an ohmic contact. However, many electro-optic applications, such as fast-switching light valves, Q-switches, or polarization modulators, require a material to display the electro-optic property in response to an AC applied voltage. A comprehensive first exploration into the electro-optic properties of CZT must therefore include characterization of the material's response to AC voltage, and not just DC voltage.

There are a few concerns when moving from DC applied voltage to AC. One is that the material's response to a high-frequency voltage may not be able to match the rate at which the voltage is switching. This can occur due to opposing electric fields created within the material, which cause a phase lag between the electric field oscillation and the oscillation of optical properties which it induces. Secondly, all materials that possess the electro-optic effect also, by necessity, possess the piezoelectric effect, which means that as the material

has an AC voltage applied, it is mechanically deformed at that frequency as well. For some materials the extent of the deformation is significant, and for others it is quite small. As the frequency is increased, however, supposing the crystal is able to withstand the deformation, it may significantly change the electro-optic properties of the material compared to with a DC voltage. For this work, only low-frequency applied voltage was used due to instrument limitations.

5.2 Experimental

The sample being investigated in this work is a cadmium zinc telluride (CZT) electro-optic crystal, which is 52.5 mm long, and 5.3 mm in width and height. Two opposing long faces contain indium electrodes, with gold wires attached near one end on each electrode with silver conductive epoxy.

I will present two schemes for measuring the Pockels retardation of the crystal, using lock-in amplifiers at first, and an oscilloscope in the second scheme. Using the FTIR as the mid-infrared light source in step scan mode, I can analyze every wavelength together. The schematic of each instrumentation is shown in Fig. 5.1. A variable AC power supply, which can supply AC voltage up to 3.2 kV amplitude at 60 Hz, is used to apply voltage to the crystal.

The crystal's optical axis is oriented 45° with respect to the two polarizers, which are aligned horizontally. In the first measurement configuration attempted, a chopper precedes the first polarizer, and the signal from the detector is passed to lock-in amplifiers along with a reference frequency from the chopper and the power supply. The lock-in amplifiers analyze the chopper frequency component of the signal, as well as the fundamental frequency (60 Hz) component and second harmonic (120 Hz) frequency component.

CZT possesses the Pockels effect, which means it is expected that the retardation of light through the sample will be proportional to the voltage being applied. The natural expectation, therefore, is that if the voltage being applied to the crystal is a sinusoidal

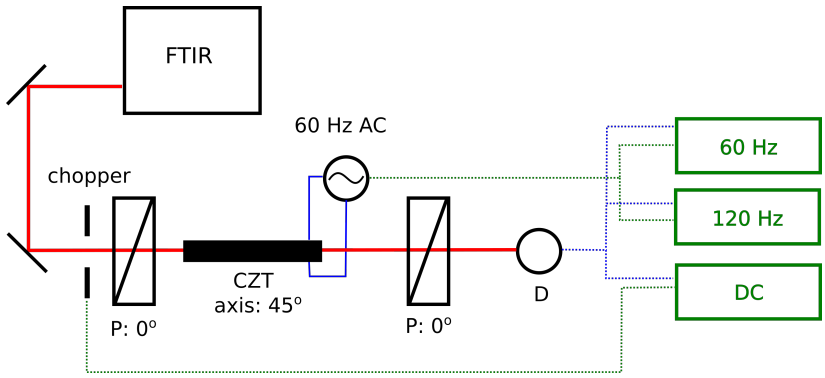

Figure 5.1: Schematic of the instrumentation for measuring the amplitude of the CZT sample's retardation, and its static retardation. Incident is chopped and polarized at 0°, and after encountering the sample with optical axis at 45°, passes through another polarizer at 0°. The signal at the detector is passed to three lock-in amplifiers, which demodulate the signal at three frequencies of interest, which correspond to the material properties.

function, then so will be the resultant retardation, with some amplitude, A, and static retardation, δ°, that can be measured. The voltage being applied to the crystal can be measured by the oscilloscope, which provides insight into whether the voltage has an ideal sinusoidal shape. This is shown in Fig. 5.2.

$$\delta_{CZT} = A\cos(2\pi f t) + \delta^\circ \tag{5.1}$$

When AC high voltage is applied to the crystal, the retardation varies with time, thus causing the transmission through the second polarizer to oscillate. For instance, in an instance where the crystal induces half-wave retardation for one wavelength, none of that light will reach the detector. The shape of the intensity waveform generated at the detector allows me to determine the retardation behaviour of the sample.

In an initial measurement scheme, I follow exactly the methodology used to characterize and calibrate the properties of a photo-elastic modulator. The polarization state which arrives at the detector depends on the behaviour of the material's retardation, which is assumed to follow Eq. 5.1. With the amplitude and static retardation needing to be fit, the spectra of the intensity components can be modeled using Mueller matrix algebra. Fig. 5.3 shows the fit of modeled data to experimental data for a 37 kHz PEM at two different

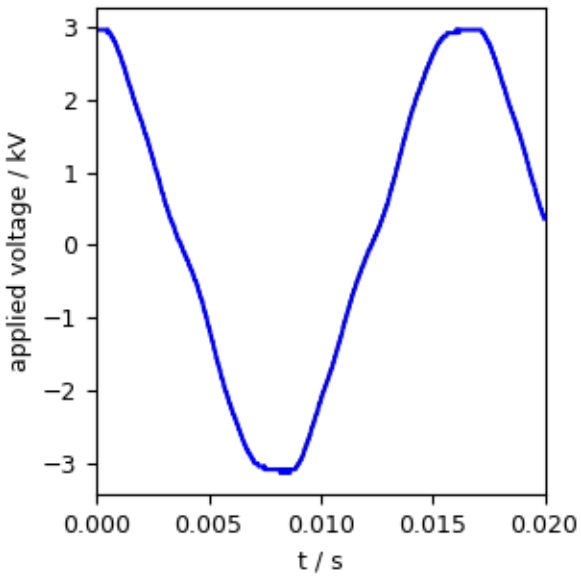

Figure 5.2: The oscilloscope trace of the reference voltage from the AC power supply. Deviation from ideal sinusoidal shape can clearly be seen.

driving voltages, and it can be seen that the model agrees well with the data.

$$\mathbf{s}' = P(0^\circ)M(\delta_{CZT}, 45^\circ)\mathbf{s} \tag{5.2}$$

In this equation, $\mathbf{s}$, the initial polarization state, is horizontal light, with a Stokes vector of $\begin{bmatrix} 1 & 1 & 0 & 0 \end{bmatrix}^T$. The MCT detector is, of course, only capable of detecting the intensity of the light, which is represented by the first element of $\mathbf{s}'$, or $\mathbf{s_0'}$.

$$\mathbf{s_0'} = \frac{1}{2}\mathbf{s_0}\left(1 + \cos(A\cos(2\pi f t) + \delta^\circ)\right) \tag{5.3}$$

I can determine different frequency components of the signal using Fourier analysis. Solving for the component of the signal of the second-harmonic frequency of the applied voltage, or I_{120}, is done by multiplying the intensity expression by a cosine of the frequency

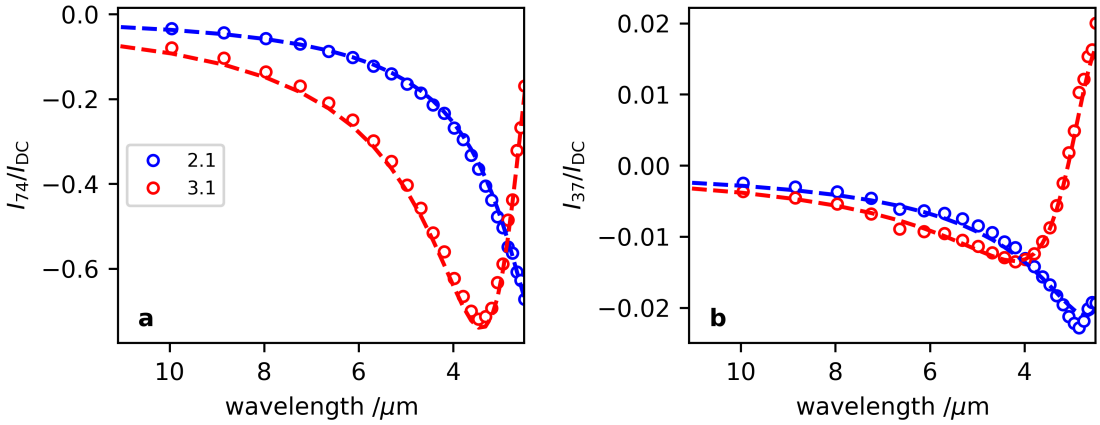

Figure 5.3: Conventional calibration of a 37 kHz photo-elastic modulator using a scheme involving a polarizer and analyzer at 0° on either side of the PEM with its optical axis at 45°, at two different driving voltages. The second-harmonic and fundamental frequency components of the intensity can be fit to a model in order to determine the amplitude of the PEM's retardation as well as its static retardation. The legend refers to the driving voltage setting, where the PEM is set to 2.1 rad or 3.1 rad retardation amplitude at 3000 cm^{-1}. The exact voltage supplied to the PEM is unknown.

of interest, and integrating over a period.

$$\begin{aligned} I_{120} &= \frac{1}{\pi}\int_{-\pi}^{\pi}\frac{1}{2}\mathbf{s_0}\left(1+\cos(A\cos(2\pi(60Hz)t)+\delta^\circ)\right)\cos(4\pi(60Hz)t)\delta t \\ &= -\cos\delta^\circ J_2(A)\mathbf{s_0} \end{aligned} \tag{5.4}$$

$$\begin{aligned} I_{60} &= \frac{1}{\pi}\int_{-\pi}^{\pi}\frac{1}{2}\mathbf{s_0}\left(1+\cos(A\cos(2\pi(60Hz)t)+\delta^\circ)\right)\cos(2\pi(60Hz)t)\delta t \\ &= -\sin\delta^\circ J_1(A)\mathbf{s_0} \end{aligned} \tag{5.5}$$

$$\begin{aligned} I_{\mathrm{DC}} &= \frac{1}{2\pi}\int_{-\pi}^{\pi}\frac{1}{2}\mathbf{s_0}\left(1+\cos(A\cos(2\pi(60Hz)t)+\delta^\circ)\right)\delta t \\ &= (1+\cos\delta^\circ J_0(A))\mathbf{s_0} \end{aligned} \tag{5.6}$$

If each frequency component pertaining to the voltage frequency is divided by the DC component, the variable of initial light intensity, $\mathbf{s_0}$, which depends on wavelength, can be

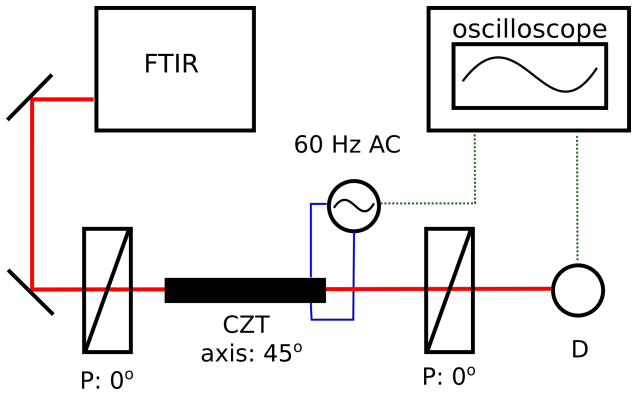

Figure 5.4: Schematic of the instrumentation used to precisely visualize the shape of the waveform at the detector. The optical path is the same as in Fig. 5.1, but with no chopper, and no lock-in amplifiers. The signal is passed to an oscilloscope, which is triggered by the reference voltage from the AC high-voltage power supply.

eliminated. Thus the beam spectrum of the source won't affect the shape of the results.

$$\frac{I_{120}}{I_{\mathrm{DC}}} = \frac{-\cos\delta^{\circ} J_2(A)}{1+\cos\delta^{\circ} J_0(A)} \tag{5.7}$$

$$\frac{I_{60}}{I_{\mathrm{DC}}} = \frac{-\sin\delta^{\circ} J_1(A)}{1+\cos\delta^{\circ} J_0(A)} \tag{5.8}$$

In the experiment, at each FTIR step, the signal is passed to three lock-in amplifiers, which measure each of these three values. After stepping through all of the mirror steps, I end up with three interferograms. The intensity spectra are determined by Fourier transforming the interferograms which are obtained as raw data, and then I divide the other two spectra by the DC spectrum. Unfortunately, it is not possible to analytically solve for the two desired values, A and δ°. I therefore fit my I_{120}/I_{DC} and I_{60}/I_{DC} spectra to determine the best values for amplitude and static retardation of the material. Here, I am aided by the multi-wavelength nature of the experiment. For one wavelength, I would get just one value from each lock-in amplifier, and these values do not have high sensitivity to small changes in amplitude and static retardation. By being able to fit a large spectrum of wavelengths, I can fit an overall trend, which allows me to avoid being too influenced by noise fluctuation in the data, and get a result I can have more confidence in.

In a second and new method for analyzing the AC behaviour of the crystal in our wavelength range, I look at the raw signal directly using an oscilloscope. The optical

configuration is identical, and only the signal processing is different. The FTIR in step scan mode steps through mirror positions, and at each one, an oscilloscope trace is recorded instead of analyzing the signal with lock-in amplifiers. A reference voltage is relayed to the oscilloscope to act as a trigger, which ensures that each FTIR-step's time-trace is aligned with respect to the applied voltage. After 256 such steps, the data set is complete.

The data can be Fourier transformed along the FTIR step axis, such that for each time step in an oscilloscope trace, a frequency-domain spectrum of transmittance is obtained, each of which can be divided by the reference spectrum collected at no applied voltage. Thus, in taking a slice of data from the 2-D plot, I end up either being able to see the transmission spectrum at a certain point of time, or the oscilloscope trace for a particular wavelength.

5.3 Results

My initial attempt at characterizing CZT under 60 Hz AC voltage was to use lock-in amplifiers and characterize the oscillating retardation in the same way that a photo-elastic modulator may be characterized; that is, with the CZT material between two parallel polarizers with its optical axis 45° off from the polarizers, the second-harmonic frequency (120 Hz), fundamental frequency (60 Hz) and DC components on the signal are measured with lock-in amplifiers. These three data points are generally sufficient to report the amplitude and mean of the oscillating retardation of the material. However, this assumes a simple and ideal behaviour of the material being measured. In the case of a photo-elastic modulator, retardation is brought about through mechanical deformation of the material at its resonant frequency, which is a highly reliable effect. Any asymmetry in this process would strain the crystal, and at high-frequency, likely cause damage to it. Thus with a PEM, one can be reasonably certain that the retardation oscillation is a tidy, sinusoidal function with time, which is corroborated by the very close fit of the data to the model in Fig. 5.3.

In the case of CZT, however, I found that a precise fit to the data could not be created,

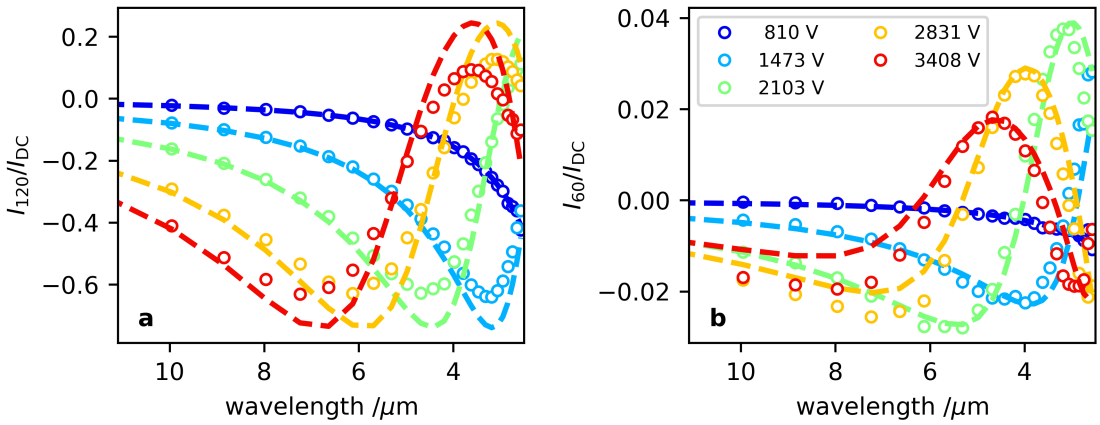

Figure 5.5: Attempts to fit the normalized second-harmonic and fundamental frequency component intensity spectra with an amplitude and static retardation are insufficient at a variety of voltages.

which led me to believe that, somehow, the shape of the oscillation of retardation in the material was not ideal. The results of this attempt can be seen in Fig. 5.5. In each case, the fit values are the slopes of the change in amplitude and static retardation with wavelength. This is because, just as in the case of retardation itself, the amplitude is greater for shorter wavelengths. These slope values are optimized by a scoring method, with the best values producing the simulated, dashed lines of Fig. 5.5. The experimental data for second harmonic can't meet the maximum and minimum values from the model so long as the fit to the fundamental frequency component is good. Either I fit the left panel well at the expense of the right panel, or vice versa.

Given that the experimental data does not seem to match to the simplistic model of an oscillating retardation around zero, I used an oscilloscope to look directly at the shape of the time-variant signal intensity in real time, in order to see why its behaviour differs from that of a photo-elastic modulator. One possible reason, of course, is the deviation of the supplied voltage from true sinusoidal shape; however, while this would introduce other frequency components into the intensity waveform, I was interested to see if behaviour was otherwise as expected.

With the configuration in the previous section, I collected the oscilloscope traces at each FTIR-step, and the data are shown in Fig. 5.6d. After Fourier transforming at each time step, the data are shown in Fig. 5.6e. An example of the data being fitted is shown in Fig. 5.6f, for 2762 cm^{-1}. Interestingly, when the voltage reaches its minimum near -3 kV, it shows much higher retardation than when it achieves a maximum near $+3$ kV. This indicates asymmetric behaviour of the crystal, with one behaviour seen for negative voltage, and another behaviour seen for positive voltage.If the electric field is uniform, then throughout the crystal, the electric field is $E = V/L$. However, as there is asymmetric behaviour between positive and negative voltages, the electric field created within the crystal cannot be uniform, and within the region of the crystal that is analyzed by the light, I consider the electric field to be piece-wise defined by the voltage and further coefficients a_+ and a_-, depending on whether the voltage is positive or negative.

$$E(x,y) = \begin{cases} a_+(x,y) \cdot V/L, & \text{if } V \geq 0 \\ a_-(x,y) \cdot V/L, & \text{if } V < 0 \end{cases} \tag{5.9}$$

where a_+ and a_- are position dependent parameters. Thus based on Eq. 4.1,

$$\delta_{\text{CZT}} = \begin{cases} a_+ \cdot \dfrac{2\pi n_0^3 r_{41} \ell V}{\lambda L}, & \text{if } V \geq 0 \\ \\ a_- \cdot \dfrac{2\pi n_0^3 r_{41} \ell V}{\lambda L}, & \text{if } V < 0. \end{cases} \tag{5.10}$$

Retardation must then be expressed as a function of time. Given that the voltage is a simple sinusoidal function $V = V_{\max} \cos \omega t$, retardation is predicted to be

$$\delta^+_{\text{CZT}} = a_+ \cdot \frac{2\pi n_0^3 r_{41} \ell V_{\max} \cos \omega t}{\lambda L} \tag{5.11a}$$

for $2n\pi/\omega \leq t \leq (2n+1)\pi/\omega$, and

$$\delta^-_{\text{CZT}} = a_- \cdot \frac{2\pi n_0^3 r_{41} \ell V_{\max} \cos \omega t}{\lambda L} \tag{5.11b}$$

for $(2n-1)\pi/\omega < t < 2n\pi/\omega$, and integer values of n. Using the same definition of two cases as in Eq. 5.11, the intensity at the detector at time t is

$$s'_0 = \frac{1}{2} s_0 (1 + \cos \delta^{\pm}_{\text{CZT}}). \tag{5.12}$$

with $\delta^{\pm}_{\mathrm{CZT}}$ piece-wise defined in the two cases defined in Eq. 5.11. By dividing the intensity data by a background of maximum transmission through the crystal, I obtain transmittance, which is bounded between zero and unity. Using this model, optimize a_1 and a_2 can be optimized to fit the entire data set in Fig. 5.6. The data in the bottom panel shows a fit to the oscilloscope trace at 2762 cm^{-1}. This simulated data for transmittance uses the intensity function described in Eq. 5.11 with optimized values of a_1 and a_2.

This method is applicable to characterizing the AC optical behaviour of any type of device or material. In the left column of Fig. 5.6, it is applied to analyze the photo-elastic behaviour of a 37 kHz photo-elastic modulator. The PEM had been previously calibrated using the lock-in amplifier method (as seen in Fig. 5.3), and it was determined that, at 2763 cm^{-1}, with its applied voltage set to provide 3.1 rad amplitude at 3000 cm^{-1}, its retardation can be described by $\delta = A \cdot \cos(2\pi\omega t) + \delta^0$ where the amplitude, A is 3.26 rad, and the static retardation, δ^0, is 0.0306. This equation for δ is thus used to create a model for the transmittance through the analyzer, and the model agrees very well with the data in Fig. 5.6c.

5.4 Discussion

In the previous chapter, I reported the DC electro-optic properties of the indium-electrode CZT sample used in this work. Part of that analysis involved mapping the electric field with voltage applied from the top electrode, and the bottom electrode. In the case of this sample, some inhomogeneity could be seen. It is possible that such inhomogeneity of the electro-optic properties within the material can be revealed by the shape of the oscilloscope trace for one wavelength. If, for instance, the beam was centred around a region in the crystal which experiences a higher electric field when voltage is applied on one electrode as opposed to the other, then the results that we see make sense: when the voltage is positive, the region of the crystal that we are analyzing experiences a certain maximum electric field, and thus reaches a certain retardation, and when the voltage is negative, it experiences a

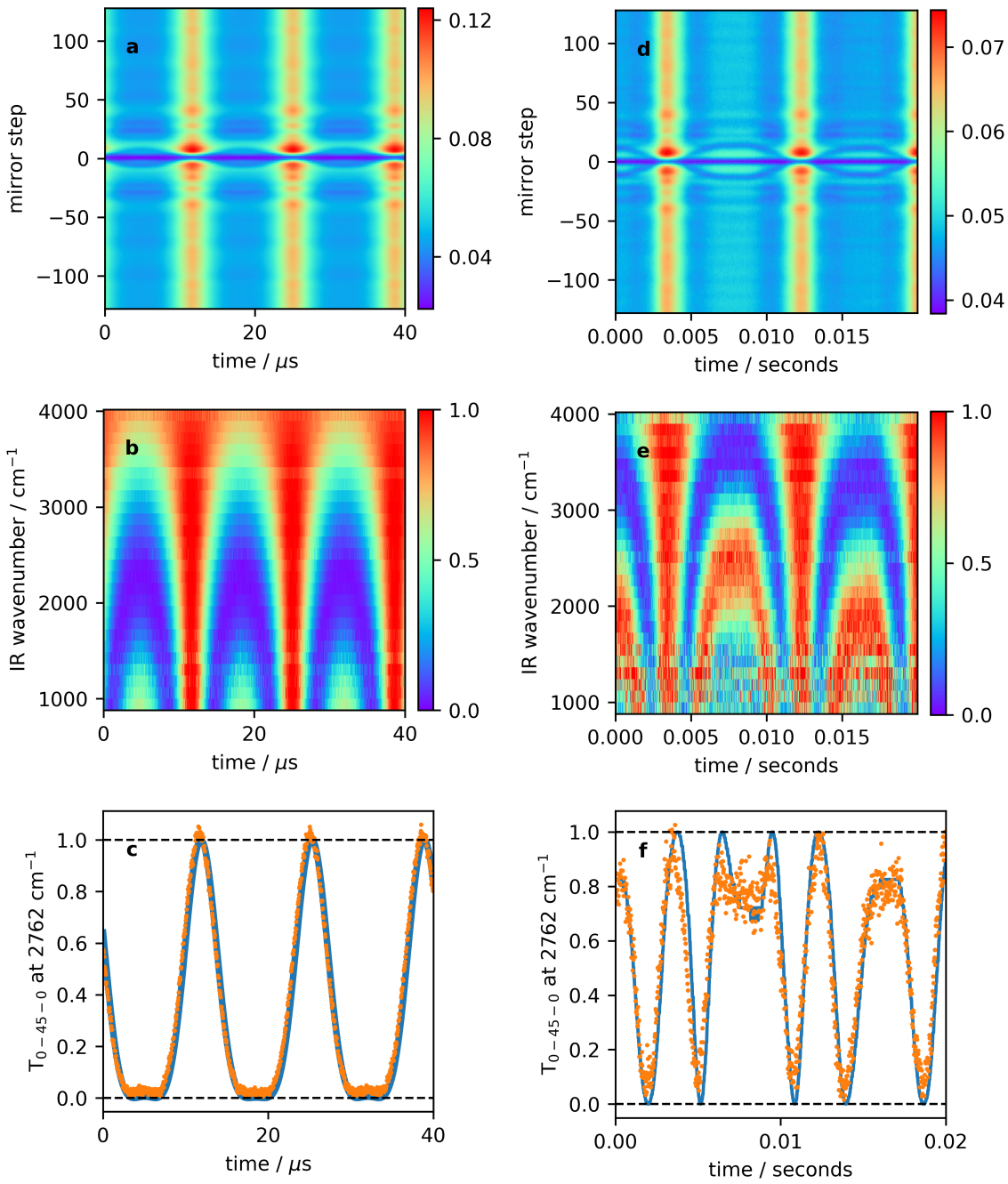

Figure 5.6: Oscillocope visualization of the response of the optical properties of a ZnSe PEM (left column) and a CZT electro-optic crystal (right column) to applied AC voltage. Raw data is shown in the top row, and is Fourier transformed along the FTIR-step axis to produce the middle row. The data slice at 2763 cm^{-1}, (bottom row, orange) is consistent with a model (blue) in either case, though the method of developing the model is more complicated for CZT.

different, larger maximum electric field, reaching a peak of greater retardation.

Regarding the concerns as to whether the material is suitable for AC applied voltage, the shape of the fit to the data in Fig. 5.6 is very encouraging, as it indicates that, at least considering either positive or negative values only, the material does seem to display retardation linearly proportional to the applied voltage in real time. In principle, the divergence in behaviour with the polarity of the applied voltage does not make a crystal unsuitable for applications involving AC applied voltage, as in many cases, the applied voltage could be pulsed, or a square wave, in which case the voltage is either at a given value (either positive or negative), or at zero.

The methodology developed to provide a more detailed analysis of the material's response to high voltage has promise to be useful for characterizing inhomogeneity in optical device materials. Whether the material in question is electro-optic, photo-elastic, or has any other capacity for modulation of optical properties, a model can be created, and deviation from expected behaviour can be measured using an oscilloscope. In the case of the electro-optic properties of CZT, I found the material to have different behaviour for positive voltage than negative voltage, and postulated that inhomogeneity could be the cause of this phenomenon. With other investigations, I would speculate that this approach could be similarly useful.

This investigation was performed with a focused broadband IR beam as the source, but for most application and investigations, a laser is used. Optical investigation techniques are, in general, easier with a single wavelength, and usually the device is envisioned as being practical especially for a discrete source. However, based on on the proposed theory of what causes the divergence in behaviour with positive and negative voltage, it's worth considering that this particular phenomenon would likely be exacerbated by a reduction in the beam spot size, given that a wider beam can allow inhomogeneities within the material to average out.

Especially with a discrete source and the lack of need to step through FTIR mirror

positions, this would be a technique that lends itself to imaging, and perhaps could be useful for locating defects or localized strain in a material.

5.5 Conclusion

CZT shows good promise for use as an electro-optic modulator with AC applied voltage, but these results are very preliminary. A full characterization of the material under AC applied voltage would need to involve much higher frequencies. A new methodology was developed to assess inhomogeneity of a material's response to applied voltage, and led to a more complete understanding of the response of CZT to AC high voltage.

Chapter 6

Summary and Conclusions

6.1 Summary of research

The mid-infrared region represents a challenging wavelength region for optical devices and techniques, due to a scarcity of available optical components, and sources which are generally not as intense as in other spectral regions. In this dissertation work, a new material for mid-infrared optical devices is characterized, and instrumental methods are explored for mid-IR polarization state measurement, and electro-optic device characterization. A novel Stokes polarimeter for broadband measurement in the mid-IR is presented. By utilizing an FTIR, the signal-to-noise ratio limitation of measuring single wavelengths from a dispersive source is avoided. This new optical technique was shown to accurately measure linearly polarized light, and was also used to experimentally determine the wavelength-dependent refractive index difference of quartz towards the long-wavelength limit of its transmission range, beyond where this property has been documented.

The electro-optic properties of a cadmium zinc telluride for the infrared have been studied and observations reported with gold and indium electrodes. The goal at the outset of the project was to use Stokes polarimetry to measure the r_{41} electro-optic coefficient of the material across the wavelength spectrum, and assess the material's applicability to electro-optic applications with both DC and AC applied voltage; however, neither sample showed consistent enough electric field throughout its cross-section to definitively report this value. In the case of gold electrodes, the electric field through the material was a consistent

gradient from one electrode to the other. Instead, I was able to investigate the ramifications of electrode metal choice, while also evaluating the electro-optic properties of the material using a modelling approach which accounts for and quantitatively assesses the distribution of retardations within the material when DC voltage is applied. AC investigations were limited to low frequency applied voltage, which allowed characterization of the material's response to a changing voltage to an extent. For most AC applications, however, frequencies up to hundreds of kilohertz are generally sought, and with higher frequency, the material's response could be very different due to piezoelectric deformation of the crystal and material defects.

A new methodology for characterizing the material's response to an AC applied voltage was conceived using an oscilloscope and an FTIR spectrometer. This method allows for the observation of asymmetric response to an AC voltage which can be caused by inconsistencies in the material across its interface, and could be applicable to other such systems where the consistency of optical response of a material is of interest.

6.2 Recommendations for further work

When the Stokes polarimeter for broadband measurement of the polarization state across the IR was designed, one of the potential applications sought was to harness the power of the IR spectral region and use it to study the orientation of vibrational bands. This work was never pursued within this dissertation, but the possibility still exists. For materials which have a characteristic vibrational band due to a bond which becomes macroscopically aligned in the material, linear dichroism would exist in the material, as these bonds preferentially absorb one linear polarization state more than others. The Stokes polarimeter described in this manuscript would be an ideal tool for investigating this, as the Stokes vector would be wavelength-dependent, which utilizes the broadband nature of the technique.

An alternative configuration of the instrument also exists, similar to that which can

be found in commercial mid-IR elliipsometers. The design of a Stokes polarimeter described in this dissertation uses an FTIR spectrometer in step-scan while allowing the polarization modulator optics to modulate light continuously at high-frequency. The alternative configuration would be to allow the FTIR to run continuously, while moving polarization modulation optics in steps. Either a retarder of fixed retardation, most favourably an achromatic retarder such as a rhomb system, could have its azimuthal angle changed in steps, or a variable retarder, potentially CZT itself, could have its retardation stepped. Having two such optics in succession with different azimuths is important, as it is in the polarimeter described in this thesis, as it allows for sensitivity to more polarization states. With four configurations chosen carefully, the Stokes vector could be measured. This arrangement would be faster for data collection than the Stokes polarimeter in this dissertation, and would allow for many averages to be taken at each configuration, leading to more precise results.

Once a consistent, single-valued electric field can be generated throughout the crystal, the r_{41} electro-optic coefficient can be measured and reported. With possible high-frequency applications such as Q-switching, it would be of interest to continue the characterization of the material with higher-frequency AC applied voltage, especially considering that high frequency can present issues with electro-optic devices due to piezo-electric response of the material.

Appendix A

Further details of derivation of Stokes vector expressions

To begin with, the following two variations of the Jacobi-Anger expansions are employed throughout.

$$\cos\left(a\cos x\right) = J_0(a) + 2\sum_{n=1}^{\infty}(-1)^n J_{2n}(a)\cos\left(2nx\right) \tag{A.1a}$$

$$\sin\left(a\cos x\right) = 2\sum_{n=0}^{\infty}(-1)^n J_{2n+1}(a)\cos\left((2n+1)x\right) \tag{A.1b}$$

where the sums on the right side are convergent due to the bounds being restricted on Bessel functions of the first kind as the degree is increased. These allow me to solve certain integrals with nested sinusoidal terms, with the understanding that every term contained by the summations in A.1a and A.1b will be zero under integration over an integer number of periods. As set out in Section 3.1.2, frequencies ω_i will always be considered to be integer-valued, with the period of integration defined from $-\pi$ to π, without loss of generality.

$$\begin{aligned}\int_{-\pi}^{\pi}\cos\left(Acos(\omega t)\right)dt &= \int_{-\pi}^{\pi}\left[J_0(A) + 2\sum_{n=1}^{\infty}(-1)^n J_{2n}(A)\cos\left(2n\omega t\right)\right]dt \\ &= \int_{-\pi}^{\pi} J_0(A)dt + 2\sum_{n=1}^{\infty}\left[(-1)^n J_{2n}(A)\cancelto{0}{\int_{-\pi}^{\pi}\cos\left(2n\omega t\right)dt}\right] \\ &= 2\pi J_0(A)\end{aligned} \tag{A.2}$$

$$\int_{-\pi}^{\pi} \sin\left(Acos(\omega t)\right)dt = \int_{-\pi}^{\pi} \left[2\sum_{n=0}^{\infty}(-1)^n J_{2n+1}(A)\cos\left((2n+1)\omega t\right)\right]dt$$

$$= 2\sum_{n=0}^{\infty}\left[(-1)^n J_{2n+1}(A)\cancelto{0}{\int_{-\pi}^{\pi}\cos\left((2n+1)\omega t\right)dt}\right]$$

$$= 0 \tag{A.3}$$

In addition, cosine laws and sine laws allow me to deal with the static retardation terms which complicate the cosine and sine terms in the expression.

$$\begin{aligned}&\cos\left(A\cos\left(\omega t\right)+\delta^0\right)\\ &=\cos\left(A\cos\left(\omega t\right)\right)\cos\left(\delta^0\right)-\sin\left(A\cos\left(\omega t\right)\right)\sin\left(\delta^0\right)\end{aligned} \tag{A.4a}$$

$$\begin{aligned}&\sin\left(A\cos\left(\omega t\right)+\delta^0\right)\\ &=\sin\left(A\cos\left(\omega t\right)\right)\cos\left(\delta^0\right)+\cos\left(A\cos\left(\omega t\right)\right)\sin\left(\delta^0\right)\end{aligned} \tag{A.4b}$$

These identities allow me to be able to reduce down the simplest of the terms in the equation for I_{dc}.

$$\begin{aligned}&\int_{-\pi}^{\pi}\cos\left(A\cos\left(\omega t\right)+\delta^0\right)dt\\ &=\int_{-\pi}^{\pi}\cos\left(A\cos\left(\omega t\right)\right)\cos\left(\delta^0\right)dt-\int_{-\pi}^{\pi}\sin\left(A\cos\left(\omega t\right)\right)\sin\left(\delta^0\right)dt\\ &=\cos\left(\delta^0\right)\cancelto{2\pi J_0(A)}{\int_{-\pi}^{\pi}\cos\left(A\cos\left(\omega t\right)\right)dt}-\sin\left(\delta^0\right)\cancelto{0}{\int_{-\pi}^{\pi}\sin\left(A\cos\left(\omega t\right)\right)dt}\\ &=2\pi\cos\left(\delta^0\right)J_0(A)\end{aligned} \tag{A.5a}$$

$$\begin{aligned}&\int_{-\pi}^{\pi}\sin\left(A\cos\left(\omega t\right)+\delta^0\right)dt\\ &=\int_{-\pi}^{\pi}\sin\left(A\cos\left(\omega t\right)\right)\cos\left(\delta^0\right)dt+\int_{-\pi}^{\pi}\cos\left(A\cos\left(\omega t\right)\right)\sin\left(\delta^0\right)dt\\ &=\sin\left(\delta^0\right)\cancelto{2\pi J_0(A)}{\int_{-\pi}^{\pi}\cos\left(A\cos\left(\omega t\right)\right)dt}-\cos\left(\delta^0\right)\cancelto{0}{\int_{-\pi}^{\pi}\sin\left(A\cos\left(\omega t\right)\right)dt}\\ &=2\pi\sin\left(\delta^0\right)J_0(A)\end{aligned} \tag{A.5b}$$

More complicated integrals involve two multiplied nested sinusoidals. To solve these, I make the assumption that for integers n and m, $2n\omega_1 \neq 2m\omega_2$ unless the value the integers is very high. For these purposes, it is important that the PEM frequencies are not multiples of each other. I can then make use of

$$\int_{-\pi}^{\pi} \cos(2n\omega_1 t)\cos(2m\omega_2 t)dt = \begin{cases} \pi, & \text{if } 2n\omega_1 = 2m\omega_2 \\ 0, & \text{if } 2n\omega_1 \neq 2m\omega_2 \end{cases} \tag{A.6a}$$

$$\int_{-\pi}^{\pi} \sin(2n\omega_1 t)\sin(2m\omega_2 t)dt = \begin{cases} \pi, & \text{if } 2n\omega_1 = 2m\omega_2 \\ 0, & \text{if } 2n\omega_1 \neq 2m\omega_2 \end{cases} \tag{A.6b}$$

$$\int_{-\pi}^{\pi} \cos(2n\omega_1 t)\sin(2m\omega_2 t)dt = \int_{-\pi}^{\pi} \sin(2n\omega_1 t)\cos(2m\omega_2 t)dt = 0 \tag{A.6c}$$

I can make the assumption that only the latter cases in the above conditional equations will occur, because as can be seen below, the coefficients of the non-zero terms with high n and m will be negligible (as i increases, $J_i(x)$ gets sufficiently small, across generally all x, and especially in the region expected for our PEM amplitudes). And therefore the more complex expressions can be solved as

$$\begin{aligned}
&\int_{-\pi}^{\pi} \cos(A_1\cos(\omega_1 t))\cos(A_2\cos(\omega_2 t))dt \\
&= \int_{-\pi}^{\pi} \left(\left[J_0(A_1) + 2\sum_{n=1}^{\infty} (-1)^n J_{2n}(A_1)\cos(2n\omega_1 t) \right] \right. \\
&\quad \left. \times \left[J_0(A_2) + 2\sum_{n=1}^{\infty} (-1)^n J_{2n}(A_2)\cos(2n\omega_2 t) \right] \right) dt \\
&= \int_{-\pi}^{\pi} J_0(A_1)J_0(A_2)dt + 2\sum_{n=1}^{\infty} \left[(-1)^n J_0(A_1)J_{2n}(A_2) \cancelto{0}{\int_{-\pi}^{\pi} \cos(2n\omega_2 t)dt} \right] \\
&\quad + 2\sum_{n=1}^{\infty} \left[(-1)^n J_0(A_2)J_{2n}(A_1) \cancelto{0}{\int_{-\pi}^{\pi} \cos(2n\omega_1 t)dt} \right] \\
&\quad + 4\sum_{n=1}^{\infty}\sum_{m=1}^{\infty} \left[(-1)^{n+m} J_{2n}(A_1)J_{2m}(A_2) \cancelto{\sim 0}{\int_{-\pi}^{\pi} \cos(2n\omega_1 t)\cos(2m\omega_2 t)dt} \right]
\end{aligned}$$

$$=2\pi J_0(A_1)J_0(A_2) \tag{A.7}$$

$$\begin{aligned}
&\int_{-\pi}^{\pi} \cos\left(A_1\cos\left(\omega_1 t\right)\right)\sin\left(A_2\cos\left(\omega_2 t\right)\right)dt \\
&= \int_{-\pi}^{\pi} \left(\left[J_0(A_1) + 2\sum_{n=1}^{\infty}(-1)^n J_{2n}(A_1)\cos\left(2n\omega_1 t\right) \right] \right. \\
&\quad \left. \times \left[2\sum_{n=0}^{\infty}(-1)^n J_{2n+1}(A_2)\cos\left((2n+1)\omega_2 t\right) \right] \right) dt \\
&= 2\sum_{n=0}^{\infty} \left[(-1)^{2n+1} J_0(A_1) J_{2n+1}(A_2) \cancelto{0}{\int_{-\pi}^{\pi} \cos\left((2n+1)\omega_2 t\right)dt} \right] \\
&\quad + 4\sum_{n=1}^{\infty}\sum_{m=0}^{\infty} \left[(-1)^{n+2m+1} J_{2n}(A_1) J_{2m+1}(A_2) \cancelto{0}{\int_{-\pi}^{\pi} \cos\left(2n\omega_1 t\right)\cos\left((2m+1)\omega_2 t\right)dt} \right]
\end{aligned}$$

$$=0 \tag{A.8}$$

$$\begin{aligned}
&\int_{-\pi}^{\pi} \sin\left(A_1\cos\left(\omega_1 t\right)\right)\cos\left(A_2\cos\left(\omega_2 t\right)\right)dt \\
&= \int_{-\pi}^{\pi} \left(\left[2\sum_{n=0}^{\infty}(-1)^n J_{2n+1}(A_1)\cos\left((2n+1)\omega_1 t\right) \right] \right. \\
&\quad \left. \times \left[J_0(A_2) + 2\sum_{n=1}^{\infty}(-1)^n J_{2n}(A_2)\cos\left(2n\omega_2 t\right) \right] \right) dt \\
&= 2\sum_{n=0}^{\infty} \left[(-1)^{2n+1} J_0(A_2) J_{2n+1}(A_1) \cancelto{0}{\int_{-\pi}^{\pi} \cos\left((2n+1)\omega_1 t\right)dt} \right] \\
&\quad + 4\sum_{n=1}^{\infty}\sum_{m=0}^{\infty} \left[(-1)^{n+2m+1} J_{2n}(A_2) J_{2m+1}(A_1) \cancelto{0}{\int_{-\pi}^{\pi} \cos\left(2n\omega_2 t\right)\cos\left((2m+1)\omega_1 t\right)dt} \right]
\end{aligned}$$

$$=0 \tag{A.9}$$

$$
\begin{aligned}
&\int_{-\pi}^{\pi} \sin\left(A_1 \cos\left(\omega_1 t\right)\right) \sin\left(A_2 \cos\left(\omega_2 t\right)\right) dt \\
=&\int_{-\pi}^{\pi} \left(\left[2 \sum_{n=0}^{\infty} (-1)^n J_{2n+1}(A_1) \cos\left((2n+1)\omega_1 t\right) \right] \right. \\
&\left. \times \left[2 \sum_{n=0}^{\infty} (-1)^{2n+1} J_{2n+1}(A_2) \cos\left((2n+1)\omega_2 t\right) \right] \right) dt \\
=&4 \sum_{n=0}^{\infty} \sum_{m=0}^{\infty} \left[(-1)^{2(n+m+1)} J_{2n+1}(A_1) J_{2m+1}(A_2) \right. \\
&\left. \times \int_{-\pi}^{\pi} \cos\left((2n+1)\omega_1 t\right) \cos\left((2m+1)\omega_2 t\right) dt \right] \sim 0 \\
=&0
\end{aligned}
\tag{A.10}
$$

There are a few new expression types found when working on the expression for I_{ω_1}. These involve the integration of the products of nested and normal sinusoidal functions. In order to deal with these new expressions, it is necessary to bear in mind what is known from Eq. A.6; that $\int_{-\pi}^{\pi} \cos\left(x\right) \cos\left(y\right) dt \neq 0$ only if x and y are the same.

$$
\begin{aligned}
&\int_{-\pi}^{\pi} \sin\left(a_i \cos\left(\omega_i t\right)\right) \cos\left(\omega_i t\right) dt \\
&\quad = \int_{-\pi}^{\pi} \left(2 \sum_{n=0}^{\infty} (-1)^n J_{2n+1}(a_i) \cos\left((2n+1)\omega_i t\right) \right) \cos\left(\omega_i t\right) dt \\
&\quad = 2(-1)^0 J_1(a_i) \int_{-\pi}^{\pi} \cos(\omega_i t) \cos(\omega_i t) dt \sim \pi \\
&\quad + 2 \sum_{n=1}^{\infty} \left[(-1)^n J_{2n+1}(a_i) \int_{-\pi}^{\pi} \cos\left((2n+1)\omega_i t\right) \cos\left(\omega_i t\right) dt \right] \sim 0 \\
&\quad = 2\pi J_1(a_i)
\end{aligned}
\tag{A.11}
$$

$$\begin{aligned}
&\int_{-\pi}^{\pi} \cos\left(a_i \cos\left(\omega_i t\right)\right) \cos\left(\omega_j t\right) dt \\
&\quad = \int_{-\pi}^{\pi} \left(J_0(a_i) + 2\sum_{n=1}^{\infty} (-1)^n J_{2n}(a_i) \cos\left(2n\omega_i t\right) \right) \cos\left(\omega_j t\right) dt \\
&\quad = J_0(a_i) \int_{-\pi}^{\pi} \cancelto{0}{\cos\left(\omega_j t\right) dt} + 2 \int_{-\pi}^{\pi} \left[\sum_{n=1}^{\infty} (-1)^n J_{2n}(a_i) \cos\left(2n\omega_i t\right) \cos\left(\omega_j t\right) \right] dt \\
&\quad = 2\sum_{n=1}^{\infty} \left[(-1)^n J_{2n}(a_i) \cancelto{0}{\int_{-\pi}^{\pi} \cos\left(2n\omega_i t\right) \cos\left(\omega_j t\right) dt} \right] \\
&\quad = 0
\end{aligned} \tag{A.12}$$

$$\begin{aligned}
&\int_{-\pi}^{\pi} \sin\left(a_i \cos\left(\omega_i t\right)\right) \cos\left(\omega_j t\right) dt \qquad ; \mathbf{i} \neq \mathbf{j} \\
&\quad = \int_{-\pi}^{\pi} \left(2\sum_{n=0}^{\infty} (-1)^n J_{2n+1}(a_i) \cos\left((2n+1)\omega_i t\right) \right) \cos\left(\omega_j t\right) dt \\
&\quad = 2\sum_{n=0}^{\infty} \left[(-1)^{2n+1} J_{2n+1}(a_i) \cancelto{0}{\int_{-\pi}^{\pi} \cos\left((2n+1)\omega_i t\right) \cos\left(\omega_j t\right) dt} \right] \\
&\quad = 0
\end{aligned} \tag{A.13}$$

Expressions will also be encountered where there are two nested sinusoidal expressions multiplied by one normal sinusoidal expression. It's worth first noting the following identities, where no more than two of x, y and z are equal, and each are integers, as discussed.

$$\int_{-\pi}^{\pi} \cos(xt)\cos(yt)\cos(zt)dt = 0 \tag{A.14a}$$

$$\int_{-\pi}^{\pi} \sin(xt)\cos(yt)\cos(zt)dt = 0 \tag{A.14b}$$

$$\int_{-\pi}^{\pi} \cos(xt)\sin(yt)\cos(zt)dt = 0 \tag{A.14c}$$

$$\int_{-\pi}^{\pi} \sin(xt)\sin(yt)\cos(zt)dt = 0 \tag{A.14d}$$

I then have a way to deal with the more complicated expressions.

$$
\begin{aligned}
&\int_{-\pi}^{\pi} \cos\left(a_i \cos\left(\omega_i t\right)\right) \cos\left(a_j \cos\left(\omega_j t\right)\right) \cos\left(\omega_i t\right) dt \\
&\quad = \int_{-\pi}^{\pi} \left(J_0(a_i) + 2\sum_{n=1}^{\infty} (-1)^n J_{2n}(a_i) \cos\left(2n\omega_i t\right) \right) \\
&\quad \times \left(J_0(a_j) + 2\sum_{n=1}^{\infty} (-1)^n J_{2n}(a_j) \cos\left(2n\omega_j t\right) \right) \cos\left(\omega_i t\right) dt \\
&\quad = J_0(a_i) J_0(a_j) \cancelto{0}{\int_{-\pi}^{\pi} \cos\left(\omega_i t\right) dt} \\
&\quad + 2J_0(a_i) \sum_{n=1}^{\infty} \left[(-1)^n J_{2n}(a_j) \cancelto{0}{\int_{-\pi}^{\pi} \cos\left(\omega_i t\right) \cos\left(2n\omega_j t\right) dt} \right] \\
&\quad + 2J_0(a_j) \sum_{n=1}^{\infty} \left[(-1)^n J_{2n}(a_i) \cancelto{0}{\int_{-\pi}^{\pi} \cos\left(\omega_i t\right) \cos\left(2n\omega_i t\right) dt} \right] \\
&\quad + 4\sum_{n=1}^{\infty} \sum_{m=1}^{\infty} \left[(-1)^{n+m} J_{2n}(a_i) J_{2m}(a_j) \cancelto{0}{\int_{-\pi}^{\pi} \cos(2n\omega_i t) \cos(2m\omega_j t) \cos\left(\omega_i t\right) dt} \right] \\
&\quad = 0
\end{aligned}
\tag{A.15}
$$

$$
\begin{aligned}
&\int_{-\pi}^{\pi} \sin\left(a_i \cos\left(\omega_i t\right)\right) \cos\left(a_j \cos\left(\omega_j t\right)\right) \cos\left(\omega_i t\right) dt \\
&\quad = \int_{-\pi}^{\pi} \left(2\sum_{n=0}^{\infty} (-1)^n J_{2n+1}(a_i) \cos\left((2n+1)\omega_i t\right) \right) \\
&\quad \times \left(J_0(a_j) + 2\sum_{n=1}^{\infty} (-1)^n J_{2n}(a_j) \cos\left(2n\omega_j t\right) \right) \cos\left(\omega_i t\right) dt
\end{aligned}
$$

$$
\begin{aligned}
&= 2J_0(a_j)(-1)^0 J_1(a_i) \int_{-\pi}^{\pi} \cos(1\omega_i t)\cos(\omega_i t)dt \\
&+ 2J_0(a_j)\sum_{n=1}^{\infty}\left[(-1)^n J_{2n+1}(a_i)\int_{-\pi}^{\pi}\cos\left((2n+1)\omega_i t\right)\cos(\omega_i t)dt\right] \\
&+ 4\sum_{n=0}^{\infty}\sum_{m=1}^{\infty}\Bigg[(-1)^{(n+m} J_{2n+1}(a_i)J_{2m}(a_j) \\
&\times \int_{-\pi}^{\pi}\cos\left((2n+1)\omega_i t\right)\cos(2m\omega_j t)\cos\left(\omega_i t\right)dt\Bigg] \\
&= 2\pi J_1(a_i)J_0(a_j)
\end{aligned}
\tag{A.16}
$$

$$
\begin{aligned}
&\int_{-\pi}^{\pi}\cos\left(a_i\cos\left(\omega_i t\right)\right)\sin\left(a_j\cos\left(\omega_j t\right)\right)\cos\left(\omega_i t\right)dt \\
&= \int_{-\pi}^{\pi}\left(J_0(a_i) + 2\sum_{n=1}^{\infty}(-1)^n J_{2n}(a_i)\cos\left(2n\omega_i t\right)\right) \\
&\times \left(2\sum_{n=0}^{\infty}(-1)^n J_{2n+1}(a_j)\cos\left((2n+1)\omega_j t\right)\right)\cos\left(\omega_i t\right)dt \\
&= 2J_0(a_i)\sum_{n=1}^{\infty}\left[(-1)^n J_{2n+1}(a_j)\int_{-\pi}^{\pi}\cos\left((2n+1)\omega_j t\right)\cos\left(\omega_i t\right)dt\right] \\
&\quad + 4\sum_{n=1}^{\infty}\sum_{m=0}^{\infty}\Bigg[(-1)^{(n+m} J_{2n}(a_i)J_{2m+1}(a_j) \\
&\int_{-\pi}^{\pi}\cos\left(2n\omega_i t\right)\cos\left((2m+1)\omega_j t\right)\cos\left(\omega_i t\right)dt\Bigg] \\
&= 0
\end{aligned}
\tag{A.17}
$$

$$\int_{-\pi}^{\pi} \sin\left(a_i \cos\left(\omega_i t\right)\right) \sin\left(a_j \cos\left(\omega_j t\right)\right) \cos\left(\omega_i t\right) dt$$

$$= \int_{-\pi}^{\pi} \left(2 \sum_{n=0}^{\infty} (-1)^n J_{2n+1}(a_i) \cos\left((2n+1)\omega_i t\right) \right)$$

$$\times \left(2 \sum_{n=0}^{\infty} (-1)^n J_{2n+1}(a_j) \cos\left((2n+1)\omega_j t\right) \right) \cos\left(\omega_i t\right) dt$$

$$= 4 \sum_{n=0}^{\infty} \sum_{m=0}^{\infty} \Bigg[(-1)^{(n+m} J_{2n+1}(a_i) J_{2m+1}(a_j)$$

$$\times \int_{-\pi}^{\pi} \cos\left((2n+1)\omega_i t\right) \cos\left((2m+1)\omega_j t\right) \cos\left(\omega_i t\right) dt \Bigg] \quad \rightarrow 0$$

$$= 0 \tag{A.18}$$

For the treatment of $I_{2\omega_1}$ and $I_{2\omega_2}$, the expressions I need to simplify are not far removed from what was encountered above. Eqs. A.14 are still relevant. First of all, I'll look at how to deal with expressions integrating $\cos\left((A\cos(\omega_i t)\right)\cos(2\omega_j t)$ and $\sin\left((A\cos(\omega_i t)\right)\cos(2\omega_j t)$.

$$\int_{-\pi}^{\pi} \cos\left(a_i \cos\left(\omega_i t\right)\right) \cos\left(2\omega_i t\right) dt$$

$$= \int_{-\pi}^{\pi} \left(J_0(a_i) + 2 \sum_{n=1}^{\infty} (-1)^n J_{2n}(a_i) \cos\left(2n\omega_i t\right) \right) \cos\left(2\omega_i t\right) dt$$

$$= J_0(a_i) \int_{-\pi}^{\pi} \cos\left(\omega_i t\right) dt \rightarrow 0 + 2(-1)^1 J_2(a_i) \int_{-\pi}^{\pi} \cos(2\omega_i t) \cos(2\omega_i t) dt \rightarrow \pi$$

$$+ 2 \sum_{n=2}^{\infty} \left[(-1)^n J_{2n}(a_i) \int_{-\pi}^{\pi} \cos\left(2n\omega_i t\right) \cos\left(2\omega_i t\right) dt \right] \rightarrow 0$$

$$= -2\pi J_2(a_i) \tag{A.19}$$

$$\int_{-\pi}^{\pi} \cos\left(a_i \cos\left(\omega_i t\right)\right) \cos\left(2\omega_j t\right) dt \qquad ; \mathbf{i} \neq \mathbf{j}$$

$$= \int_{-\pi}^{\pi} \left(J_0(a_i) + 2\sum_{n=1}^{\infty} (-1)^n J_{2n}(a_i) \cos\left(2n\omega_i t\right) \right) \cos\left(2\omega_j t\right) dt$$

$$= J_0(a) \int_{-\pi}^{\pi} \cos\left(2\omega_j t\right) dt \to 0$$

$$+ 2\int_{-\pi}^{\pi} \left[\sum_{n=1}^{\infty} (-1)^n J_{2n}(a_i) \cos\left(2n\omega_i t\right) \cos\left(2\omega_j t\right) \right] dt$$

$$= 2\sum_{n=1}^{\infty} \left[(-1)^n J_{2n}(a_i) \int_{-\pi}^{\pi} \cos\left(2n\omega_i t\right) \cos\left(2\omega_j t\right) dt \right] \to 0$$

$$= 0 \tag{A.20}$$

$$\int_{-\pi}^{\pi} \sin\left(a_i \cos\left(\omega_i t\right)\right) \cos\left(2\omega_j t\right) dt \tag{A.21}$$

$$= \int_{-\pi}^{\pi} \left(2\sum_{n=0}^{\infty} (-1)^n J_{2n+1}(a_i) \cos\left((2n+1)\omega_i t\right) \right) \cos\left(2\omega_j t\right) dt$$

$$= 2\sum_{n=0}^{\infty} \left[(-1)^{2n+1} J_{2n+1}(a_i) \int_{-\pi}^{\pi} \cos\left((2n+1)\omega_i t\right) \cos\left(2\omega_j t\right) dt \right] \to 0$$

$$= 0 \tag{A.22}$$

And now the more complicated versions with three sinusoidals,

$$\int_{-\pi}^{\pi} \cos\left(a_i \cos\left(\omega_i t\right)\right) \cos\left(a_j \cos\left(\omega_j t\right)\right) \cos\left(2\omega_i t\right) dt$$

$$= \int_{-\pi}^{\pi} \left(J_0(a_i) + 2\sum_{n=1}^{\infty} (-1)^n J_{2n}(a_i) \cos\left(2n\omega_i t\right) \right)$$

$$\left(J_0(a_j) + 2\sum_{n=1}^{\infty} (-1)^n J_{2n}(a_j) \cos\left(2n\omega_j t\right) \right) \cos\left(2\omega_i t\right) dt$$

$$
\begin{aligned}
&= J_0(a_i)J_0(a_j)\cancelto{0}{\int_{-\pi}^{\pi}\cos(2\omega_i t)dt} \\
&+ 2J_0(a_i)\sum_{n=1}^{\infty}\left[(-1)^n J_{2n}(a_j)\cancelto{0}{\int_{-\pi}^{\pi}\cos(2\omega_i t)\cos(2n\omega_j t)dt}\right] \\
&+ 2J_0(a_j)\left[(-1)^1 J_2(a_i)\cancelto{\pi}{\int_{-\pi}^{\pi}\cos(2\omega_i t)\cos(2\omega_i t)dt}\right] \\
&+ 2J_0(a_j)\sum_{n=2}^{\infty}\left[(-1)^n J_{2n}(a_i)\cancelto{0}{\int_{-\pi}^{\pi}\cos(2\omega_i t)\cos(2n\omega_i t)dt}\right] \\
&+ 4\sum_{n=1}^{\infty}\sum_{m=1}^{\infty}\left[(-1)^{n+m}J_{2n}(a_i)J_{2m}(a_j)\cancelto{0}{\int_{-\pi}^{\pi}\cos(2n\omega_i t)\cos(2m\omega_j t)\cos(\omega_i t)dt}\right] \\
&= -2\pi J_2(a_i)J_0(a_j) \qquad \text{(A.23)}
\end{aligned}
$$

$$
\begin{aligned}
&\int_{-\pi}^{\pi}\sin(a_i\cos(\omega_i t))\cos(a_j\cos(\omega_j t))\cos(2\omega_i t)dt \\
&= \int_{-\pi}^{\pi}\left(2\sum_{n=0}^{\infty}(-1)^n J_{2n+1}(a_i)\cos((2n+1)\omega_i t)\right) \\
&\times\left(J_0(a_j)+2\sum_{n=1}^{\infty}(-1)^n J_{2n}(a_j)\cos(2n\omega_j t)\right)\cos(2\omega_i t)dt \\
&= 2J_0(a_j)\sum_{n=0}^{\infty}\left[(-1)^n J_{2n+1}(a_i)\cancelto{0}{\int_{-\pi}^{\pi}\cos((2n+1)\omega_i t)\cos(2\omega_i t)dt}\right] \\
&+ 4\sum_{n=0}^{\infty}\sum_{m=1}^{\infty}\Bigg[(-1)^{(n+m}J_{2n+1}(a_i)J_{2m}(a_j) \\
&\times\cancelto{0}{\int_{-\pi}^{\pi}\cos((2n+1)\omega_i t)\cos(2m\omega_j t)\cos(2\omega_i t)dt}\Bigg] \\
&= 0 \qquad \text{(A.24)}
\end{aligned}
$$

$$
\begin{aligned}
&\int_{-\pi}^{\pi} \cos\left(a_i \cos\left(\omega_i t\right)\right) \sin\left(a_j \cos\left(\omega_j t\right)\right) \cos\left(2\omega_i t\right) dt \\
&\quad = \int_{-\pi}^{\pi} \left(J_0(a_i) + 2\sum_{n=1}^{\infty} (-1)^n J_{2n}(a_i) \cos\left(2n\omega_i t\right) \right) \\
&\quad \times \left(2\sum_{n=0}^{\infty} (-1)^n J_{2n+1}(a_j) \cos\left((2n+1)\omega_j t\right) \right) \cos\left(2\omega_i t\right) dt \\
&\quad = 2J_0(a_i) \sum_{n=1}^{\infty} \left[(-1)^n J_{2n+1}(a_j) \int_{-\pi}^{\pi} \cos\left((2n+1)\omega_j t\right) \cos\left(2\omega_i t\right) dt \right] \quad \rightarrow 0 \\
&\quad + 4\sum_{n=1}^{\infty}\sum_{m=0}^{\infty} \left[(-1)^{(n+m} J_{2n}(a_i) J_{2m+1}(a_j) \right. \\
&\quad \left. \times \int_{-\pi}^{\pi} \cos\left(2n\omega_i t\right) \cos\left((2m+1)\omega_j t\right) \cos\left(2\omega_i t\right) dt \right] \quad \rightarrow 0 \\
&\quad = 0
\end{aligned}
\tag{A.25}
$$

$$
\begin{aligned}
&\int_{-\pi}^{\pi} \sin\left(a_i \cos\left(\omega_i t\right)\right) \sin\left(a_j \cos\left(\omega_j t\right)\right) \cos\left(2\omega_i t\right) dt \\
&\quad = \int_{-\pi}^{\pi} \left(2\sum_{n=0}^{\infty} (-1)^n J_{2n+1}(a_i) \cos\left((2n+1)\omega_i t\right) \right) \\
&\quad \times \left(2\sum_{n=0}^{\infty} (-1)^n J_{2n+1}(a_j) \cos\left((2n+1)\omega_j t\right) \right) \cos\left(2\omega_i t\right) dt \\
&\quad = 4\sum_{n=0}^{\infty}\sum_{m=0}^{\infty} \left[(-1)^{(n+m} J_{2n+1}(a_i) J_{2m+1}(a_j) \right. \\
&\quad \left. \times \int_{-\pi}^{\pi} \cos\left((2n+1)\omega_i t\right) \cos\left((2m+1)\omega_j t\right) \cos\left(2\omega_i t\right) dt \right] \quad \rightarrow 0 \\
&\quad = 0
\end{aligned}
\tag{A.26}
$$

References

[1] Jasse, B.; Koenig, J. *J. Macromol. Sci. Part C* **1979,** *17,* 61–135.

[2] Steininger, J.; Strauss, A.; Brebrick, R. *J. Electrochem. Soc.* **1970,** *117,* 1305–1309.

[3] Szeles, C. *Phys. Stat. Sol. (b)* **2004,** *241*, 783–790.

[4] Kaminow, I.; Turner, E. *Appl. Opt.* **1966,** *5,* 1612–1628.

[5] Tompkins, H. G. *A User's Guide to Ellipsometry;* Dover Publications: New York, 2006.

[6] Goldstein, D. H. *Polarized Light;* CRC Press: Boca Raton, FL, 2010.

[7] Hecht, E.; Zajac, A. *Optics;* Addision-Wesley: Reading, MA, 1979.

[8] Tyo, J. S.; Goldstein, D. L.; Chenault, D. B.; Shaw, J. A. *Appl. Opt.* **2006,** *45,* 5453–5469.

[9] Lin, H. *ASP Conf. Ser.* **2005,** *343,* 357–368.

[10] Hore, D. K.; Natansohn, A.; Rochon, P. *J. Phys. Chem. B* **2002,** *106,* 9004–9012.

[11] Hall, S. A.; Covert, P. A.; Blinn, B. R.; Shakeri, S.; Hore, D. K. *J. Phys. Chem. C* **2013,** *117,* 1796–1803.

[12] Chenault, D. B.; Chipman, R. A.; Lu, S. Y. *Appl. Opt.* **1994,** *33,* 7382–7389.

[13] Chenault, D. B.; Chipman, R. A. *Appl. Opt.* **1993,** *32,* 3513–3519.

[14] Hore, D. K.; Natansohn, A. L.; Rochon, P. L. *J. Phys. Chem. B* **2003,** *107,* 2197–2204.

[15] Hore, D. K.; Natansohn, A. L.; Rochon, P. L. *J. Phys. Chem. B.* **2003,** *107,* 2506–2518.

[16] Hore, D. K.; Natansohn, A.; Rochon, P. *Physics in Canada* **2003,** *59,* 139–144.

[17] Hore, D.; Wu, Y.; Natansohn, A.; Rochon, P. *J. Appl. Phys.* **2003,** *94,* 2162–2166.

[18] Robbie, K.; Broer, D. J.; Brett, M. J. *Nature* **1999,** *399,* 764–766.

[19] Robbie, K.; Brett, M. J.; Lakhtakia, A. *Nature* **1996,** *384,* 616.

[20] Schubert, M.; Dollase, W. *Opt. Lett.* **2002,** *27,* 2073–2075.

[21] Röseler, A. *Infrared spectroscopic ellipsometry;* Wiley-VCH Verlag GmbH: 1990.

[22] Guan, W.; Jones, G. A.; Liu, Y. W.; Shen, T. H. *J. Appl. Phys.* **2008,** *103,* 043104.

[23] Mackey, J. R.; Salari, E.; Tin, P. *Opt. Eng.* **2003,** *42,* 1460–1466.

[24] Liu, Y. W.; Jones, G. A.; Peng, Y.; Shen, T. H. *J. Appl. Phys.* **2006,** *100,* 063537.

[25] Kuldkepp, M.; Hawkes, N. C.; Rachlew, E.; Schunke, B. *Appl. Opt.* **2005,** *44,* 5899-5904.

[26] Cross, L. J. K.; Hore, D. K. *Appl. Opt.* **2012,** *51,* 5100–5110.

[27] Hall, S. A.; Hoyle, M.-A.; Post, J. S.; Hore, D. K. *Anal. Chem.* **2013,** *85,* 7613–7619.

[28] Berry, H. G.; Gabrielse, G.; Livingston, A. E. *Appl. Opt.* **1977,** *16,* 3200–3205.

[29] Boyer, G. R.; Lamouroux, B. F.; Prade, B. S. *Appl. Opt.* **1979,** *18,* 1217–1219.

[30] Guan, W.; Cook, P. J.; Jones, G. A.; Shen, T. H. *Appl. Opt.* **2010,** *49,* 2644–2652.

[31] Schäfers, F.; Mertins, H.-C.; Gaupp, A.; Gudat, W.; Mertin, M.; Packe, I.; Schmolla, F.; Fonzo, S. D.; Soullié, G.; Jark, W.; Walker, R.; Cann, X. L.; Nyholm, R.; Eriksson, M. *Appl. Opt.* **1999,** *38,* 4074–4088.

[32] Koide, T.; Shidara, T.; Yuri, M.; Kandaka, N.; Fukutani, H.; Yamaguchi, K. *Rev. Sci. Instrum.* **1992,** *63,* 1458–1461.

[33] Voss, K. J.; Liu, Y. *Appl. Opt.* **1997,** *36,* 6083–6094.

[34] Hofmann, T.; Schubert, M.; Leibiger, G.; Gottschalch, V. *Appl. Phys. Lett.* **2007,** *90,* 182110.

[35] Goldstein, D. H.; Chipman, R. A.; Chenault, D. B. *Opt. Eng.* **1989,** *28,* 120–125.

[36] Bremer, J.; Hunderi, O.; Fanping, K.; Skauli, T.; Wold, E. *Appl. Opt* **1992,** *31,* 471–478.

[37] Zhang, K. Q.; Yen, Y.-h. *Appl. Opt* **1989,** *28,* 2929–2934.

[38] Tiwald, T. E.; Thompson, D. W.; Woollam, J. A.; Pepper, S. V. *Thin Solid Films* **1998,** *313,* 718–721.

[39] Drevillon, B. *Thin Solid Films* **1998,** *313,* 625–630.

[40] Xia, G.-Q.; Zhang, R.-J.; Chen, Y.-L.; Zhao, H.-B.; Wand, S.-Y.; Zhou, S.-M.; Zheng, Y.-X.; Yang, Y.-M.; Chen, L.-Y. *Rev. Sci. Instrum.* **2000,** *71,* 2677–2683.

[41] Garcia-Caurel, E.; Bertran, E.; Canillas, A. *Thin Solid Films* **1999,** *354,* 187–194.

[42] Kudenov, M. W.; Hagen, N. A.; Dereniak, E. L.; Gerhart, G. R. *Opt. Express* **2007,** *15,* 12792–12805.

[43] Hofmann, T.; Gottschalch, V.; Schubert, M. *Appl. Phys. Lett* **2007,** *91,* 121908.

[44] Hofmann, T.; Gottschalch, V.; Schubert, M. *Phys. Rev. B* **2002,** *66,* 195204.

[45] Hofmann, T.; Schubert, M.; Herzinger, C. M.; Pietzonka, I. *Appl. Phys. Lett.* **2003,** *82,* 3463–3465.

[46] Hofmann, T.; Schade, U.; Agarwal, K. C.; Daniel, B.; Klingshirn, C.; Hetterich, M.; Herzinger, C. M.; Schubert, M. *Appl. Phys. Lett.* **2006,** *88,* 042105.

[47] Kircher, J.; Henn, R.; Cardona, M.; Richards, P. L.; Williams, G. P. *J. Opt. Soc. Am. B* **1997,** *14,* 705–712.

[48] Giudicotti, L.; Brombin, M. *Appl. Opt.* **2007,** *46,* 2638–2648.

[49] Hofmann, T.; Schade, U.; Herzinger, C. M.; Esquinazi, P.; Schubert, M. *Rev. Sci. Instrum.* **2006,** *77,* 063902.

[50] Hofmann, T.; Herzinger, C. M.; Tedesco, J. L.; Gaskill, D. K.; Woollam, J. A.; Schubert, M. *Thin Solid Films* **2011,** *519,* 2593–2600.

[51] Hofmann, T.; Boosalis, A.; Kühne, P.; Herzinger, C. M.; Woolam, J. A.; Gaskill, D. K.; Tedesco, J. L.; Schubert, M. *Appl. Phys. Lett.* **2011,** *98,* 041906.

[52] Schöche, S.; Shi, J.; Boosalis, A.; Kühne, P.; Herzinger, C. M.; Woollam, J. A.; Schaff, W. J.; Eastman, L. F.; Schubert, M.; Hofmann, T. *Appl. Phys. Lett.* **2011,** *98,* 092103.

[53] Akabane, K. *Proc. IRE* **1958,** *46,* 194–197.

[54] Sparks, W.; Germer, T. A.; MacKenty, J. W.; Snik, F. *Appl. Opt.* **2012,** *51,* 5495–5511.

[55] Todorov, T.; Nikolova, L.; Stoilov, G.; Hristov, B. *Appl. Opt.* **2007,** *46,* 6662–6668.

[56] Todorov, T.; Nikolova, L. *Opt. Lett.* **1992,** *17,* 358–359.

[57] Nikolova, L.; Ivanov, M.; Todorov, T.; Stoyanov, S. *Bulg. J. Phys.* **1993,** *20,* 46–54.

[58] Kiefer, J.; Yariv, A. *Appl. Phys. Lett.* **1969,** *15*, 26–27.

[59] Sordo, S. D.; Abbene, L.; Caroli, E.; Mancini, A. M.; Zappettini, A.; Ubertini, P. *Sensors* **2009,** *9*, 3491–3526.

[60] Becker, K.; Johnson, B.; Edwards, G. *Rev. Sci. Instrum.* **1994,** *65*, 1496–1501.

[61] Wang, J.; Buck, S. M.; Even, M. A.; Chen, Z. *J. Am. Chem. Soc.* **2002,** *124*, 13302–13305.

[62] Kim, J.; Somorjai, G. A. *J. Am. Chem. Soc.* **2003,** *125*, 3150–3158.

[63] Kim, J.; Koffas, T. S.; Lawrence, C. C.; Somorjai, G. A. *Langmuir* **2004,** *20*, 4640–4646.

[64] Koffas, T. S.; Kim, J.; Lawrence, C. C.; Somorjai, G. A. *Langmuir* **2003,** *19*, 3563–3566.

[65] Chen, Z.; Ward, R.; Tian, Y.; Malizia, F.; Gracias, D. H.; Shen, Y. R.; Somorjai, G. A. *J. Biomed. Mater. Res.* **2002,** *62*, 254–264.

[66] Malyk, S.; Shalhout, F. Y.; O'Leary, L. E.; Lewis, N. S.; Benderskii, A. V. *J. Phys. Chem. C* **2013,** *117*, 935–944.

[67] Asanuma, H.; Noguchi, H.; Uosaki, K.; Yu, H.-Z. *J. Phys. Chem. B* **2006,** *110*, 4892–4899.

[68] Asanuma, H.; Noguchi, H.; Uosaki, K.; Yu, H.-Z. *J. Am. Chem. Soc.* **2008,** *130*, 8016–8022.

[69] Avrutsky, I.; Soref, R. *Opt. Express* **2011,** *19*, 21707–21716.

[70] Daum, W.; Krause, H.-J.; Reichel, U.; Ibach, H. *Phys. Rev. Lett.* **1993,** *71*, 1234–1237.

[71] Kolasinski, K. W.; DeWitt, K. M.; Harrison, I. *Phys. Stat. Sol.* **2007,** *204,* 1356–1361.

[72] Curtis, A. D.; Reynolds, S. B.; Calchera, A. R.; Patterson, J. E. *J. Phys. Chem. Lett.* **2010,** *1,* 2435–2439.

[73] Zheng, D.-S.; Wang, Y.; Liu, A.-A.; Wang, H.-F. *Int. Rev. Phys. Chem.* **2008,** *27,* 629–664.

[74] Lambert, A. G.; Davies, P. B.; Neivandt, D. J. *Appl. Spectrosc. Rev.* **2005,** *40,* 103–145.

[75] Hall, S. A.; Hickey, A. D.; Hore, D. K. *J. Phys. Chem. C* **2010,** *114,* 9748–9757.

[76] Lu, R.; Gan, W.; Wu, B.-H.; Zhang, Z.; Guo, Y.; Wang, H.-F. *J. Phys. Chem. B* **2005,** *109,* 14118–14129.

[77] Chen, Z.; Ward, R.; Tian, Y.; Baldelli, S.; Opdahl, A.; Shen, Y.-R.; Somorjai, G. A. *J. Am. Chem. Soc.* **2000,** *122,* 10615–10620.

[78] Wang, J.; Chen, C.; Buck, S. M.; Chen, Z. *J. Phys. Chem. B* **2001,** *105,* 12118–12125.

[79] Jena, K. C.; Covert, P. A.; Hall, S. A.; Hore, D. K. *J. Phys. Chem. C* **2011,** *115,* 15570–15574.

[80] Briggman, K. A.; Stephenson, J. C.; Wallace, W. E.; Richter, L. J. *J. Phys. Chem. B* **2001,** *105,* 2785–2791.

[81] Pouthier, V.; Ramseyer, C.; Girardet, C. *J. Chem. Phys.* **1998,** *108,* 6502–6512.

[82] Liljelad, J. F. D.; Tyrode, E. *J. Phys. Chem. C* **2012,** *116,* 22893–22903.

[83] Löbau, J.; Wolfrum, K. *J. Opt. Soc. Am. B* **1997,** *14,* 2505–2512.

[84] Jena, K.; Hung, K.-K.; Schwantje, T.; Hore, D. K. *J. Chem. Phys.* **2011,** *135,* 044704.

[85] Jellison, G. E.; Modine, F. A. *Appl. Opt.* **1997,** *36,* 8184–8189.

[86] Jellison, G. E.; Modine, F. A. *Appl. Opt.* **1997,** *36,* 8190-8198.

[87] Radhakrishnan, T. *Proc. Indian Acad. Sci.* **1951,** *31,* 22–34.

[88] Radhakrishnan, T. *Proc. Indian Acad. Sci.* **1947,** *22,* 260–265.

[89] Jena, K. C.; Covert, P. A.; Hore, D. K. *J. Chem. Phys.* **2011,** *134,* 044712.

[90] Bell, R. *Rev. Phys. Appl.* **1977,** *12,* 391–399.

[91] Rhoderick, E. *IEEE Proc.* **1982,** *129,* 1–14.